Adaptive control system of a slotless DC linear motor

By

Monier Habil

The thesis submitted in fulfilment of the requirement for the degree of Doctor of Philosophy

Wolfson Centre for Magnetics

School of Engineering

Cardiff University

Wales

June 2023

ABSTRACT

Slotless DC linear motors (SDCLM) offer several benefits over traditional linear motors, including higher efficiency, smoother operation, and higher power density. These advantages make them a popular choice for a wide range of applications in various industries. One of the main benefits of a slotless DC linear motor is the absence of slot harmonics, which can cause vibration and noise in traditional slotted motors. This makes slotless motors ideal for applications that require precise and smooth motion, such as in medical equipment, robotics, and semiconductor manufacturing. However, one of the challenges of a Slotless DC linear motor is the presence of force ripple, which can limit the motor's performance, precision, and accuracy. Force ripple is caused by the mutual attraction of the translator's magnets and iron cores. It is independent of the motor current and is determined only by the relative position of the motor coils regarding the magnets. To overcome these challenges, motor redesign, magnetic field optimisation and the use of an adaptive control system.

This research program focused on and investigated the above possible methods (i.e., motor redesign, magnetic field optimisation field and use of advanced control algorithms such as Sliding Mode Control SMC) to tackle the current challenges and improve the relevant industrial application performance and precision. The inquiry encompasses the analysis, design, and control of the SDCLM by proper modelling, building, and experimental validation of the modelled findings, applying both static and dynamic methodologies. Electrical, mechanical, and magnetic analyses were performed on the SDCLM design.

The performance of the SDCLM was investigated using a finite element method (FEM), and the motor parameters were improved. Investigation and analysis are performed about additional difficulties such as force ripple and normal force, where the results indicated that the flux density in the airgap and the thrust force were different between the actual time and the simulation by 7.14% and 8.07%, respectively. Moreover, sliding mode control is designed to achieve desired system performance, such as reducing the power ripple of a slotless DC linear motor. where the proposed control shows experiments that it has stability despite disturbances and uncertainties.

To improve the control method and reduce the steady-state error caused by the force ripple, the Bees algorithm has been used to tune the parameters of the controller.

Finally, the outcomes indicate that the control method employing the disturbance observer and Bees algorithm has enhanced the performance of both position and speed, while concurrently reducing the force ripple. A comparison between simulation and experiment shows that there is a difference in the tracking performance, where the difference was around 13.6%. This error could have arisen from the omission of certain errors that cannot be accounted for within the simulation. These errors may stem from issues with the position sensor or discrepancies in the manual system design process.

ACKNOWLEDGEMENTS

First and foremost, I appreciate ALLAH for assisting me in accomplishing my thesis.

I want to extend my sincere thanks to Dr. Fatih Anayi, my academic supervisor, for his superb direction, encouragement, compassion, and patience during this research as well as for creating a wonderful environment for me.

I want to express my deep gratitude to my loving family. my mother's prayer for me has kept me going so far. Words cannot express my gratitude to my father for his significant influence on my life and for the various sacrifices he made for my brothers and myself.

Lastly, I would like to express my gratitude to my wife in particular for her support, understanding, and encouragement throughout the years.

To my family

Contents

List of Figures

LIST OF ABBREVIATIONS AND NOMENCLATURES

Abbreviations

AC	Alternating current
BA	Bees algorithm
BLDCLM	Brushless direct current linear motor
BLPMSM	Brushless permanent magnet synchronous motor
DC	Direct current
DCLM	DC linear motor
DOB	Disturbance observer
EMCN	Equivalent magnetic circuit network
EMF	Electrical magnetic field
EMF	Electromotive force
FEM	Finite element method
ILC	Iterative learning control
IM	Induction motor
LIM	linear induction motor
LPMBDCM	Linear permanent magnet brushless DC motor
LSM	Linear synchronous motor
MMF	Magnetomotive force
NdFeB	Neodymium iron boron
PM	Permanent magnet
PMDCLM	Permanent magnet direct current linear motor
PWM	Pulse width modulation
SMC	Sliding mode control.
SDCLM	Slotless direct current linear motor
SmCo	Samarium cobalt
TLBO	Teaching learning-based optimization.
PID	Proportional integral derivative

Nomenclatures

H	Magnetic field strength
Φ_m	Magnetic flux
B_m	Magnetic flux density
B_s	Magnetic saturation flux density
B_i	Intrinsic magnetization
ψ	Flux linkage
Φ_l	Leakage flux
H_c	coercivity
B_r	Remanent magnetic flux density
H_g	Air-gap magnetic field intensity
H_m	Permanent magnet field intensity
B_g	Air-gap magnetic field density
q	Leakage coefficient
P_m	Permeance of the magnet
F	Electromagnetic force
N	Number of turns.
E_{emf}	Electromotive force
μ_R	relative permeability
μ	permeability
Φ	Flux
Ʀ	Reluctance
f_m	Magnetic force
μ_0	Magnetic permeability of free space
M	Mass
a	Acceleration
F_i	Force
F_d	Force performing on the moving unit.
F_c	Coulomb friction force.
F_s	Static friction force at zero velocity.
F_{load}	Disturbance force or load force.

$v(t)$	Linear velocity of the the mover.
F	Viscous friction coefficient.
R_a	Armature resistance
L_a	Armature inductance
K_b	Back electromotive force constant
K_t	Thrust constant.
T_m	The mechanical time constant
T_e	The electrical time constant

List of publication

Journal Publications:

1. M. Habil, F. Anayi, Y. Xue, and K. Alnagasa, “Analyzing the Design and Performance of a DC Linear Stepper Motor,” *Machines*, vol. 11, no. 8, p. 785, Jul. 2023, doi: 10.3390/machines11080785.

Conference:

1. M. Habil, F. Anayi, Y. Xue, and M. Shouran, “Optimisation of Sliding Mode Parameters Using Different Algorithms to Control the Position of a Linear DC Motor, Accepted.
2. M. Shouran and M. Habil, "Tuning of PID Controller Using Different Optimization Algorithms for Industrial DC Motor," *2021 International Conference on Advance Computing and Innovative Technologies in Engineering (ICACITE)*, Greater Noida, India, 2021, pp. 756-759, doi: 10.1109/ICACITE51222.2021.9404616.

Chapter 1: Introduction and Objectives

1.1. Introduction

An electric motor serves as a mechanism that transforms electrical energy into mechanical energy. These motors primarily harness the electromagnetic phenomenon, which results in the creation of a mechanical force when a current-carrying wire interacts with a magnetic field. Diverse configurations and structures of electric motors leverage this fundamental principle to generate mechanical force and motion through the utilization of electricity [1].

Rotary machines or conventional generally consist of two components: a rotating central section known as the rotor, and a stationary outer section referred to as the stator. In one configuration, either permanent magnets or electromagnets are located on one of these sections to produce a magnetic field. Meanwhile, current-carrying wires on the other section generate a secondary magnetic field. The interaction between these two magnetic fields is what facilitates the generation of rotary motion [2].

Before the advent of linear machines, rotary machines provided a solution to produce linear motion. Ball and screw, belt and pulley and other rotary solutions have been employed to convert rotary motion into translational. However, compared to linear machines, these solutions are less precise and display backlash error. While using linear machines, load can be directly coupled with the mover. Moreover, when it comes to speed, accuracy, and efficiency; linear machines are more suitable to meet these needs [3].

Linear motors are widely used in industrial applications. Many machines' tools and industrial equipment are now utilizing linear machines in designs that require linear motion due to the advantages offered by this device. The simple structure of linear motor offers high flexibility to the machine in terms of size and space [4].

Linear motors have been designed and developed by applying two fundamental operating principles. The first of these relies on the interaction between a current-carrying conductor and a magnetic field in proximity, and the second on the alignment of magnetomotive forces. There are two categories of linear motors which exploit these

principles; one is the moving-coil design that uses the first principle for the generation of motion and the other is the moving-iron design based on the second principle [5].

1.2. Research background

A linear motor produced motion in a straight line directly, without the use of a crank or any other mechanism for converting rotary motion to linear motion. The history of linear motors goes back as far as the last decade of the nineteenth century. The earliest linear electric motor emerged before 1838, after the discovery of Faraday's induction law in 1831[6].

These machines were practically forgotten for nearly half a century, but there has been a genuine revival of interest in them since the 1950s. although linear motors dispense with the need for gears, belts, and screws, which are necessary to obtain linear motion from rotary motors. The latter is still preferred because of the wide range of speed and thrust that can be obtained with the help of gearing at an economic [7].

The first DC linear motor was built in 1917, it was a reluctance motor in tubular form, and it was proposed as a launcher. The electromagnetic motor consisted of a combined series of straight induction coils in which mover is accelerated. The mover itself switched on the current in the solenoid ahead and turned off the current in the solenoid behind it, thus propelling it in an ever-accelerating motion forward, this motor was known as Birkeland's Cannon, and it was never developed beyond the model stag [8].

Figure 1.1 First DC linear motor [8].

Conventional DC linear motors are like rotational DC motors, so they have an armature and a field system, but in the linear case the armature is stationary, and the field is moving part. In general, the armature consists of a circular bar that is made of ferromagnetic material. The linear motors can be divided into two types according to whether the rotor or stator is extended to the full length of machines. The short stator, also known as the short primary, refers to a machine where the rotor surpasses the stator in length. Conversely, the short rotor, occasionally termed the short secondary, represents a machine where the rotor is shorter than the stator. Depending on specific needs, both short stator and short rotor machines can be configured as either single-sided or double-sided [9].

A high-speed DC linear motor was built at the Royal Aircraft Establishment in Farnborough in 1954, it was a linear form of the conventional rotary motor. It was made and designed as a wind tunnel, and capable of accelerating a mass of 1kg to a speed of 500 m/s [10].

In the 1950s, owing to the development of control technology and years of experimental theory, the linear motor entered a new stage of comprehensive development [11]. During this period, Professor Laithwaite published a comprehensive monograph "Induction Machines for Special Purpose", which stimulated interest and made a significant contribution to the field of linear motors. After 1965, more and more equipment based on a linear motor was developed, such as the electric gramophone, sewing machine and conveyor device [12].

(since 1971 to the current day) In this period, linear motors entered the commercialization era. Many varieties of linear motors appeared worldwide, not only in industrial areas but also in people's daily lives. The linear motor was also developed and widely used in tools such as an automatic graph plotter, scanner recorder, and linear potentiometer [13]. [11]. By providing a direct thrust force to a payload, linear motors offer numerous advantages over rotary-to-linear counterparts. In applications requiring linear motion, linear motors offer many advantages over rotary motors [7]. The main benefits of linear motors are their ability to achieve a high force density, high positioning

precision, mechanical simplicity, higher reliability, longer lifetime, accuracy associated with the mechanical simplicity of such systems and no backlash, thus, providing a very high accuracy [14].

Permanent magnet linear motors are the most naturally suited among electric motor drives for motion control applications requiring great speed and precision. The rising industrial applications of PMLMs in various semiconductor processes, accurate metrology, and miniature system assembly are unambiguous proof of PMLMs' effectiveness in satisfying the rigorous requirements of these application areas. The key benefits of a PMLM are its high force density, decreased heat losses, and, most importantly, its high precision and accuracy as a result of its simple mechanical structure. Unlike rotary machines, linear motors do not need indirect connection techniques like gearboxes, chains, or screws. This reduces the effects of contact-type nonlinearities and disturbances, such as backlash and frictional forces, especially when paired with aerostatic or magnetic bearings. Nevertheless, the inherent ability to attenuate the effects of model errors and external disruptions [15], and the advantages of mechanical transmission are lost. If high-speed and high-precision motion control is to be carried out, it is of the highest importance that these effects be reduced, either by a suitable physical design or via the control system. The phenomenon of force ripple originating from the magnetic structure, which has position- and velocity-dependent features, has a significant and well-known nonlinear effect on the dynamics of the PMLM. This is a significant factor inhibiting PMLM performance [16]. Several technological apps also encounter intermittent outages. In data storage systems, for instance, the eccentricity of a disc's track needs periodic read/write head movement synchronised with the disk's rotating frequency. Torque pulsations occur at the frequency of rotation of rotary type DC motors and stepper motors [17] due to the tendency of permanent magnets to align themselves along the paths of least resistance. In switched reluctance motors, torque ripples develop as a result of the saturation effect and the variation in magnetic reluctance, which result in highly nonlinear features that create torque ripples. Many efforts have been devoted to solving the challenges that nonlinear ripple effects provide. A neural network feedforward controller is proposed by [18] to reduce positional inaccuracy caused by recurring and slow time-varying

disturbances. Yao and Tomizuka [19] created an adaptive robust control approach, which was subsequently applied to the high speed and high-accuracy motion control of machine tools. A radial basis function is used as part of a composite control system in [20] to remove errors caused by nonlinear uncertain remnants that were not accounted for by the linear control. [21] describes the implementation of iterative learning control for applications needing repeated iterative operations. Even though all of these experiments focused on adjusting for nonlinear uncertainty, there has been no explicit modelling of the ripple force phenomena and, thus, no direct effort to diminish these forces. Adaptive techniques are used because motion systems are subject to time-varying drift and disturbances, requiring ongoing control adaptation to these changes for optimal performance.

Despite these advantages over rotary counterparts, linear motors have not been able to totally replace conventional techniques A prominent nonlinear phenomenon significantly influencing the dynamics of Slotless DC Linear Motors (SDLMs) is the occurrence of force ripple. This phenomenon emanates from the inherent magnetic structure and manifests characteristics that are contingent upon both position and velocity variables. Force ripple represents a prominent constraint that substantially restricts the overall operational performance of (SDLMs), this factor should be overcome by explicitly taking them into account in the design of the motor and the controller.

1.3. Research Gap and Problem Statement

Force ripple reduction is an important factor in linear motor control as it impacts on the motion of the industrial applications and affects the system performance. Force ripple refers to the variation in force produced by the linear motor as it moves along its path. This variation can be caused by several factors, including variations in the magnetic field strength, non-uniformities in the winding or iron core, and other mechanical or electrical factors.

When a force ripple is present, it can cause undesirable effects such as vibration, noise, and reduced precision in the motion control system. In some applications, such as precision machining or optical positioning systems, even small variations in force can

cause significant errors or damage to the system.

Therefore, reducing force ripple in linear motors is crucial for achieving precise and smooth motion control, guaranteeing a fast dynamic time response. This can be done through various techniques such as optimizing the design of the motor, using feedback control, or applying compensation algorithms to the control system. By reducing force ripple, the linear motor can achieve better performance, accuracy, and reliability, making it a more effective solution for a wide range of applications.

addressing ripples in linear motors involves a multidisciplinary approach that combines improvements in magnetic design, control systems, mechanical components, and manufacturing processes. By focusing on these aspects, the performance of linear motors can be significantly enhanced, leading to smoother operation and reduced ripples.

1.4. Aim and Objectives.

The aim of this research programme is:

Design and Development of a New Slotless DC Linear Motor and Adaptive Control System using Bee's Algorithm to improve the overall performance, application precision, and accuracy.

The objectives are:

- To undertake a thorough analysis of slotless DC linear motor control, investigate the key findings, in progress studied subjects, and the potential problems with the possible solutions for force ripple in modern linear systems.
- To design and model the slotless DC Linear motor using “MagNet” software.
- To construct the slotless DC Linear motor and assess its viability for use in linear motion systems.
- To derive the mathematical model of the linear DC actuator for the design the proposed controller.
- To design and apply the disturbance observer with sliding mode control to the system to limiting the force ripple.
- To compare and analysis the simulation result of position and speed in MATLAB/SIMULINK with the experimental result in the same condition.

1.5. Research Methodology

- A new design of slotless linear DC motor is introduced to reduce the cogging force, which caused by the slotting of iron-core translator.
- Sliding mode control (SMC) with disturbance observer (DOB) is proposed, where a DOB is employed for disturbance rejection and improve the robustness of SMC.

1.6. Research Programme Contribution to Knowledge

The contributions of this work are as following:

- Design a new slotless DC linear motor to reduce the cogging force.
- Implementation of Sliding Mode Control with Disturbance Observer (SMC-DOB) obtained based on the mathematical model of the investigated system under the effect of force ripple.
- Implement the Bees Algorithm (BA) for the first time in DC linear motor to the tuning the parameters of the control method (sliding mode control) with disturbance observer to improve the performance of slotlss linear DC motor under the effect of disturbance.

1.7. Thesis Structure and Organisation

There are six chapters in this thesis. In order to providea a quick understanding of the several ways to conduct a linear movement, Chapter 2 provides a categorization of linear motors overview. Also, a short overview of the various linear motor types and their topologies is provided. The prior research on the design of linear motors and methods for reducing force ripple is discussed at the end.

Mathematical model of DC linear motor is achieved in chapter 3, where a mechanical and electrical model is calculated by using Newton and Kirchhoff law respectively. Also in this chapter, the modelling of the problem statement is carried out, by using LuGre model, the friction model is designed. Then, calculation of total force ripple is achieved with an estimated parameter. The model of the system with the frictional and force ripple have been designed and tested using MATLAB / Simulink. Also, on the basis of

the created preliminary geometry, a Finite element method (FEM) analysis is used to modelling and design a linear dc motor. A comparison between the modelling and real design is carried out, in terms of the static thrust, air-gap flux density and magnetic flux distribution. In chapter 3 also covers mesh building, boundary condition specification, and excitation source pre-processing activities. In addition, the selection of the optimal materials for the magnetic circuit and the justifications for their favour are also covered.

Sliding mode control with disturbance observer is designed and implement on the slotless DC linear motor under the disturbance in chapter 4. The control low is calculated according to parameters of the linear dc motor, frictional and force ripple. Also, simulation analysis is carried out using MATLAB to verify the performance of the proposed nonlinear controller with disturbance observer and the effectiveness of the control strategy for position and speed.

Also, this chapter (4) Describes the proposed algorithm "the Bees Algorithm" and provides some applications in which it has been used. It describes the fundamental notion of business analysis, the theoretical analysis done on BA, and its primary applications. As a new application of BA, this method is used extensively in this thesis to determine the optimal settings for the controllers described in chapters 4 in order to achieve the optimum performance.

In chapter 5 an outline of the experimental setup for real time implementation of close-loop velocity and position controllers has been presented. LabView is used to carry out experimental testing in order to confirm the viability of the suggested control strategy, while the LabVIEW maths module is used to develop the SMC-DOB. A brushless DC linear motor, a laser distance sensor, a power source, an Arduino Mega microcontroller, and a PC make up the experimental set-up. The experiment involves controlling position, speed, and adding a load on the mover to assess the stability of the control approach. In this chapter, a comparison between simulation and experiment results is presented.

Finally, conclusions of this research and recommendations for future work are presented in chapter 6.

Chapter 2: Literature Review

2.1. Introduction

The pursuit of enhanced precision, efficiency, and versatility in electromechanical systems has led to continuous advancements in motor technology. Among the most notable innovations in this domain is the emergence of the slotless DC linear motor, a dynamic solution that has found wide-ranging applications in various industrial and scientific domains. Unlike its conventional rotary counterparts, the slotless DC linear motor offers a distinctive linear motion mechanism that eliminates the need for mechanical commutation. This innovation has paved the way for a spectrum of benefits, including reduced mechanical wear, improved precision, and higher responsiveness. As a result, the slotless DC linear motor has become an attractive choice for applications necessitating precise and rapid linear motion [22].

Linear and rotational motors run on closely aligned principles and have analogous structures, with the linear version being like the rotating motor but cut on a radial plane which is unrolled, figure 2.1. This creates a direct electromagnetic linear actuator capable of producing electric-speed linear movement, with no contact, meaning that issues of maintenance and reflux are removed. Thus, linear motors can be defined as an electromechanical device that produces linear motion along a single axis by utilizing electromagnetic forces without the need for rotary-to-linear mechanical conversion mechanisms [23].

Linear motors offer a notable advantage over the more conventional linear motion systems, which often involve the use of rotary electric motors and ball screw mechanisms. In traditional setups, rotary motors are adapted to produce linear motion through additional components like screws or balls, which can introduce mechanical complexities, friction, and inefficiencies into the system. These mechanical components can result in issues such as backlash, wear, and reduced precision. The advantages of linear motors are high speeds or acceleration rates, faster dynamic time response, more stiffness and without backlash. Therefore, linear motors are used in many application domains [22].

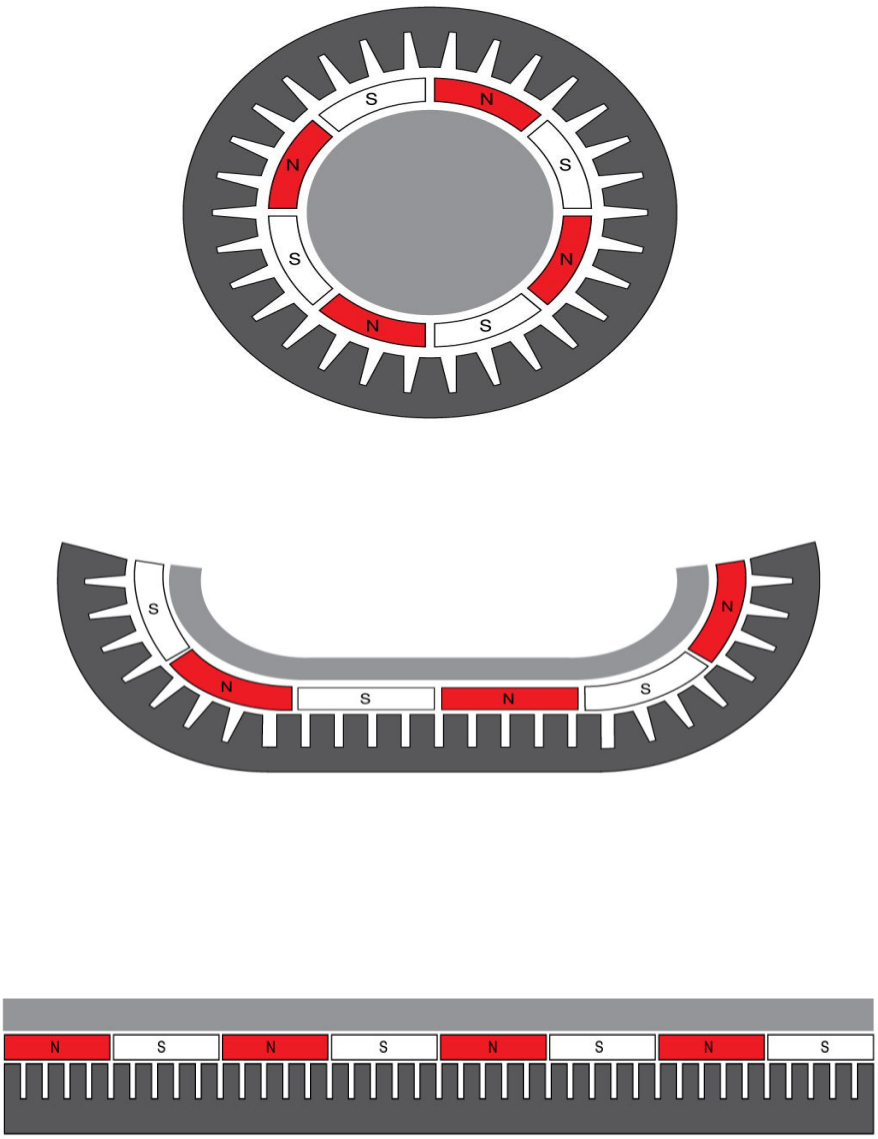

Figure 2.1 The process of unrolling rotary motor to become linear motor [23].

2.2. Classification and Topology of Linear Motors

Figure 2.2 shows the main classifications of linear motor, which are especially based on

the geometric structure of the devices, as flat or in tube form. The two geometrical types are then structured topologically to form long or short stators. Flat linear motors may be constructed with one side or two opposing sides (a double-sided motor).

Short and long stators have the following characteristics: in short stators, the windings and primary electrical components are the same length or shorter than the secondary component. In general, movement is seen in the part with the electrical supply. This type of motor is generally used in machine tools [24].

Providing a classification is challenging due to the individual perspectives of each author, which can result in differences in categorization based on factors such as excitation methods, power supply components, or other considerations [24].

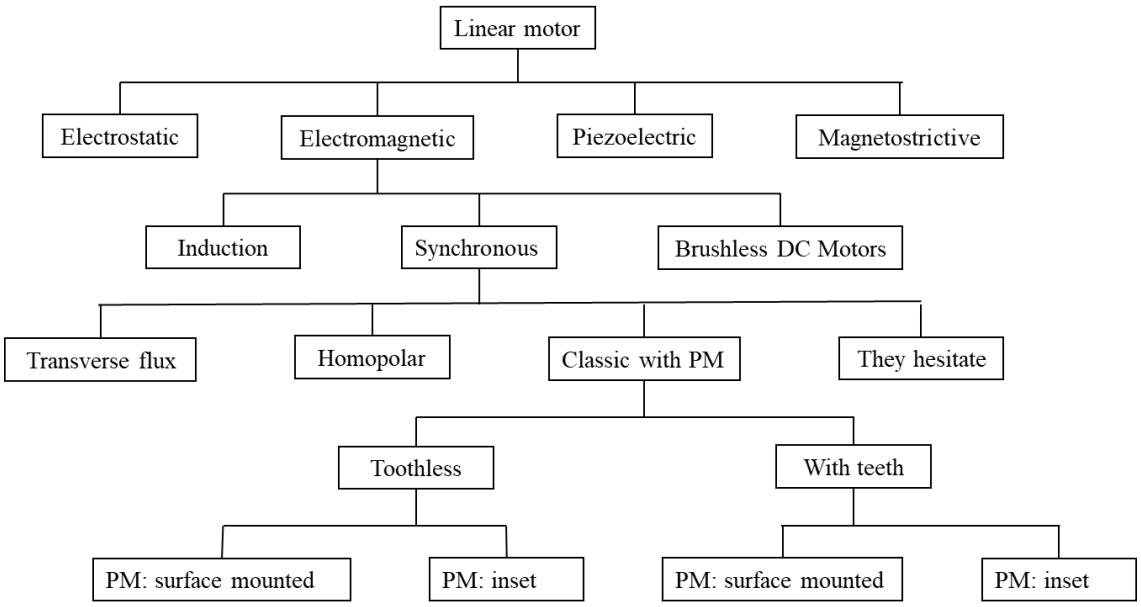

Figure 2.2 Linear motor classification [24]

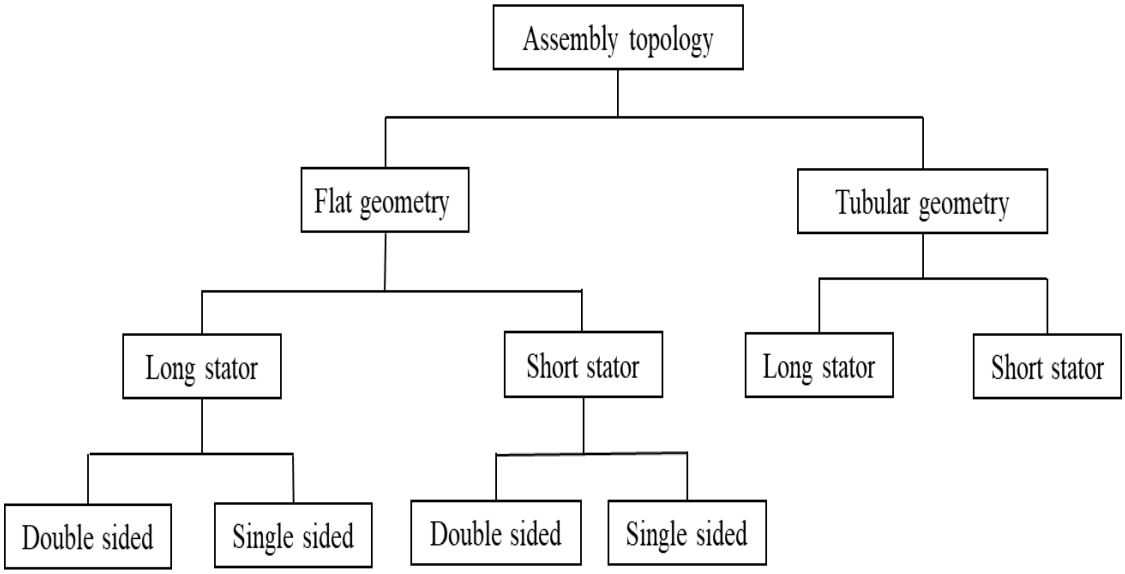

Figure 2.3 The main topologies of linear motor [15]

Linear motors can be classed as tubular in form if primary and secondary parts form a coupling rather than flatbed form, while motors in either category can be long or short stator type, indicating long or short primaries. The long stator linear motors have longer electrical supplied parts (primary, winding) in comparison with secondary parts. In this case, the secondary parts are moving (moving track – static forcer). Meanwhile, a short stator linear motor has greater length in the secondary components, while the primary components move (i.e. with a moving force and static track). In addition, a flat linear motor may be single or double-sided linear motors, based on how many primary/secondary components there are and how these are organised. The linear motor can also be categorized based on their electrical elements, with similar types to the rotational motor, including the linear induction motor (LIM), linear DC motor, linear stepper motor and linear synchronous motor (LSM) [3].

In linear induction motors, the primary induces excitation through the conduction layer, generating a magnetic field within the airgap and thus inducing voltage within secondary parts. As the magnetic field and secondary induced current interact, they create electromagnetic force. LIMs are simply designed and therefore are a lower-cost option in comparison to LSM.

Linear synchronous motors generate linear movement synchronously with the airgap's

induced magnetic field. Generation of thrust occurs through the PM-generated magnetic field and the primary-generated magnetic field. LSM gives a greater thrust density in comparison with LIM.

DC linear motors (DCLMs) rely on a DC to provide excitation current. Generation of thrust is achieved through magnetic field interactions produced through PM-produced magnetic field and switched DC current. The typical DC linear motor is a 2-unit construction, consisting of a permanent magnet, providing primary airgap flux, and an armature. One of these units forms the moving part, and this part is generally shorter. The other unit dictates how long the motor's track is.

The unit in the motor containing current flow through the windings, producing electromagnetic flux, is termed the active part, while the magnet over the airgap is termed passive. The stator may be passive or active, and is the part which does not move, while the section which moves, which also may be passive or active, is the mover/translator [6]. For the purposes of the thesis, the term "mover" is used to denote the permanent magnet responsible for generating the primary magnetic field. Conversely, the term "stator" refers to the motor armature, which consists of the winding and the stator core.

2.3. Linear motor types

Linear motor design principles primarily revolve around two fundamental operational concepts. The first entails employing a conductor through which electric current flows and establishing interaction with a proximate magnetic field. The second approach centres on aligning magnetomotive forces. These principles underpin two distinct linear motor types: the moving coil linear motor, which hinges on the interaction between conductor currents and magnetic fields to induce motion, and the moving magnet motor, which orchestrates magnetomotive forces to achieve mechanical work [25].

2.3.1. Moving magnet motor

A simple magnet motor design contains a moving armature fitted with magnets as well as a support member forming a pathway of return for magnetic flux. It is possible to create the stator with steel laminate stampings and the insertion of windings in a similar

way to the rotary motor. Moving magnet motors can have advantages where there is a need for strong linear forces or if the motor needs to be simple. Figure 2.4 shows an illustration of a single-sided moving magnet type of linear motor with high-strength magnetic attraction from stator to magnet unit, forming a force which runs orthogonally in relation to linear force. This can create high bias loads on the linear bearings. This can be balanced by including two stators: one on each side of a magnet assembly (the moving part), meaning that most magnetic forces of attraction cancel each other out [26].

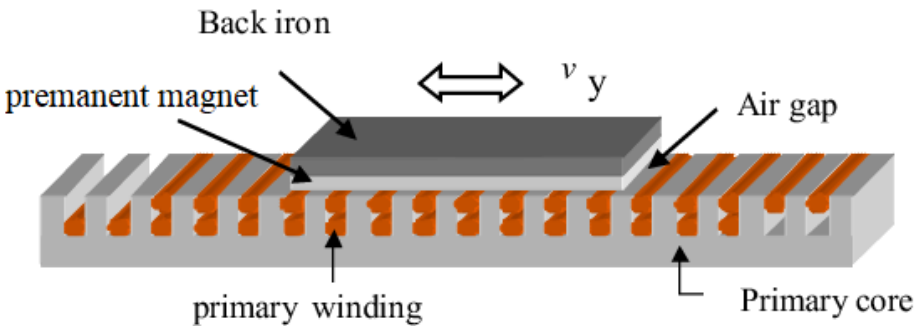

Figure 2.4 Moving magnet motor [28]

2.3.2. Moving armature motor

Moving armature motor types contain an assembly of windings and core laminations which is shorter than stator, and a longer stator unit which contains a lengthy magnet assembly, mounting the magnets onto a surface which magnetism can permeate. These motors have characteristics which are essentially similar to those in the moving magnet type, with the exception of the interfacing of each winding with neighbouring magnets. This increases efficiency, although meaning that more magnets are required. In addition, this type of design needs flexible winding cable (see Figure 2.5) [27].

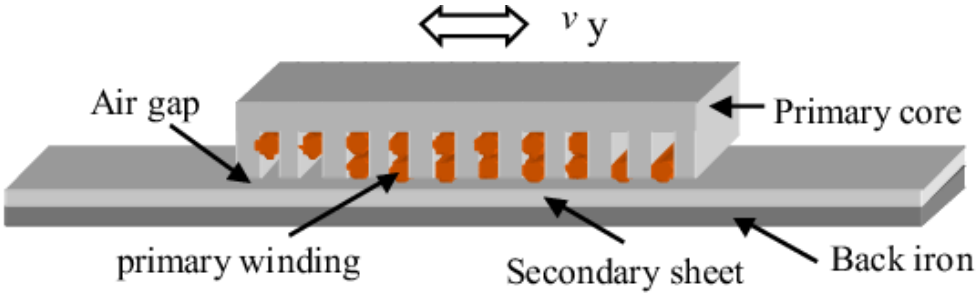

Figure 2.5 Moving armature motor [27]

2.3.3. Moving coil motor designs

There are many similarities between the moving armature and moving coil motor, but the moving coil motor has no iron in the moving assembly, with just conductor and supports. This type of motor has a balanced magnet construction: however, it is also possible to have an assembly which has magnets on a single side, with the other side hosting a flux return path. Moving electrical forces generate magnetic forces, which are generated through a conductor within a magnetic field. A permanent magnet is typically used to provide this field, with the forces generated being in direct proportion to conductor current [28].

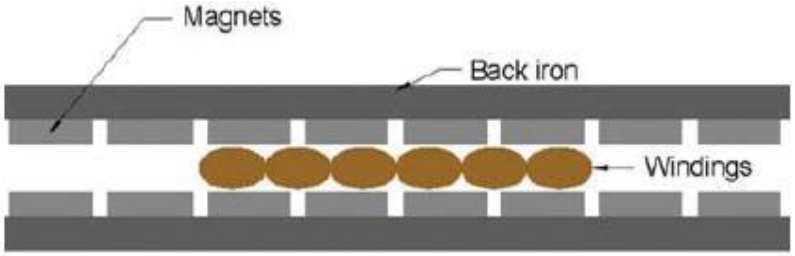

Figure 2.6 Moving coil motor [29]

The moving coil has a lighter armature and gives the greatest proportion of force to inertia. Designs can include forces with very small force ripples are possible as there is no reluctance force, and low inertia moment means that motion can be incremental, allowing very rapid acceleration/deceleration. Thermal resistance in this type of motor is comparatively high between the surrounding air and the armature, meaning that cooling techniques may need to be applied to the coils when increments are high [29].

Table 2-1 Features of different linear motor types.

Linear motor	Moving magnet	Moving armature	Moving coil
Weight of moving unit	Medium	Heavy	Light
End effects	Present	Present	Absent
Power loss	High	Medium	Low
Moment of inertia	Medium	High	Low
Reluctance clogging	Moderate	Moderate	None
Volume of magnets	Low	Medium	High
Cost	Moderate	Low	High

2.4. MAGNETIC MATERIALS

Materials are categorised based on μ_R as relative permeability. This categorization gives rise to three distinct groups: ferromagnetic materials ($\mu_R > 1$), which exhibit high relative permeability and are characterized by strong magnetic properties; electrical conductor materials ($\mu_R < 1$), recognized as diamagnetic materials, with low relative permeability, and materials with limited magnetic response; and electrical insulator materials, known as paramagnetic materials, featuring moderate relative permeability and displaying magnetic characteristics within a specified range [30].

The flux density in the air gap can be expressed as:

$$B = \mu_0 H \qquad (2.1)$$

Where B is representing flux density, H is the magnetic field strength.

And μ_0 , is the magnetic permeability of free space:

$$\mu_0 = 4\pi \times 10^{-7}\, H/m \qquad (2.2)$$

It is necessary to adjust (2.1) in a material for descriptions of non-free space magnetic

phenomena:

$$B = \mu H \qquad \mu = \mu_R \mu_0 \tag{2.3}$$

In which permeability is given by μ, with μ_R giving relative permeability as a nondimensional constant. However, material-based permeability can only be applied where the material shows homogeneity in quality and isotopism. Homogeneity signifies a consistent and uniform composition and quality throughout the material, ensuring that its properties remain identical in all parts. Simultaneously, isotopism denotes that the material's magnetic behaviour remains consistent regardless of the direction from which magnetic fields are applied. Additionally, (2.1) shows nonlinearity in several frequently found materials and μ is variable based on B, leading to a range of subcategories of permeability descriptions which relate to materials' non-linear B-H properties.

Since the majority of materials which are magnetic show nonlinear properties, graphical approaches can be beneficial to describe these materials' magnetic properties. The primary properties from these are the hysteresis loop and the magnetisation characteristic or B-H curve [31].

2.5. Hysteresis of Ferromagnetic Materials (B-H Curve)

As a sample is magnetised and demagnetised, induction flux density (B) lags behind the applied magnetic field strength (H), being termed ferromagnetic hysteresis. The B-H curve plots applied field strength against induction flux density as ferromagnetic specimens are magnetised and demagnetised [32].

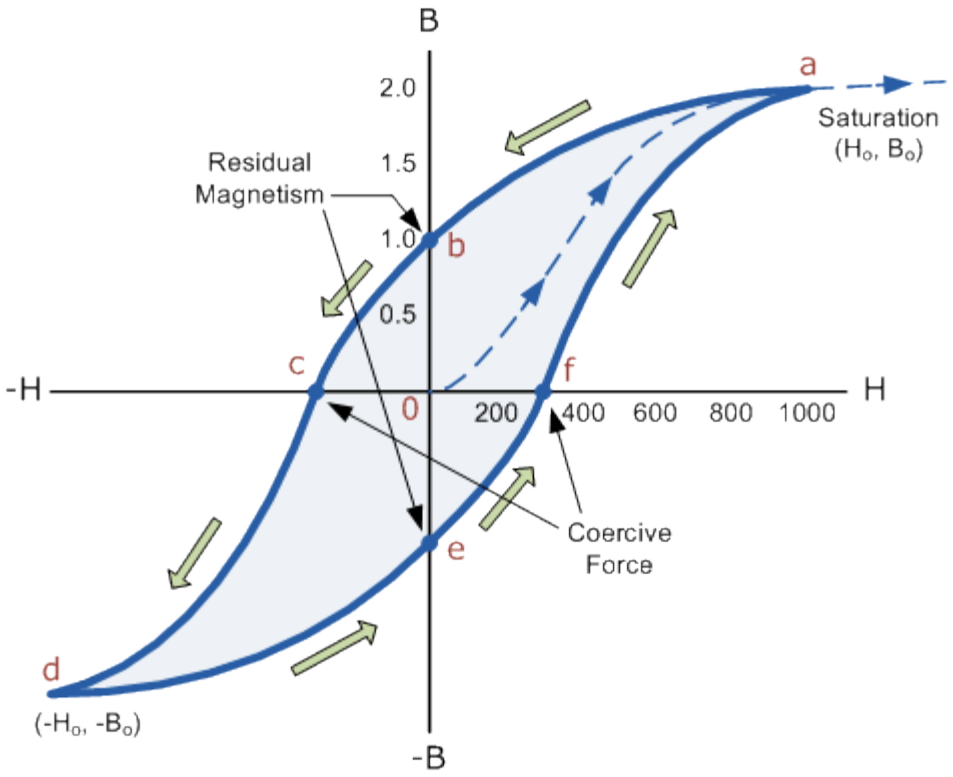

Figure 2.7 B-H curve of a typical magnetic material [33]

The graph of the Magnetic Hysteresis loop illustrates the behaviour of a ferromagnetic core, depicting the non-linear relationship between the magnetic field strength H and the flux density B. At point 0 on the magnetisation curve, both B and H are at zero as the core is unmagnetized. As the magnetisation current i increases, the magnetic field strength H increases linearly, causing the flux density B to rise towards saturation, represented by point a.

When the magnetising current is reduced to zero, the magnetic field strength also reduces to zero, but the residual magnetism in the core means that the flux density will not reach zero, as shown by the curve from point a to point b. Reversing the current flowing through the coil generates a coercive force, which nullifies the residual flux density and demagnetises the core at point c.

Increasing the reverse current causes the core to be magnetised in the opposite direction, reaching saturation at point d. Reducing the current to zero yields the residual magnetism in the opposite direction, point e, which can be eliminated by reversing the

magnetising current into a positive direction, resulting in the magnetic flux reaching zero at point f.

The B-H curve traces the path of a-b-c-d-e-f-a, depicting the magnetising process of the ferromagnetic core, which depends on its previous history and creates a form of "memory" in the material. Soft ferromagnetic materials, such as iron or silicon steel, have narrow magnetic hysteresis loops and small amounts of residual magnetism, making them suitable for use in transformers, relays, and solenoids, as they can be easily magnetised and demagnetised.

However, closing the hysteresis loop requires applying a coercive force, which dissipates energy as heat in the material, resulting in hysteresis loss. The amount of loss depends on the material's coercive force value. Adding additives, such as silicon, produces materials with narrow hysteresis loops and small coercive forces, called soft magnetic materials, that are easily magnetised and demagnetised. [34].

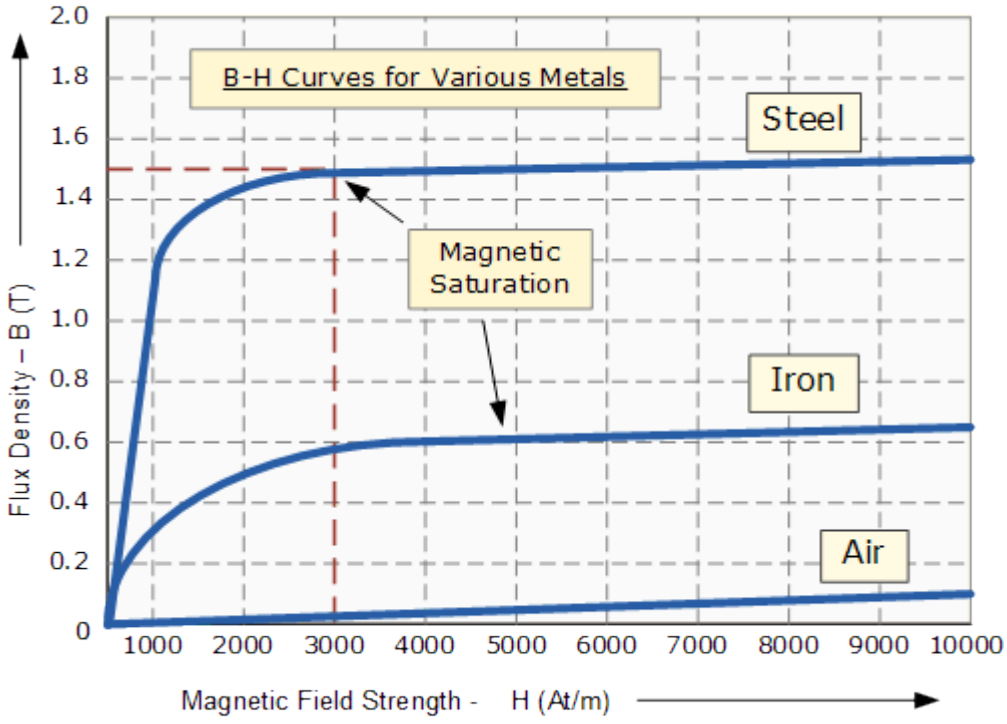

Figure 2.8 Magnetisation curves [35] .

The magnetisation curves in Figure 2.8 show typical B-H relations in both steel and soft-iron cores: different core materials have different curves for magnetic hysteresis. It can be seen that flux density rises proportionally in line with field strength up to a given

value after which no more growth is possible, levelling out to nearly constant while field strength rises further. This occurs due to limitations on how much flux density the core can produce, with perfect alignment of every domain within the iron. Additional increases do not impact magnetisation, and magnetic saturation, or saturation of the core, is achieved at the point where maximum flux density is reached. In Figure 2.8, saturation is reached for the steel at approximately 3,000 ampere-turns per metre.

Saturation is reached due to changes in the randomly organised structure of molecules as the magnets at molecular level increasingly line up. With growth in the strength of the magnetic field strength, H, the molecular magnets increasingly align to eventually be completely aligned, which generates peak flux density. After this point further increases in H caused by electric current in the coil do not have any significant impact [35].

Magnetisation and demagnetisation are simple for soft magnetic material as the energy required for this is low, with such materials having a coercive field lower than 1000A/m. Moreover, with this type of material, domain growth is not difficult to achieve, and the main uses of such materials is for increasing flux and/or creating a pathway for current-produced flux. Soft magnetic materials are assessed based primarily on their coercive force, permeability, which allows the reaction of materials to an applied magnetic field to be predicted, capacity for current conduction (electrical conductivity), and the maximal magnetic field which can be generated by the material (saturation magnetisation).

2.5.1. Hysteresis Loop of soft magnetic materials

Materials create a hysteresis loop when magnetised through exposure to an alternating magnetic field. This loop has a limited area in soft magnetic materials, as shown in Figure 2.9, meaning that there is little hysteresis loss.

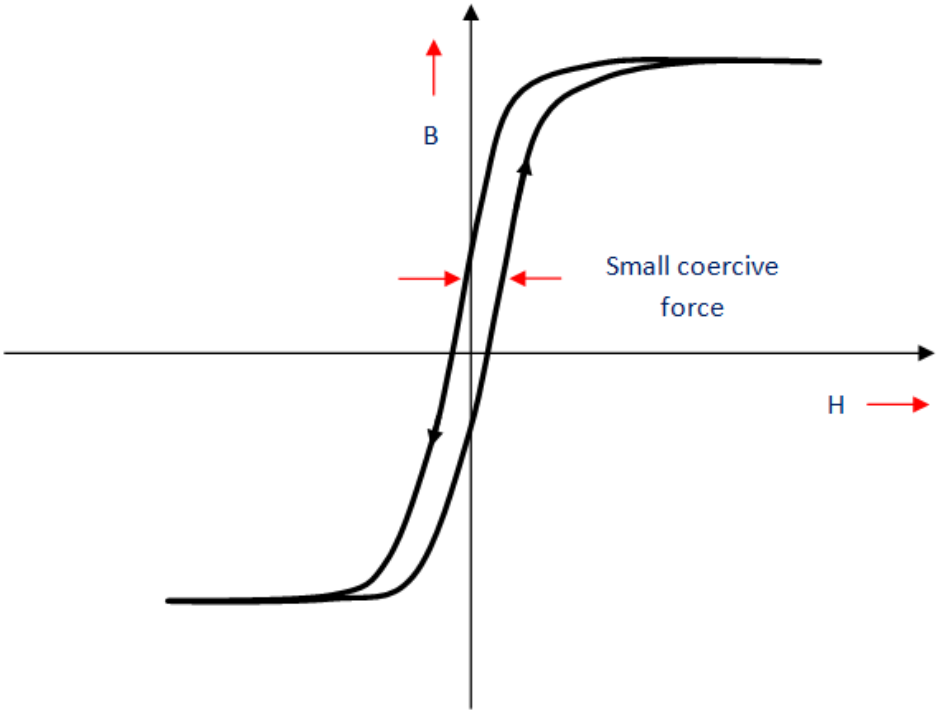

Figure 2.9 Hysteresis loop of soft magnetic materials [36].

Soft Magnetic Material properties are:

- Maximum permeability.
- Low coercive force.
- Low losses from hysteresis.
- Low remnant induction.
- Strong saturation magnetisation

Relevant soft magnetic materials include pure Iron, which refers to iron with less than 0.1% carbon. Refining pure iron gives maximal permeability while lowering coercive force based on appropriate methods which produce soft magnetic material. However, this material generates eddy current loss under conditions of strong flux density because it has poor resistivity. This makes it more suited to low frequency uses including parts within electrical tools and electromagnetic cores [36].

hard magnetic materials are referred to as such because of the difficulty in magnetising them. In such materials, there is no motion in domain walls due to imperfections or flaws

in crystals. However, this type of material remains magnetised once it is magnetised leading to it being termed permanent magnetic material. These materials show a coercive force of over 10 kA/m, with strong retentivity. The application of an externally sourced magnetic field to a hard magnet for the first time to lead to growth and rotation of the domain towards alignment with the field applied when magnetisation becomes saturated. Removal of the field follows. This reverses magnetisation to an extent: however, the magnetisation curve is not traced after this. The magnet stores a given quantity of energy, termed Br, being magnetised permanently.

2.5.2. Hysteresis Loop of hard magnetic materials

The hysteresis loop's overall area is equal to the energy dissipated through magnetisation of a unit volume material within one operational cycle. This area is significant for all hard-magnetic material due to the significant coercive force present (see Figure 2.10).

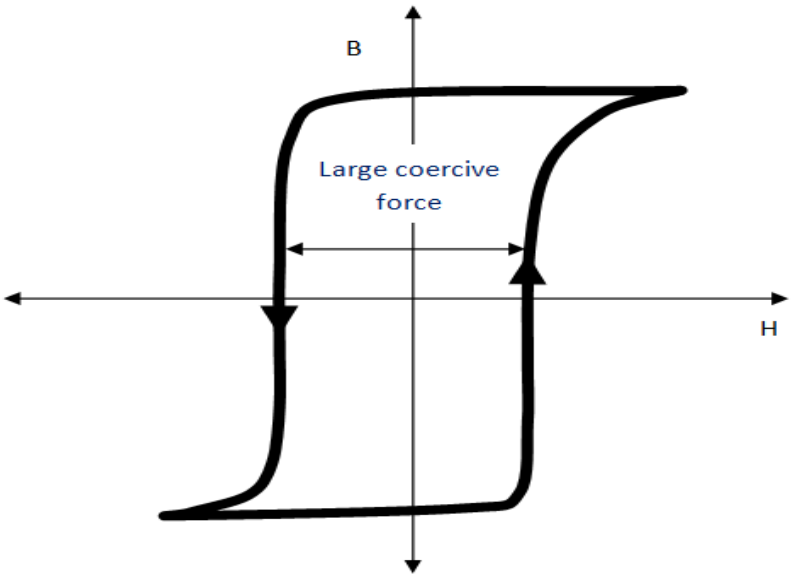

Figure 2.10 Hysteresis loop of hard magnetic materials [13].

BH as a product is not constant over the demagnetisation curve. An effective permanent magnet shows maximum product value, or (BH)max. It should be noted that such BH suggests energy density (Jm^3), termed energy product.

Hard Magnetic Material properties are:

- Maximum coercivity and retentivity.
- A high BH (energy product)
- The BH loop is almost rectangular.
- The hysteresis loop is large.
- Permeability begins at a low level [13].

Soft ferromagnetic/permeable magnetic materials enable the easy passage of flux lines and are not difficult to magnetise or demagnetised. Magnetising soft ferromagnetic materials creates a soft magnet.

Hard ferromagnetic/permanent magnetic materials can hold a magnetic field after removal of a magnetising force. Such materials are known as hard due to the difficulty involved in magnetising or demagnetising them. These materials form a hard magnet when magnetised [38].

The fundamental disparity between soft and hard magnetic materials lies in their respective magnetic behaviour: the ease of magnetic alteration in soft materials versus the resistance to change in hard materials. This contrast governs their applications, where the former is employed for dynamic magnetic scenarios, and the latter for the establishment of durable, unchanging magnetic fields.

2.6. Magnetic Circuit Analysis

Materials for permanent magnets have developed quickly and their use has spread to a range of sectors in industry, with permanent magnet machines being used instead of the previous induction motors, due to them being more efficient and taking up less space. Selecting gradings of permanent magnets and approaches for maximising power gain is based on a sound understanding of the behaviour of these materials within electrical machine systems. Based on this, the behaviours of permanent magnet materials should be thoroughly investigated prior to analysing the magnetic circuit.

2.6.1. Permanent Magnet Material Properties

Permanent magnet materials' properties can be plotted on a graph to illustrate practical

relationships linking the intensity of the magnetic field of the magnetic specimen in A/m, represented by H, externally applied field magnitude, and B as the magnetic outputs in T (Tesla). Figure 2.11 illustrates this, in which the plot or demagnetisation curve is seen in the top left quadrant and gives a detailed understanding of the behaviour of a material in practice, as well as its capacity to withstand various magnetic loads. The demagnetisation curve represents the material characteristics of a magnet rather than being related to magnet size [39].

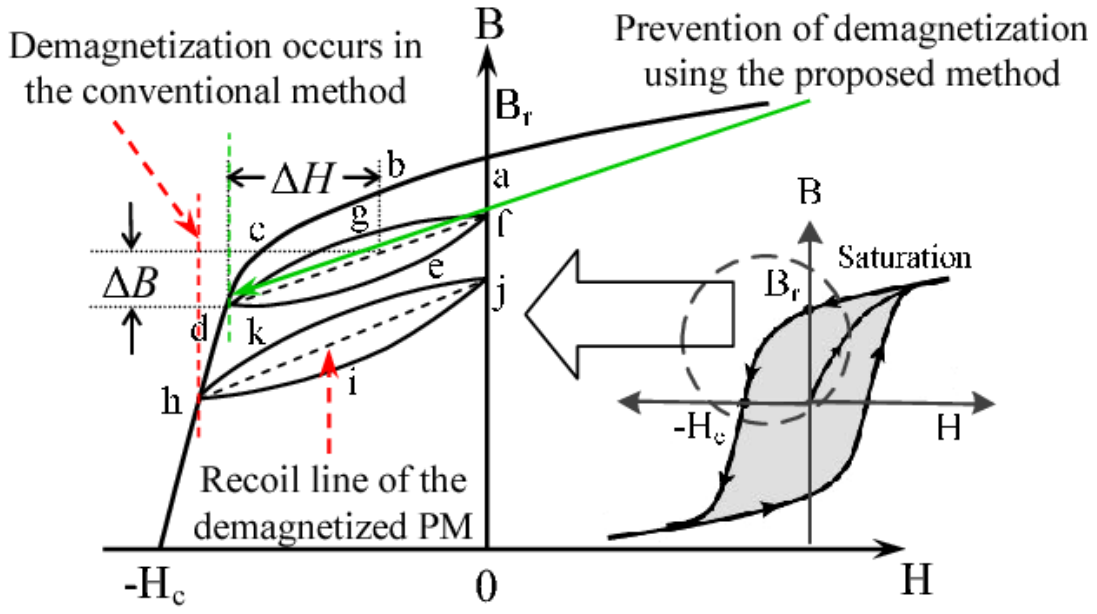

Figure 2.11 Demagnetization curve of a permanent magnet (PM) [40].

In the absence of current flowing through the armature windings, the operation of the permanent magnet relies on intrinsic coactivity and the remnant magnetic flux density, represented by H_c and B_r respectively. Application of reverse magnetic field intensity reduces magnetic flux density, which reaches point K. K as the magnetic material's operational point is where the PM demagnetisation curve intersects with the loading line, forming the Permeance Coefficient. After removing reverse magnetic field intensity, B as density of magnetic flux reaches f again, following a minor hysteresis loop. Typically, the operational point of the magnet can rise and fall in a reversible manner in the small hysteresis loop. The straight 'recoil line' often replaces this loop

[41].

The following equation broadly represents the relationship between magnetic flux density, intrinsic magnetization, and magnetic field intensity (B_{m}, B_i and H respectively):

$$B_m = \mu_0 H + B_i \tag{2.4}$$

2.6.2. Magnetic Circuit Analysis for a Permanent Magnet Motor

Analysis of magnetic flux within magnetic circuits involves treating these circuits as comparable to electric circuits, with magnetic flux ϕ being analogous to the current I, magnetomotive force taking the place of V, voltage, and magnetic reluctance Ɍ being comparable to R, resistance. Calculation of the relationships linking these factors for a reluctance network is performed as follows: [41]

Permanent magnet designs generally focus on identifying the size parameters and specification of materials which will generate the desired magnetomotive force to address magnetic circuit reluctance and create the flux necessary for the airgap [42].

There are three main components in the linear motor magnetic circuit: a permanent magnet, airgap, and iron flux pathway. The MMF which is produced by the PM determines the total flux generated in the external circuit.

$$MMF = \Phi . \Re \tag{2.5}$$

In which Φ = flux, MMF = magnetomotive force and Ɍ = reluctance

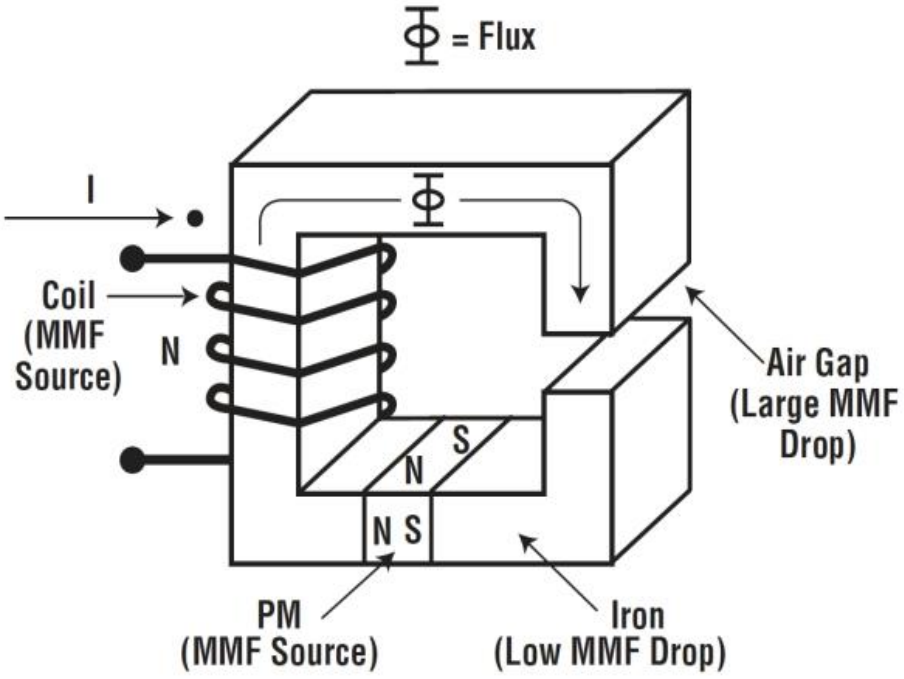

Figure 2.12 Simple magnetic circuit with permanent magnet (PM) [43].

Disregarding the yokes and the mild steel core of the armature's magnetic reluctance Figure 2.12 illustrates the magnetic flux pathway. The figure gives just a single PM block, but it can be assumed that the motor's remaining blocks will have an identical flux path. Permeability of the core is assumed as infinite; the core's H has been disregarded. Recognizing that the MMF acting on the magnetic circuit that shown in Figure 2.12 is zero can be written as:

$$\text{MMF} = k_r L_g H_g + L_m H_m \tag{2.6}$$

Or expressed as:

$$H_g = -\frac{H_m L_m}{k_r L_g} \tag{2.7}$$

With H_g representing the airgap's magnetic field intensity, and H_m representing intensity of the field within the PM. The reluctance factor is given by k_r. Flux throughout the circuit is continuous.

$$\phi = B_m A_m = q B_g A_g \tag{2.8}$$

$$B_m = \frac{q.A_g B_g}{A_m} \tag{2.9}$$

In which B_g represents the airgap magnetic field density, B_m is the PM's magnetic field density, and q represents leakage factor. $\mu_\circ$ is airgap permeability, leading to the following equation:

$$B_m = \frac{H_g k_r L_g \, \mu_\circ}{L_m} \tag{2.10}$$

$$B_m = \frac{H_g k_r L_g \, \mu_\circ}{L_m} = \frac{q.A_g B_g}{A_m} \tag{2.11}$$

Equation 2.11 demonstrates that magnetic field density and intensity relate to each other in a linear manner, through the load line (see Figure 2.13)

The demagnetization curve, also known as the B-H curve or magnetization curve, depicts the relationship between the magnetic field strength (H) and the magnetic flux density (B) in a magnetic material. It shows how the material's magnetic properties change as an external magnetic field is applied and removed. This curve demonstrates the material's ability to retain magnetism and its susceptibility to becoming demagnetized under different levels of external magnetic influence. [44].

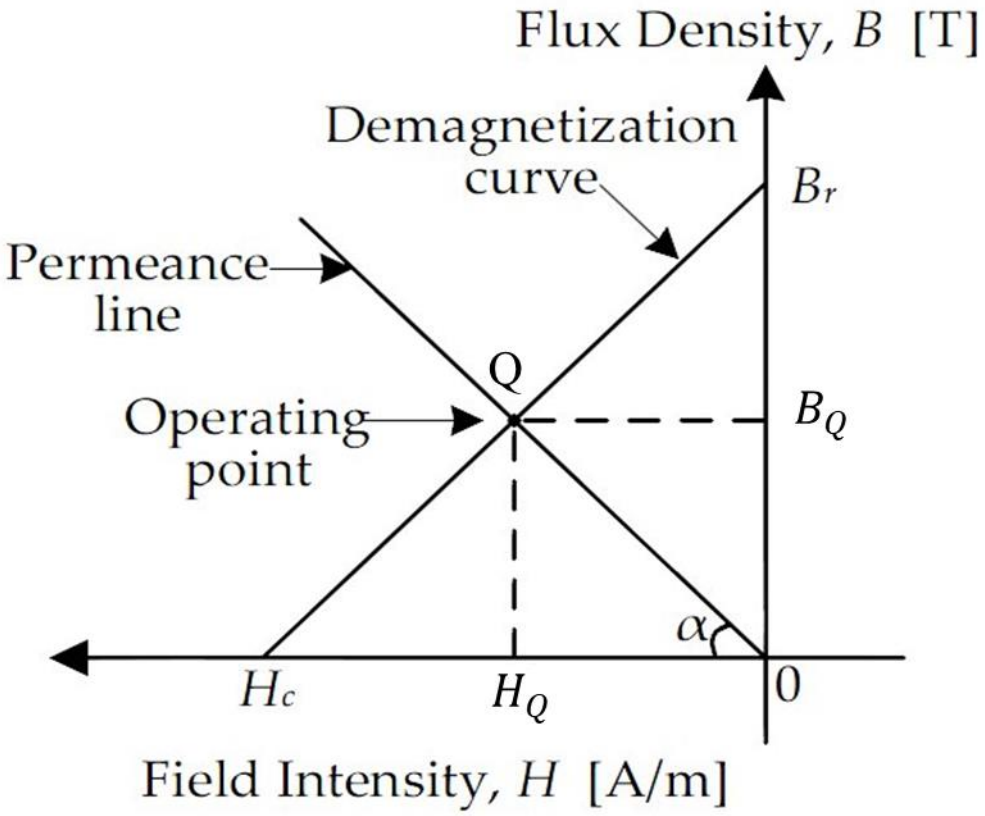

Figure 2.13 PM demagnetisation curve and load line [45].

Figure 2.13 has two lines, representing the PM's demagnetisation curve and permeances line, which is straight. The demagnetisation curve can be shown as follows:

$$B_m = tan\alpha\ H_m + B_r \tag{2.12}$$

The demagnetisation curve's slope is:

$$tan\alpha = \frac{B_r}{H_c} \tag{2.13}$$

$$B_m = \frac{B_r}{H_c}\ .H_m + B_r \tag{2.14}$$

The intersection Q of the demagnetisation curve and load line in the figure shows the PM operation point.

2.7. Force ripple

PM sloless linear DC motors are capable of direct transformation of electrical energy to

mechanical force, and do not need other devices or tools to achieve this. This type of motor offers benefits in comparison to conventional motors, for which other devices are required for conversion of rotary to linear motion. PM brushless linear motors are more accurate, give significant power and offer reduced friction and backlash. Linear and rotary motors differ mainly in the linear motor's airgap, which is open, and its mover, which has a finite length. These features impact upon the motor's transverse and longitudinal magnetic fields in the PM linear motor, instigating the end effect, in which force ripple is produced, impacting the motor's operations [46]. The ripple force transfers to the mover directly and leads to significant inaccuracies in tracking, meaning that particular linear motors present major uncertainties in linearity.

An example of this is a motor using an iron core because iron cores and permanent magnets attract each other, and this generates a magnetic cogging force an electromagnetic force ripple, with these nonlinear uncertainties transferring to and impacting upon the mover and its motion. This means that a detailed understanding of such elements is required to achieve accurate and high-performing linear motors. Various approaches are currently used to compensate for force ripple, through controls to minimise uncertainty and optimise structures to reduce such forces [47] [48].

2.7.1. Force ripple sources

Permanent magnet linear motor (PMLM) thrust force comes from multiple attracting ripple forces occurring between PMs and slots, which can be transferred to a translator by applying an electric current through the coils. Additional forces occur alongside thrust force in permanent magnet linear motors, and are known as parasitic forces, due to the LM's magnetic pattern. The majority of PMLMs produce force ripples where the winding core is a ferromagnetic material, including moving-magnet, tubular and flat type motors.

The two major force ripple sources are reluctance force and the detent or cogging force, reluctance force is originating from variations in magnetic reluctance within the motor, causing fluctuations in the magnetic force during operation, thereby contributing to force ripple. Detent or Cogging Force is results from the mutual attractive force between the permanent magnets and the iron core in the motor. It is a constant force present

regardless of the presence of an electrical current in the motor windings. The detent force, due to the interaction between the permanent magnets and the iron core, creates specific points of resistance or detent positions during motion, even when the motor is not electrically energized. Both reluctance and detent forces significantly contribute to force ripple, affecting the motor's performance and smoothness of operation, which are crucial considerations in motor design and operation. The cogging force emerges at particular times in relation to the relative locations of translator and PMs, being produced due to the fact that translators tend to become aligned in certain positions irrespective of the excitation condition. In the PM linear motor this cogging can result from two possible factors: the iron core translator's restricted length, and slotting. Reluctance force occurs based on varied winding self-inductance in relation to magnet-translator positioning. Therefore, reluctance force periodically relates to this factor. Reluctance force and cogging force jointly constitute ripple forces. With no power to the motor, ripple forces still exist as the translator travels down its guideway. Lowest and highest resistance occurs at fixed points. With low speeds, it is easier to identify ripple forces because there is less momentum against magnetic resistance [49].

2.8. State of the art of design linear dc motor

2.8.1. Wound field DC linear motor.

While the linear electric motor has existed for many decades, it was only in the 1960s that research interest grew in this type of motor as compared with rotary motor research. Nowadays, linear motors are widely applied in industry [50]

Ratcliff and Griffiths introduced a new brushed DC linear motor in the mid-1960s [51], featuring a field unit which moves as well as 4 current-supply brushes attached to the carriage and supplying the conductors of the armature. It is possible to connect this to the windings of the armature, creating series, compound, or shunt-pattern fields. A round, mild steel/ferromagnetic solid bar with conductive copper over-windings across the whole bar and winding field coils for the carriage (see Figure 2.14). Supplying power to the coils, flux is created within the carriage, illustrated by dotted lines in the figure, with the pathway of flux passing via the core of the armature and cutting the copper conductor within the airgap. Connecting the brushes in the configuration illustrated, the

magnetic field is directed along the z axis, with armature conductor currents passing between a and b, and then between c and d with the current of the armature directed along the y axis. Airgap flux cuts the conductors, causing force to emerge in the left-hand rule, at right angles to the directions taken by the magnetic field current for the armature. This allows movement of the carriage if this is not restricted.

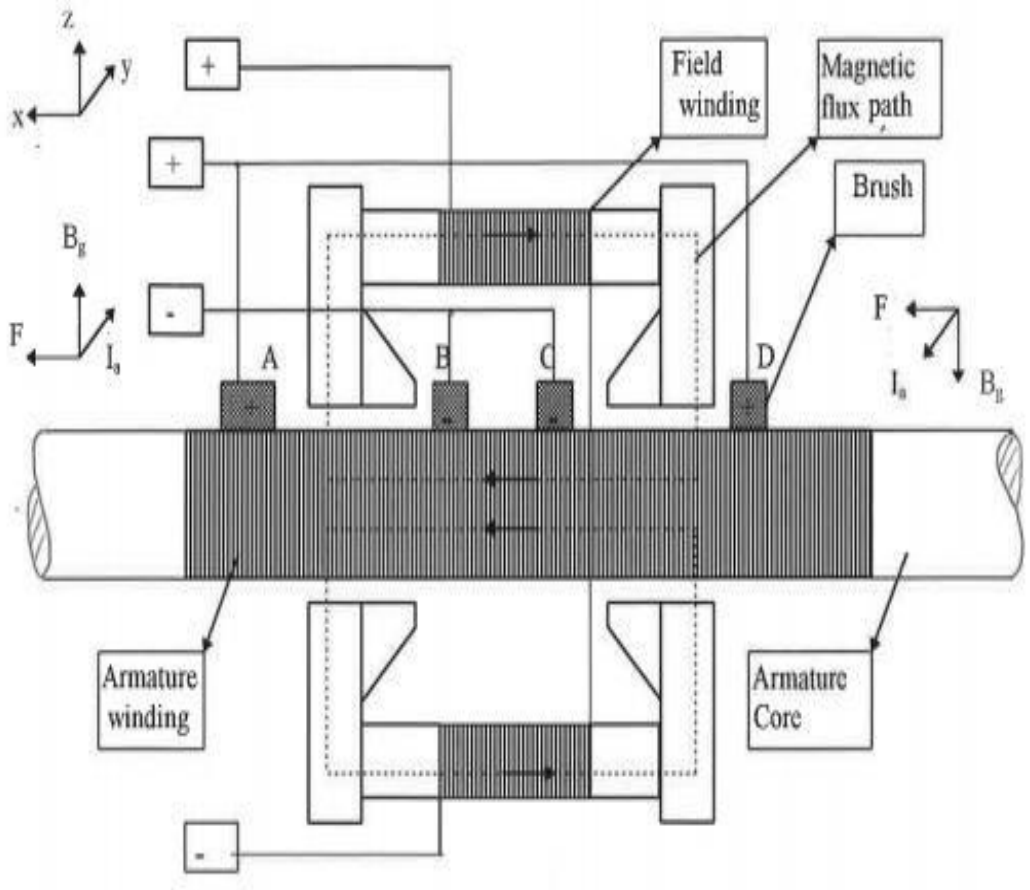

Figure 2.14 Cut section of wound field two pole linear motor was design by Ratcliff and Griffiths [52] .

This was followed in 1969 by another design, by Jones, based on Ratcliffe and Griffiths' brushed DC linear motor. This later design featured a differently shaped pole and had only 3 brushes. Figure 2.15 illustrates this, with the broken lines indicating the path of the magnetic flux. Also in 1969, 2 further DC linear motor types were designed by Griffiths and Jones [53], and these were the wound field 4 pole DC linear motor, illustrated in Figure 2.14, and the 2-pole, demonstrated in Figure 2.15, with the broken line representing the path of magnetic flux. Each motor features movement in the field unit, with static armature windings. Brushes affixed to the carriage provide voltage to

the armature, requiring unipolar to be supplies via the carriage to both field coils and the armature-supplying brushes. An analogous motor featuring cylindrical field windings was designed two years later by Warnett [54]

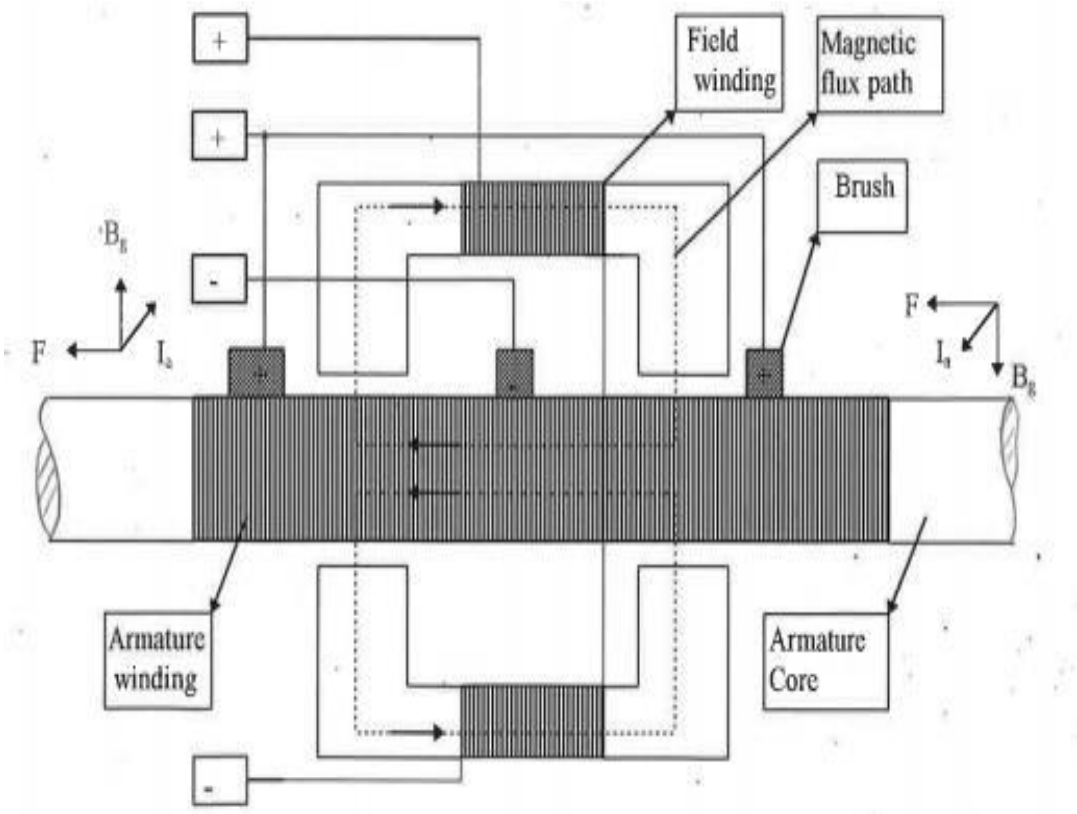

Figure 2.15 Jones' wound field two pole linear motor in cross-section [44].

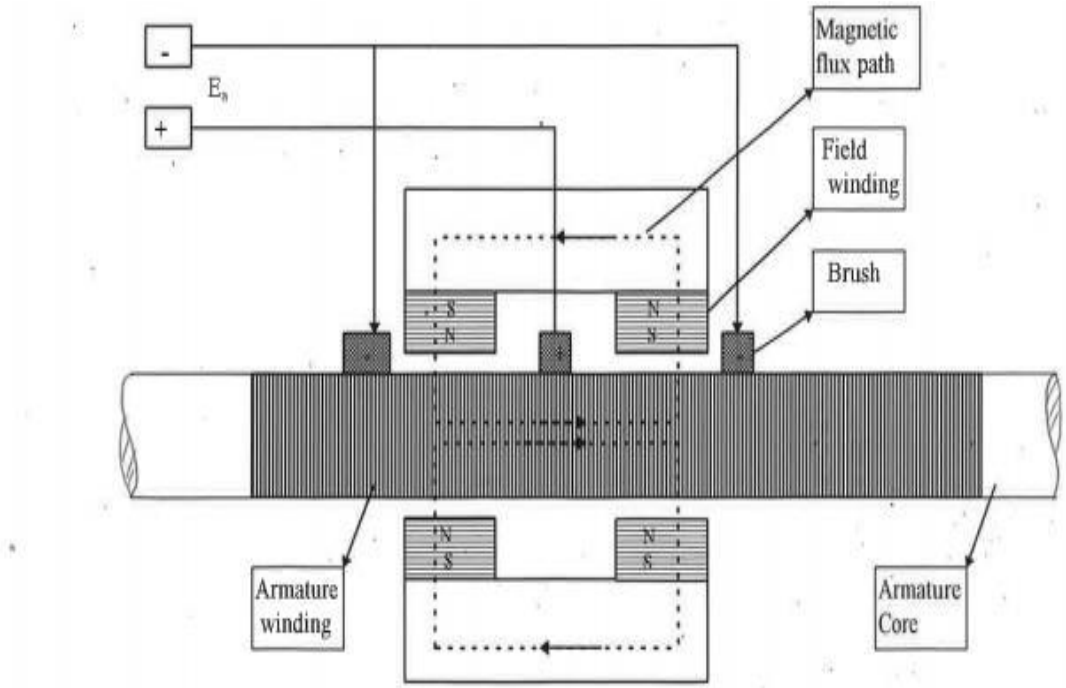

Figure 2.16 Griffiths and Jones' wound field two pole linear motor in cross-section [45].

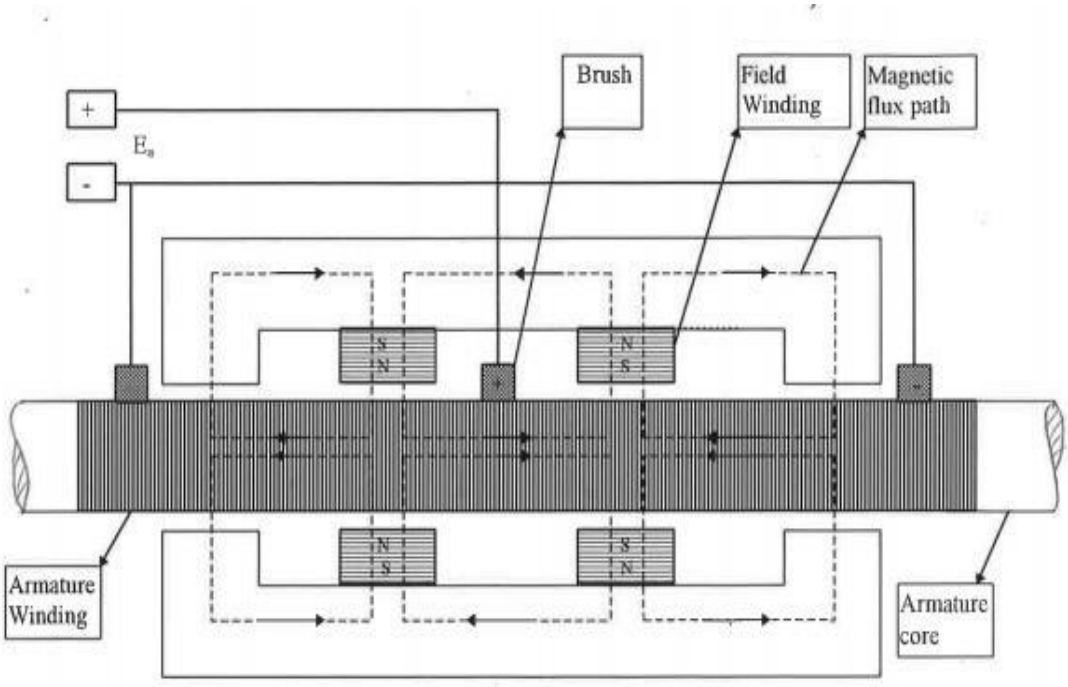

Figure 2.17 Griffiths and Jones' wound field 4 pole linear motor in cross section [45].

A different model for a DC linear motor was developed in 1969 by Green and Paul for static and stroke applications [55]. A simple 2-pole linear actuator is given in Figure

2.16, in which free movement in a linear direction over a short range is allowed for the armature, with fixed field units. The armature is constructed with a circular mild steel core with one layer of winding, reversing winding directions in the idle. Encapsulation of the windings means that no brushes are needed. While a commutator is not needed for the linear motors shown, field winding was needed in order to generate airgap flux. Figure 2.19 illustrates flux patterns in a 2-pole linear DC actuator, with the airgap flux's radial element cutting the current for the armature, generating unidirectional force at both poles. A support for the armature is given at both ends, with travel distance being limited.

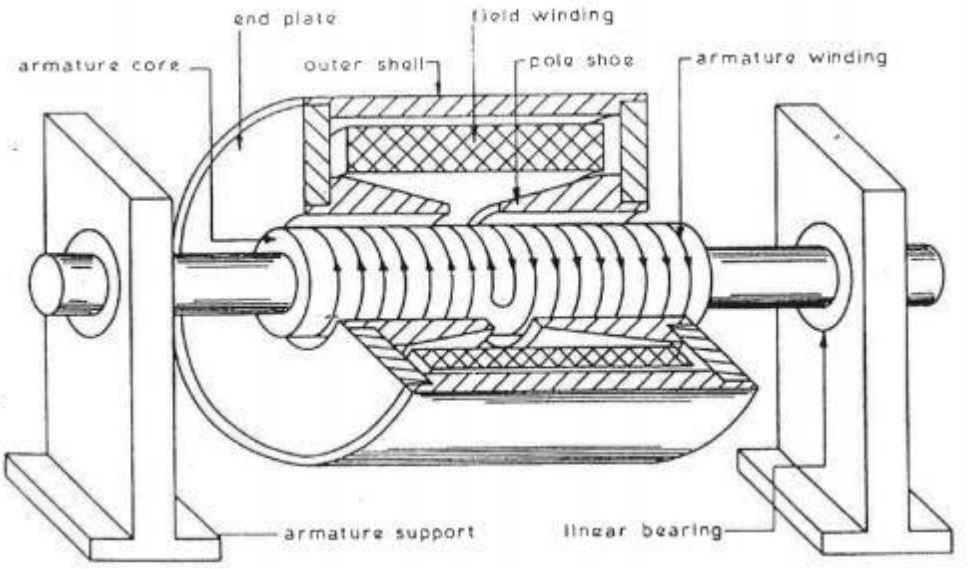

Figure 2.18 Two poles linear motor [55].

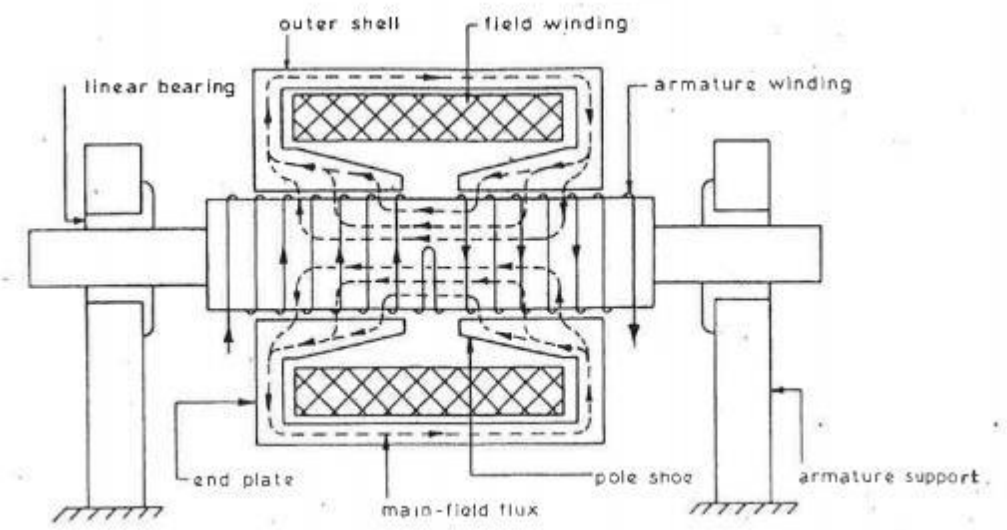

Figure 2.19 Flux pattern of two poles linear motor [55].

2.8.2. PM linear DC motors

In 1975, Basak designed and tested a DC LM which had a ferrite PM as its field source [56] in Figure 2.18. This motor has similarities with Griffiths and Jones' LM but substitutes a permanent magnet for field windings for the generation of a magnetic field to generate linear movement through its armature current interactions. It also has auxiliary poles in Figure 2.20 [57]. Field flux generation relies on ferrite PMs, thus improving performance due to the motor only requiring a single source of power: however, this model retains the issues associated with brush use. In Figure 2.20, Basak's ferrite field DC LM is illustrated, with dotted lines indicating the path of magnetic flux. The PM DC LM by Dascalescu demonstrates how the ferrite field DC LM continued to be improved, being based on Basak's design but with an overshot applied [58] [59] to allow positional management of corona electrodes within electrostatic separates. In this design, the DCLM comprises a field system which moves and a static armature. Silicon-iron laminate yokes alongside PM blocks make up the field system. A bar of mild steel forms the core of the armature, with the one-layer windings made from enamelled copper in Figure 2.21. The control circuit determines positional accuracy in this design.

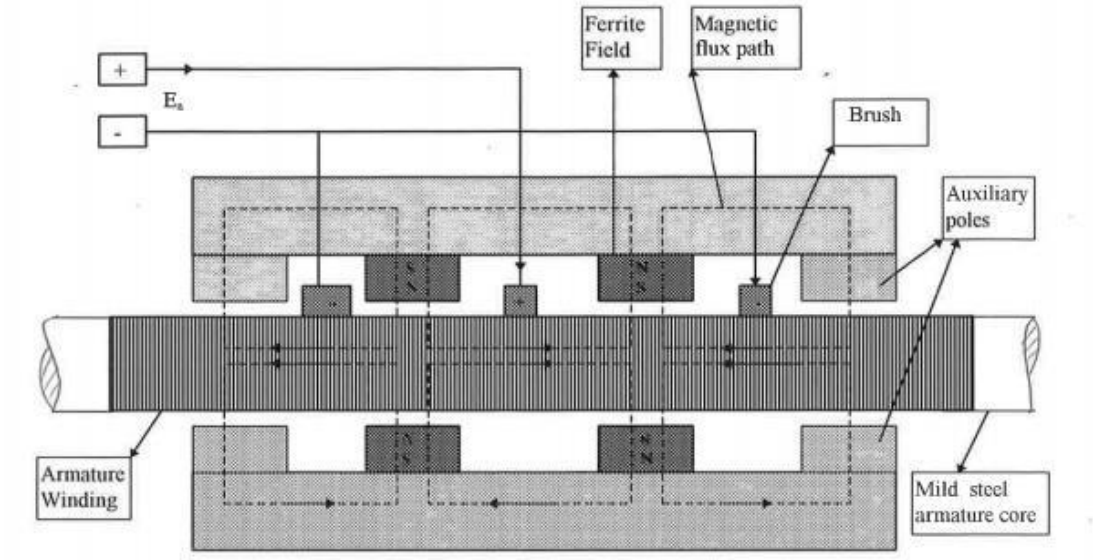

Figure 2.20 Cut section a ferrite field with four poles linear DC motor [56].

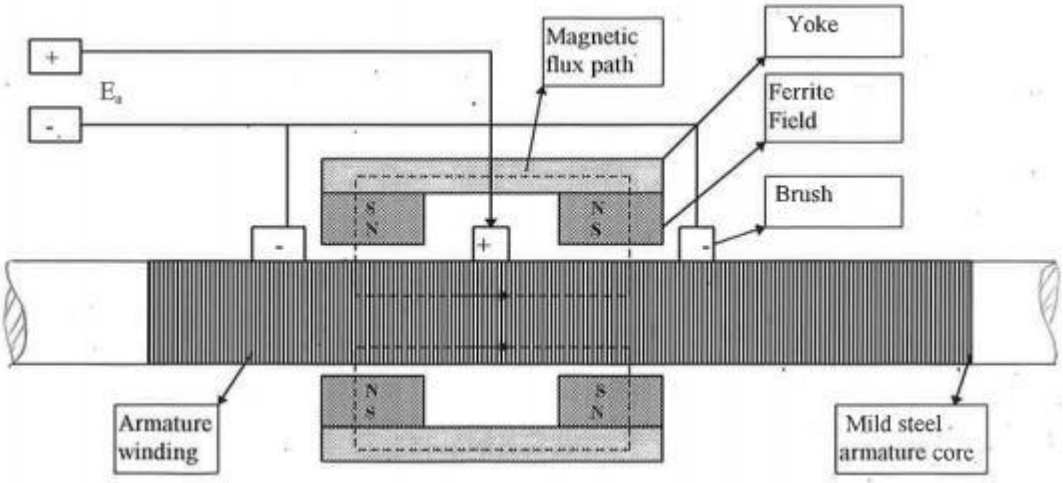

Figure 2.21 Cut section of a ferrite field with two poles linear DC motor [56].

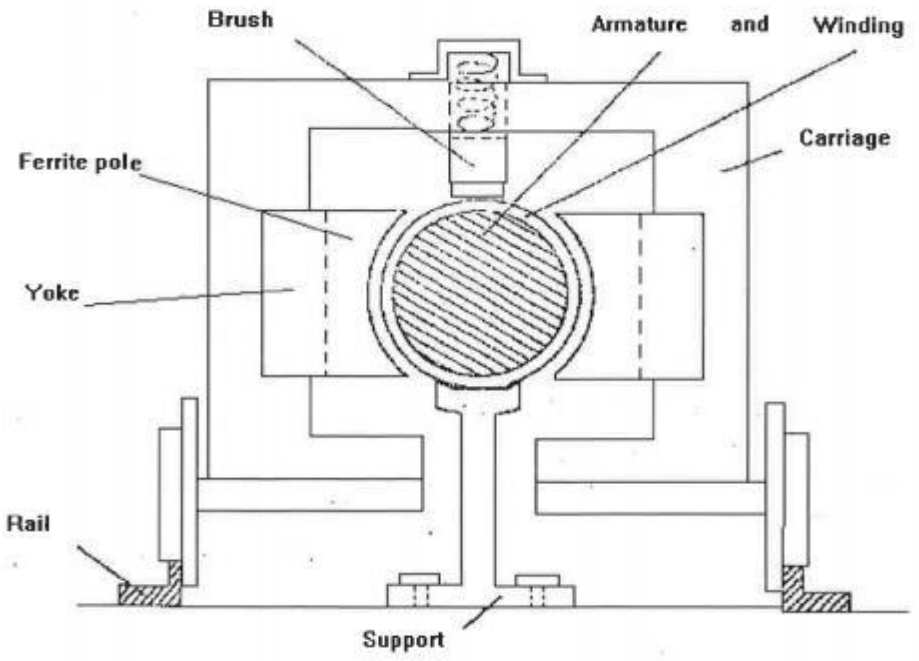

Figure 2.22 The elevation of ferrite field linear DC motor [56].

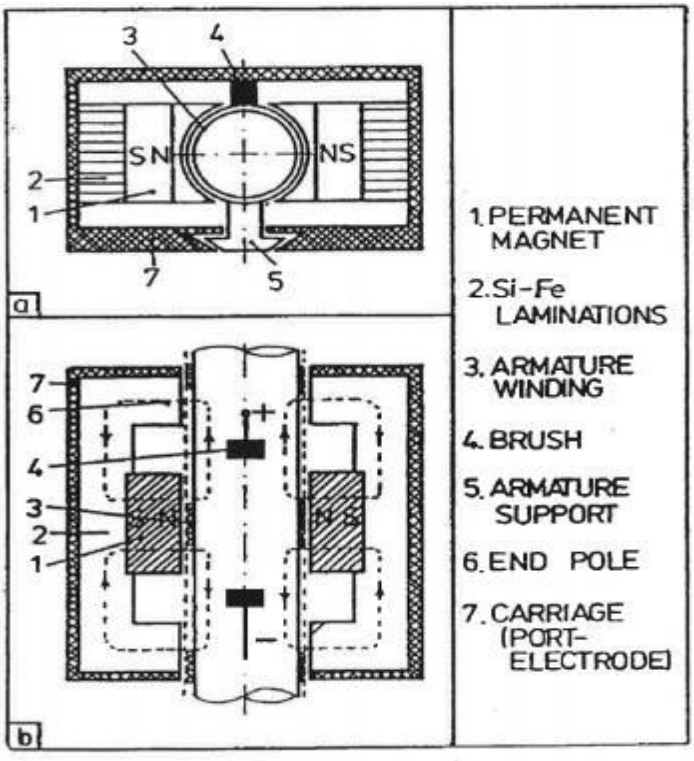

Figure 2.23 Linear dc motor designed by Basak and used by Dascalescu for electro-stators [60].

In the mid-1980s, a more effective rare-earth PM was developed, with a neodymium-

iron-born (NdFeB) PM forming a field unit which could be used in linear and rotary motors. Akmes studies 2 types of flat PMLM to be used in long-stoke functions [61]. in the first design, Neodymium-iron-born (NdFeB) permanent magnet was used as the field unit while the second design made use of a ferrite magnet as the field unit. Through a comparison of FEM and experiment findings for each design, the NdFeB-based design was found to be more efficient.

In 1995, Anayi designed and built a brushless DCLM using an NdFeB PM and a square cross-section core for the armature [62]. The design's cross-section is illustrated in Figure 2.24. Four permanent PMs are mounted on a motor slider with a guide made up of 2 fixed bars and a linear bearing. Windings around the core of the armature were made up of 64 sections, energised sequentially by a switching circuit controlled by a microprocessor. Measurements were taken for various factors as functions of the positioning of the linear motor slider, including LM flux density, axial flux and static thrust. Airgap uniformity is ensured by the PM's rectangle form, with measurement of flux distribution across the whole motor cross section performed via FEM.

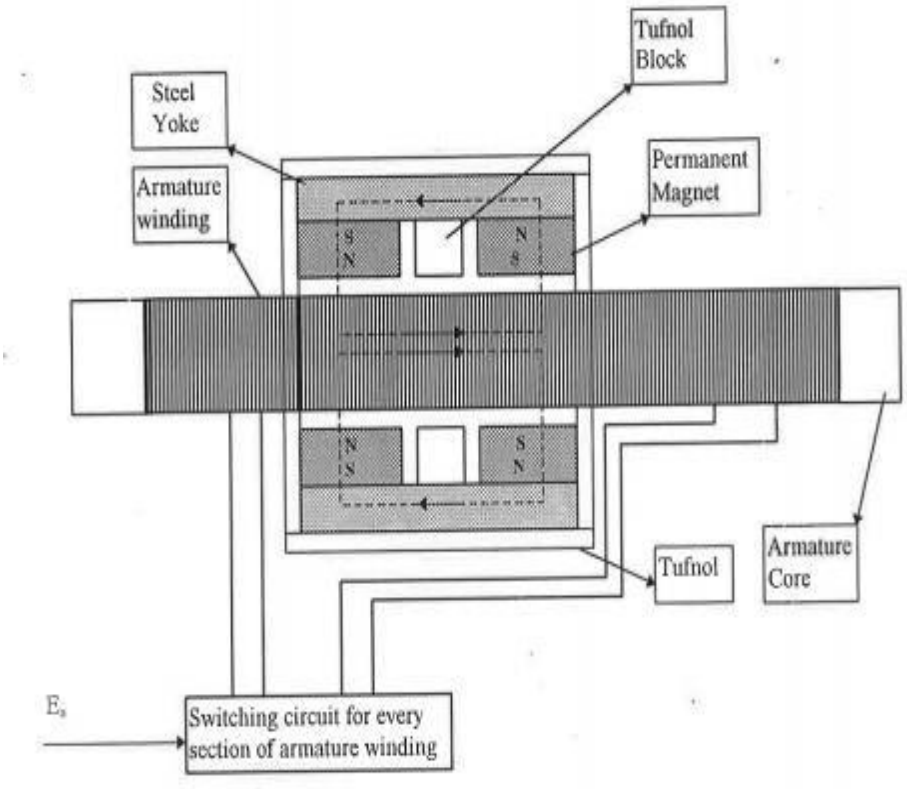

Figure 2.24 Cut section of a brushless permanent magnet linear DC motor designed by Anayi [63].

Two further designs for brushless DC LMs were created in 1996 by Filho [64], each using 2 armature cores in parallel, and with one design featuring a single armature winding which was continuous in Figure 2.25, and the second having armature windings in multiple sections in Figure 2.26, capable of stepper motor use. Each design contains 7 NdFeB PM blocks forming the source of the magnetic field, and 2 mild steel section bars which were long and square forming the fixed core of the armature. The second design allows individual or simultaneous energising of the separate winding sections, and this must be synchronised with the moving unit's positioning.

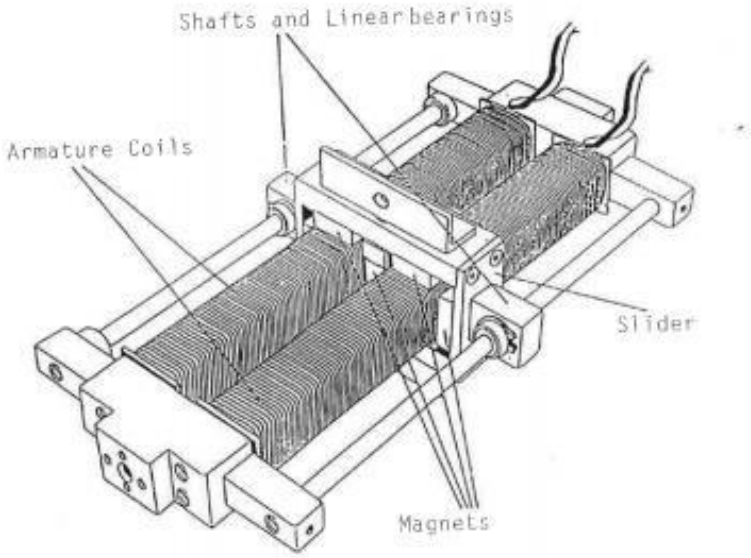

Figure 2.25 Do

uble armature brushless DC linear motor with continuous winding [65].

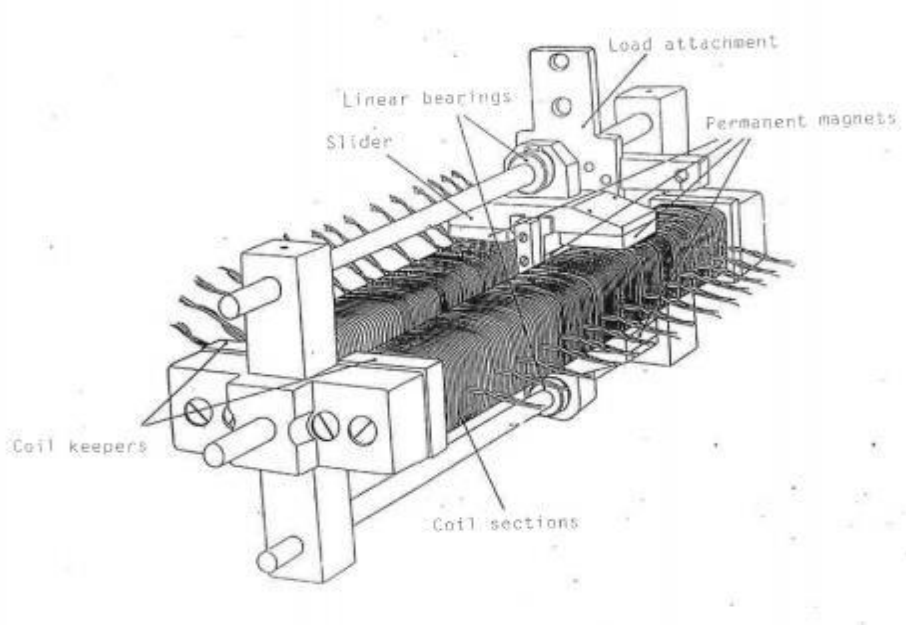

Figure 2.26 Double armature brushless DC linear motor with multi-section of armature winding [66].

Basak designed a linear DC stepping motor based on sectioned 3-layer windings on the armature, with a moving field unit which contained an NdFeB rare-earth PM and a mild steel long stator. A comparison was made between this design and a second motor which was set up in a similar way but had only one layer of winding on the armature [67]. Basak reports that thrust can be increased by using multiple layers of windings on the armature. The findings from experiment reveal a small impact on the useful flux from airgap variation based on use of one layer or 3 layers. However, the 3-layered windings LM gave approximately triple the flux of the one-layer motor at a particular useful flux and current [67].

There has been an increasing focus in research on applying MATLAB and FEM in designing and optimising DC LMs. Basak applied a dynamic and 3D electromagnetic FEM method for analysis of dynamic properties for a DC LM with a square armature as applied in material handling systems. This included analysing findings on speed as a function of time through applying different currents, as well as analysis of power and force outputs as functions of speed [68].

Honds and Meyer's 1982 [69] work involved a novel PM DC linear motor for recorders. The design applied 2 PMs to generate the airgaps magnetic field, affixed to the carriage, with the static part of the assembly containing 3 cores of soft iron in parallel, with the

central core having the windings for the armature. The designed motor gave a peak force at 0.6 Amp of 2 N.

2.9. Sliding Mode Control

Sliding Mode Control (SMC) offers a straightforward and systematic approach to achieving robust control, characterized by high-speed discontinuous switching operations. This control methodology allows tailoring the dynamic behaviour of the system through the choice of a specific switching function, providing excellent performance with insensitivity to parameter variations and disturbance rejection. The simplicity and systematic procedures for designing SMC systems make it an attractive choice in control system design [137]

Despite its theoretical robustness in the face of parametric uncertainty, classical SMC is hindered by chattering a phenomenon involving finite-frequency, finite-amplitude oscillations seen in many sliding mode implementations. Chattering results in drawbacks such as low control accuracy, increased heat loss in electrical circuits, and heightened wear of mechanical components. Additionally, it may induce unmodeled high-frequency dynamics, degrading overall system performance [138]. The practical implementation of SMC is limited due to these challenges.

To address the issue of chattering, various smoothing techniques for sliding control have been proposed. One such technique is the continuous approximation of the switching control law, known as boundary layer control. This method employs a continuous high-gain control law within the boundary, with saturation applied outside the boundary. However, reducing the acceptable gain to avoid instability in the boundary layer can significantly impact system performance, falling short of the ideals achieved by pure sliding mode control [139].

From a different perspective, the reaching law method offers a solution to chattering by directly tuning reaching mode characteristics. This approach acknowledges that chattering is often caused by nonideal reaching at the end of the reaching phase. An additional advantage of the reaching law method is its ease in obtaining the SMC control law [140]. Despite these efforts to mitigate chattering, it is important to recognize the potential trade-offs introduced in terms of overall system performance.

2.10. The Bees Algorithm

One of the latest algorithms influenced by bee behaviour is the Bees Algorithm (BA). Proposed by Pham [123], BA is a population-based metaheuristic algorithm rooted in the swarm intelligence of bees during food foraging. Essentially, the algorithm combines a form of exploitative local or neighborhood search with an exploratory global search. Both search modes involve a uniform random search. During the global search, scout bees are randomly distributed across different areas of the search space to explore potential solutions. In the local or neighborhood search, follower bees are enlisted for patches identified by scout bees as more promising, allowing for the exploitation of these patches.

In recent times, there has been significant attention directed towards the Bees Algorithm (BA) as a valuable tool for optimizing controller parameters to achieve optimal performance. A notable application, as documented in [141], involved employing the BA to optimize PID controller parameters for a two-floor structure subjected to earthquake excitation. Notably, the PID-based BA demonstrated superior performance compared to the same controller tuned using the Genetic Algorithm (GA).

In another instance documented in [142], the BA was applied to optimize PID controller parameters for one leg of a quadruped robot. Additionally, a study conducted in [143] highlighted the BA's proficiency in solving intricate parameter optimization challenges in robot manipulator control. This study presented two applications: the first involved modelling the inverse kinematics of an articulated robot arm using neural networks, while the second focused on designing a hierarchical Proportional–Integral–Derivative (PID) controller for a flexible single-link robot manipulator.

Furthermore, the application of the BA in designing a PID controller for a single-input multi-output (SIMO) inverted pendulum system was explored in [144]. This diversity of applications underscores the versatility and efficacy of the Bees Algorithm in addressing complex optimization problems across various domains.

2.11. State of the art of the force ripple reduce technique.

The thrust ripple can be minimised by suppression techniques for linear motors, and

these methods are summarised in the following categories. Structural optimisation is a method used to minimise cogging and end effect force in slotted linear motors. This control method is one of a number that have been used to decrease the thrust ripple, where different types of control methods and algorithms are used to reduce the speed fluctuation caused by the force ripple. The latest methods include combination control methods and structural optimisation [70].

2.11.1. Structure optimisation

Huang et al., in [71], presented a simple structural design which changes the length of mover to reduce the end force, and in which the magnetic fields at each end of the armature are abnormal. This makes the inductance of the winding in the middle different from that at the ends. This then leads to unequal magnetic flux in the winding. Force 1 and force 2 describe the thrust at each end of the mover, wherein each force has a different direction, and the end force is the sum of these. By adjusting the length of mover, the forces at the end are reduced and this improves the performance of the DC linear motor, as shown in Figure 2.27 and 2.28.

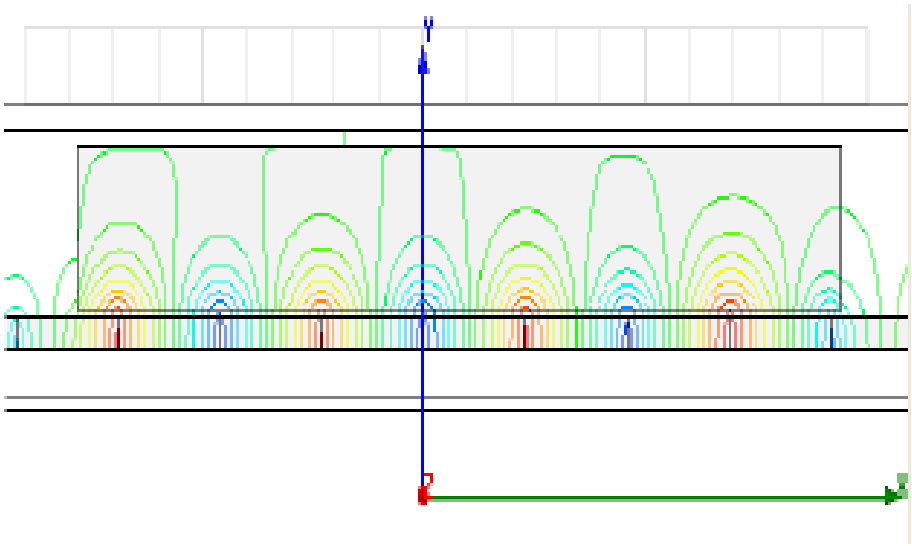

Figure.27 Magnetic distribution of LBDCM L=7.5τ [72].

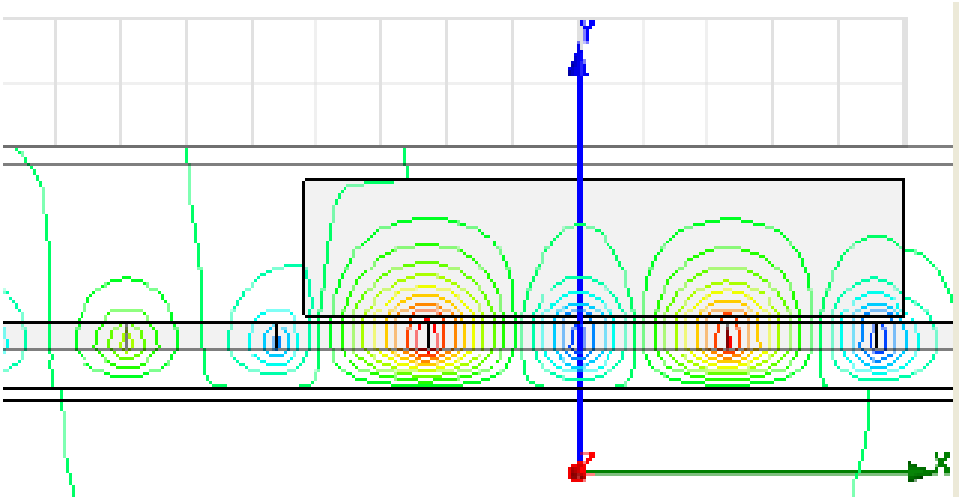

Figure 2.28 Magnetic distribution of LBDCM L=4τ [72] .

Wang et al., in [72] , proposed a structured design for a permanent magnet shape to minimise the detent force of a permanent magnet linear brushless DC motor. The finite element method was used for analysis, such as shifting magnetic poles and varying the magnet width to minimise the detent force. The magnetic flux flows from the edge of the permanent magnet to the slots, resulting in production of the detent force. This flux generates a horizontal component of attractive force to the incoming side of the tooth. Similarly, the magnetic flux from the rear edge of the permanent magnet also produces a horizontal force. As the width of the magnet decreases, the leading and trailing parts of the permanent magnet become closer to each other. This causes a change in the horizontal components of the force of attraction developed on the side of the permanent magnet. The resulting retention force may increase or decrease depending on the relationship between the pitch of the magnet and the pitch of the slot.

The detent force of each magnet is in phase and therefore these are added together to produce the full cogging effect. To prevent this additive effect, magnets can be displaced relative to each other to keep the detent force of each magnet out of phase with the other. It is assumed that the detent force arises from the difference in the position of the permanent magnet end and the position of the tooth. If one detent force is independent of the other, the total detent force can be decreased by arranging a permanent magnet end and a tooth.

Baatar et al., in [73], designed a permanent magnet linear synchronous motor with 9 poles and 10 slots to minimise the cogging force and then optimised its shape to minimise the detent force, as shown in Figure 2.29.

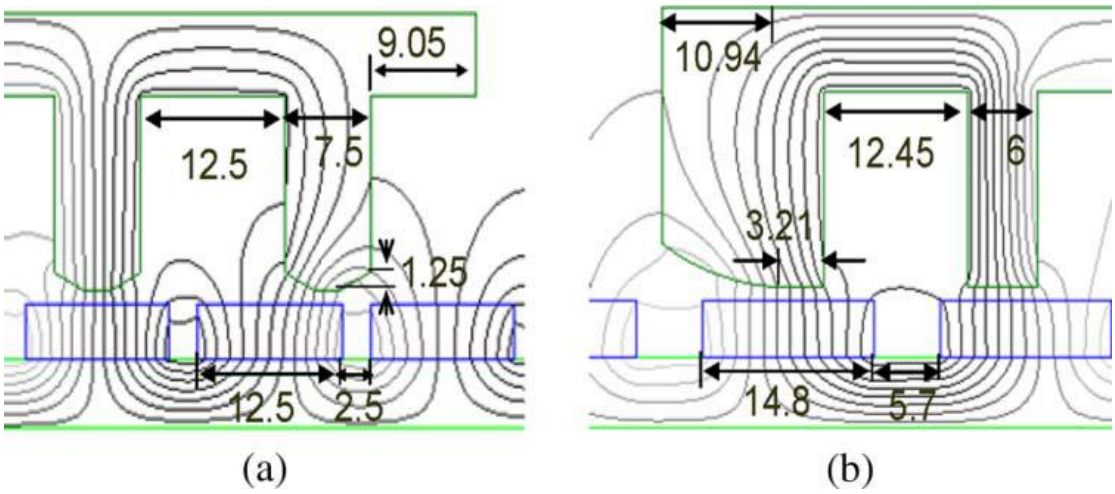

Figure 2.29 Comparison of the optimized shapes. (a) Conventional structure. (b) Proposed structure [73].

The cogging force is generated individually by each winding slot of the armature core and the total cogging force is the summation of these. Baatar used a structure termed 9p10s in order to lead the individual cogging forces from armature slots to cancel each other out. The results show that the cogging force and detent force were reduced, and also that the thrust force was increased by around 7% under the same operation conditions.

Optimizing axial length to reduce the cogging force is the approach used by Zhu et al. [74] in a slot-less permanent magnet linear motor. The cogging force arises due to two potential causes, resulting from the finite length of the armature core and the slotting. Since a slot-less linear motor was used, this technique was applied to the end cogging force, which is the main source of force cogging. This technique is based on analysis of the end force waveform, aiming for this to become completely the opposite of the other end's force, wherein the result is the two forces cancelling each other out, as shown in Figure 2.30.

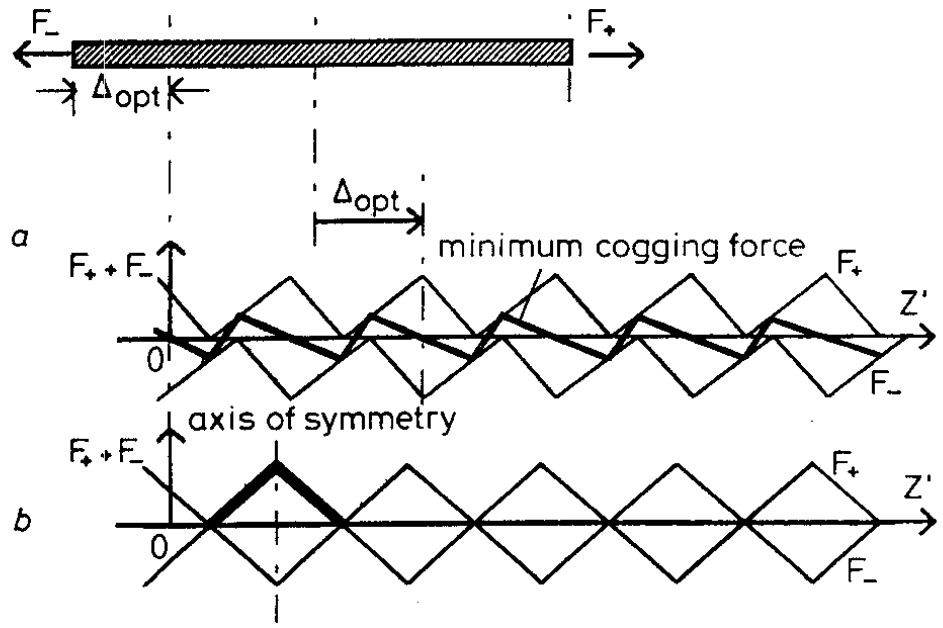

Figure 2.30 a) The cogging force with the original length b) Results of cogging force after optimal length [75].

Luo et al., in[75] , developed a method to minimise the detent force through optimizing magnet width through combining the finite element method and Fourier transform to obtain the power spectra of the elements that constitute the detent force. These components are caused by edge effect and slotted effect, which can be decomposed into three components: right edge (force resulting from the right edge) of the mover; the left edge (force resulting from left edge); and the force that results from interaction of both edges of the magnets. The results show that the thrust ripple of the DC linear motor can be effectively reduced by adjustment of the magnet width, as shown in Figure 2.31.

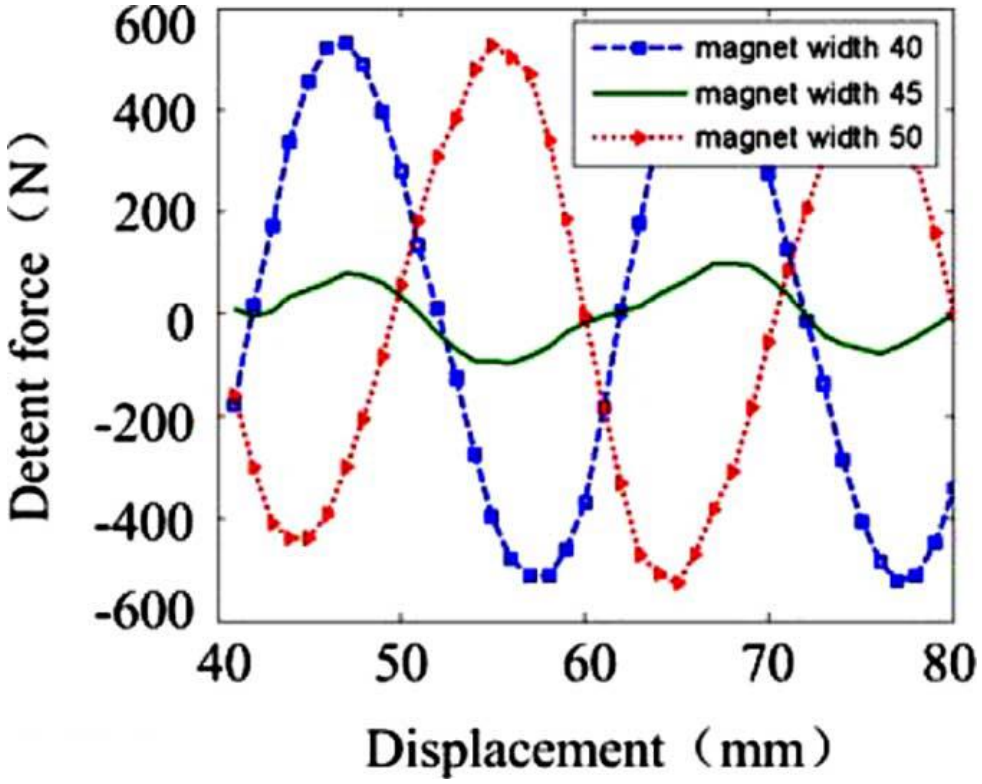

Figure 2.31 Detent force comparison of three different magnet width [76].

Using current compensation and the optimal structure design technique, the detent force was reduced by Zhu et al. in [76] . The authors analysed the detent force, which can be divided into two components. The first component is slot effect and the other is the end effect. Zhu et al. avoided the complex structure by only using the semi-closed technique to minimize the slot effect, as shown in Figure 2.32.

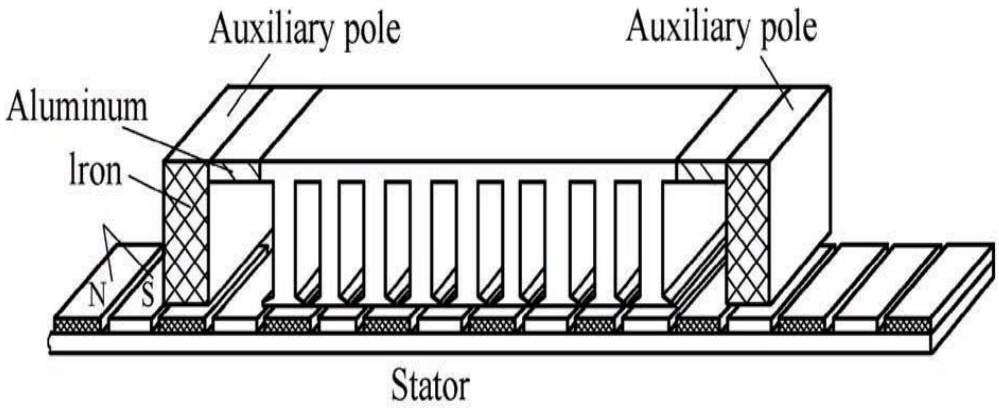

Figure 2.32 Auxiliary pole fixed on the end of mover [77].

This method also has an effect on the end force due to changing the length of the mover, becoming close to the permanent magnet, but this was not the only technique used for suppressing the end effect: The authors provided a novel technique used for end effect; auxiliary poles. The auxiliary poles are fixed to both sides of the iron core, with aluminium used in between the auxiliary poles and iron core to block the effect on flux distribution from exciting the current in the winding. Also, the current compensator was realized a higher performance by using a field-oriented method with a feed-forward current. The result shows that the best way to reduce the force ripple is a combination between the structure optimization technique and the control method.

Zhen et al., in [77], have presented a new model to suppress the force ripple. This model uses the d-q reference frame, where the force ripple is calculated at discrete positions. The authors used the developed model, measured flux density data, and winding distortion to calculate the force ripple, and data for flux density was also used. This model was applied for an iron-less permanent magnet synchronous motor with double sides in one magnetic track setup, to measure the force ripple and magnetic flux density distribution. The results show that this model is effective in minimizing the force ripple, and it can also be used to obtain a smooth thrust or torque for motor optimization design.

Because the cogging force is dependent on the position of the permanent magnet when interaction occurs between armature teeth and permanent magnet without input from an exciting current in the winding, Bianchi et al., [78], used shifting poles to reduce cogging force by adjusting the distance between them. The idea behind this method was about pushing components of the cogging force out of phase by shifting the poles as shown in Figure 2.33

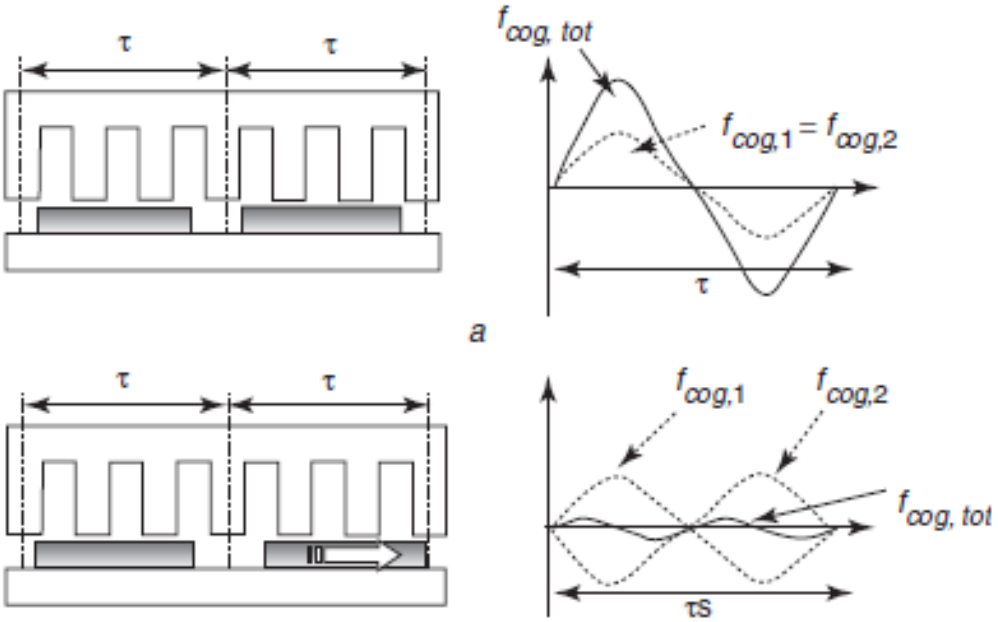

Figure 2.33 The results before and after shifting the permanent magnet [78].

As a result, the total cogging force is reduced, which means that the two main components of the cogging force are out of phase and cancel each other out. This technique has been applied for a permanent magnet linear tubular motor using six poles and eight slots and adjusting the distance between them.

The permanent magnet is the main source of air-gap magnetic field for PM linear motors. When a permanent magnet is used as a mover for the linear motor, its form and size could affect the detent force component [79]. Lim et al. [76] worked on adjustment of the width of the PM versus constant slot pitch to decrease the detent force. Analysing components of detent was performed using finite element analysis, and a moving model node technique was used to overcome the problems of excessive computation time and demand for resources which arise when using the FEA. The results show that the moving model node technique has a substantial effect to some extent on the detent force and reduces it satisfactorily.

Structural optimization is a technique used for suppression of the force ripple. Many approaches have been used to reduce this force such as pole shifting, adjusting the size and shape of PMs, semi-closed slots, adjusting stator length and end structure

optimisation, optimization not eliminate the force [76]. In addition, most of these methods are complex, and the desired force is also reduced [72]. Other techniques are expensive and complex to manufacture, such as adjusting PM width, appropriate PM shape and skewed PM,, as these also increase the structure's complexity. However, different types of control methods have been used to decrease the thrust ripple of linear motors because of their convenient and flexible features.

2.11.2. Control suppression methods

The force ripple arises because of the attraction between the iron core and the permanent magnet in the direction of motion. This force is always present, even if the current is not flowing through the coils. Also, it depends on the position of the permanent magnet and core. The self-inductance of the winding will change when the position of the mover is changed, while when the current flows through the coils, this generates a force that is dependent on the position in the direction of motion of the translator. The result of combining of forces is called force ripple. Imen and Shak in [80] have designed a learning controller to minimize these forces (force ripple). This control method has two main parts: one is feedback and the other is an adaptive feedforward controller. The authors designed a feedback control based on a PID, using second-order control function, and to suppress the force ripple, an adaptive feedforward controller was designed based on a neural network which is used for the prediction of unknown relations and un-modelled forces.

An adaptive dither was used for force ripple suppression by Tan and Zhao in [49], for an iron-core permanent magnet motor. The control method was designed with three components, which are PID feedback, simple feed-forward, and an adaptive feed-forward (AFC). The first two components are used for linear control of the motor, where the PID structure was used by feed-back control and the adaptive feed-forward produces a dither signal based on a signal model. This signal is responsible for suppressing the force ripple. This method has been applied with an iron-core permanent magnet linear motor to make a smooth movement without compromising the main thrust force while minimizing the force ripple.

A design for achieving high position accuracy for linear motors and reducing the effect of parametric uncertainties that happen due to cogging, friction and force ripple was developed by Yao and Xu in [81]. Discontinuous projection is a method that has been constructed by using an adaptive robust motion controller for a high-performance linear motor. Yao and Xu designed a model consisting of a known basis function to estimate force ripples that are not known: "on-line parameter adaptation is then utilized to reduce the effect of various parametric uncertainties such as unknown weights, inertia, and motor parameters while certain robust control laws are used to handle the uncompensated uncertain nonlinearities effectively for high performance".

Because the thrust ripple is a periodic function of position, an iterative tuning method is utilised by Wu et al. in [82] to reduce thrust ripple. They use a position-dependent multi-order harmonic model as the feed-forward controller. This controller uses past cycle results to tune the parameters of the controller. Thus, the performance of the motor is improved by tracking it cycle by cycle with robustness to external disruptions. By applying this method, errors were reduced by 60% at least.

The thrust ripple can be defined as a periodic function of position, and the fast Fourier transform has been used to analyse the components of the force ripple. Then the recursive least square parameters (RLS) have been applied without the velocity variable to avoid noise when calculating the parameters of the thrust ripple. Finally, the feed-forward component is used for injecting certain values into the system to compensate for the force ripple [83] [79]. These steps were applied to permanent magnet linear motors by Zhao and Tan in [83] [84]. They designed a control system based on recursive least squares (RLS). The control algorithm used consists of a PID feed-back component and two adaptive feed-forward components: one for compensation of the force ripple; and another which works as the inverse model of the controlling permanent magnet linear motor.

Cho et al., in [85], present a novel disturbance reparation to suppress periodic disturbance, including force ripple. This method works on the output of the disturbance through the zero-time period as the first observed results. After this, a combination is made between this and adaptive control. These steps are to get the results updates continually for each next period.

Repetitive control was used also to supress the force ripple of the linear motor by Chen and Hsieh in [86]. They designed the system in a discrete time domain to track errors and then reduce them using a repetitive controller, and also increase the efficiency of performance of the linear motor. The principle of this controller depends on generating a reference signal and injecting this into the closed loop system, in which the output follows or tracks this signal. Based on this, the output signal either follows the reference signal or rejects the periodic disturbance, including the force ripple. The period error is decreased after the initial period, and the control system works on improving accuracy, enhancing performance, and increasing stability.

Lee et al., in [87], designed a new control structure based on basic PID, which consists of a feed-back control and a feed-forward control. The feedforward was designed using an iterative learning control (ILC) algorithm. An intelligent feed-forward control was utilised to enhance the trajectory tracking performance of a linear motor based on results arising from repeated implementation of the same operational process, while the feedback was utilised to stabilise the permanent magnet linear motor system. This control method has been used by Qian et al. in [88] to minimise the torque ripple of the permanent magnet synchronous motors. The iterative learning control was analysed in both time domain and frequency domain. For the time domain, a forgetting factor is launched to enhance the robustness of the iterative learning control against disturbance. However, this has limited the impact of suppression of disturbance, and thus the ILC has been modified and implemented in the frequency domain, and then used to suppress the thrust ripple.

Many approaches have been proposed to suppress the force ripple of the linear motor, most of them focused on structure optimisation. Others have focused on control methods separately. However, the results of these methods show that they cannot suppress force ripple completely. Therefore, the best approach that can be used is a combination of control methods and structure optimisation. A combination of control method and structure design is presented by Wang and Li in [89]. A permanent magnet was designed with optimal skewed length to reduce high order harmonic components, and the low harmonic was reduced by linearization observation without dependence on a speed controller. For the control method, a feedforward control is utilised after injecting an

estimate force ripple into the control system.

To enhance the performance of linear motors and reduce force ripple, this thesis aims to achieve smoother operation and reduced ripples by focusing on combined improvements in magnetic design, control systems, mechanical components, and manufacturing processes.

2.12. Summary

A comprehensive review has been conducted comparing various classifications and topologies of linear actuators. The discussion also includes the classification of magnetic materials used in linear motors, and a comparison of different types of permanent magnets to determine the most suitable for a particular motor. The benefits of using linear motors instead of rotary to linear systems shut as CNC machines, conveyor systems, crane systems and magnetic levitation are highlighted. The analysis of a magnetic circuit in a permanent magnet actuator is demonstrated through the use of an "Equivalent Magnetic Circuit," and the determination of air-gap flux density is discussed. Additionally, the forces associated with linear motors and the nonlinear effects that can impact motor performance are examined. Lastly, a review of previous work related to the design of linear motors and reduce force ripple are presented.

Chapter 3: Mathematical Modelling and Structure of DC Linear Motor

3.1. Introduction

A knowledge of system properties is commonly assumed in the construction of controllers. A controller design cycle typically starts with the modelling phase which will be considered in this chapter. A model permits simulation and study of a system's dynamics without implementing the system, which forms the basis for the design of a control system. After calculating Mathematical model of DC linear motor, a dynamic friction model will be employed to elucidate static friction phenomena and the dynamic friction phenomena, particularly relevant in the context of high-precision applications. This investigation will centre on the nuanced examination of frictional responses to step inputs. Also, to acquire a comprehensive understanding of the machine characteristics and a more precise brushless DC linear motor design, a finite element method (FEM) analysis is initially performed according to the preliminary geometry. A comparison will be carried out between the simulated and model designs, in term of the static thrust, air-gap flux density and magnetic flux distribution. The approach adopted for modelling both the magnetic materials and the permanent magnets is explained in detail. This chapter also describes the pre-processing operations involved, including the mesh construction, specified boundary conditions and the excitation sources used.

3.2. Dynamic and model DC linear motor

Mathematical model of DC linear motor can be found by apply some fundamental laws such as Newton's law for mechanical and linear movement model and apply Kirchhoff's and Ohm's laws for electrical model.

For a translator part, Newton's law state is:

$$Ma = \sum_{i=1}^{n} F_i \tag{3.1}$$

Where M =mass

a =acceleration

F_i =force

There are two general units in linear motors, which are stationary and free to move. The result of the force that produced by DC linear motor is the movement of the moving unit as a linear motion.

The linear motor can be proposed as shown in schematic below.

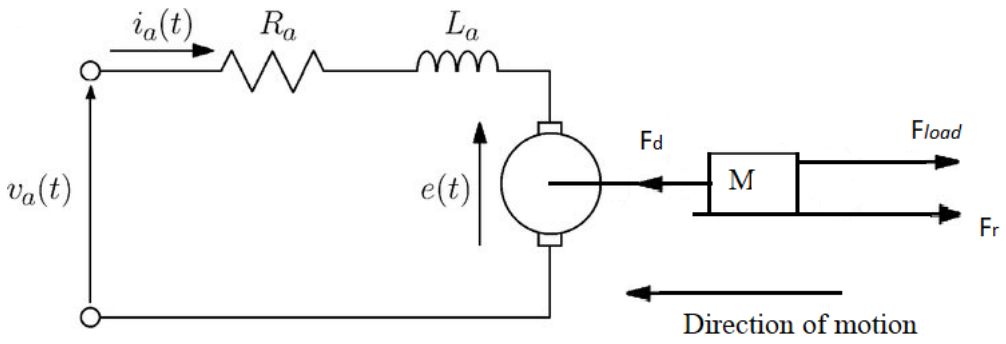

Figure 3.1 Equivalent circuit of a DC linear motor

Where M is the total mass of the translator of the DC linear motor. F_d is the developed force performing on the moving unit. whereas F_{load} and F_r are forces moving in contradiction to the motion.

With using Newton second law to apply it on the linear motor whose equivalent circuit in Figure 3.1 it can get the equation for movement of the mover unit as below

$$M\frac{dv(t)}{dt} = F_d(t) - F_c - F_s - F_{load} \tag{3.2}$$

F_d is the developed force performing on the moving unit.

F_c is the Coulomb friction force.

F_s is the static friction force at zero velocity.

F_{load} is disturbance force or load force.

M is the total mass of the translator of the DC linear motor.

F is the viscous friction coefficient.

$v(t)$ is the linear velocity of mover.

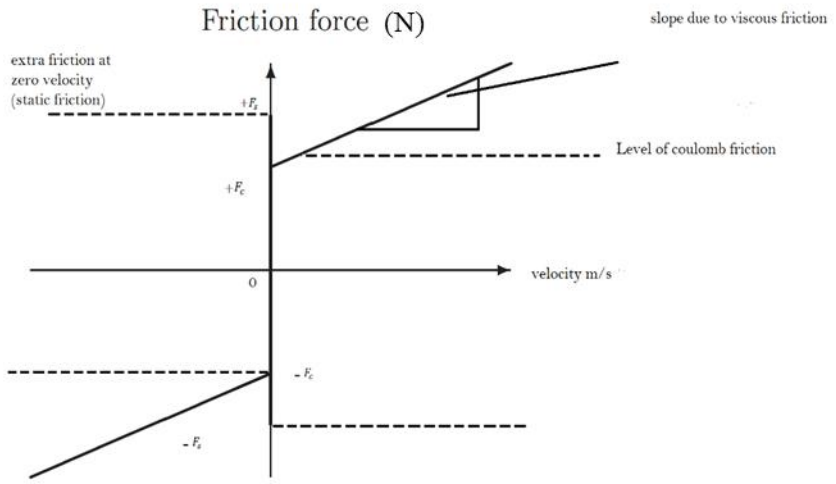

Figure 3.2 Simplified friction force in motion control system [90].

a simplified model, friction is often considered a constant force that opposes the motion of an object. While real-world friction can be complex and affected by various factors like surface roughness, lubrication, and temperature, a simplified friction model helps in analysing and designing control systems by considering a constant, predictable force that resists the motion of objects being controlled.

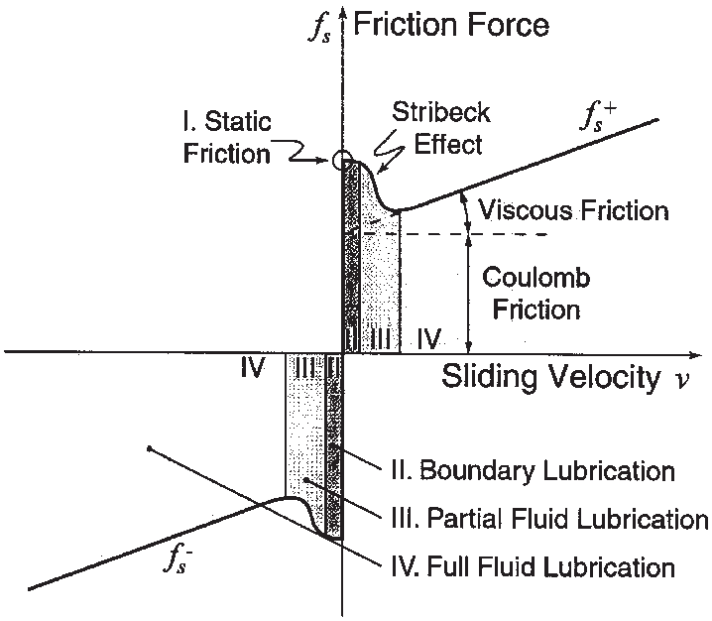

Figure 3.3 More realistic friction forces in motion control system [90].

From equation 3.2 sum of friction force of mover can be written as:

$$F_r = F\ v(t) + F_c + F_s \tag{3.3}$$

Where: F_r is the total friction force, F is the viscous friction coefficient and $v(t)$ is the linear velocity of mover.

As shown in equation (3.3) the friction force can be subdivided into three terms such as coulomb friction, viscous friction, and static friction force. In motion control system, friction forces deteriorate control performance. The general friction model is shown in figure 3.2. And figure 3.3 shows a combination of the friction force action on motion control system. As can be seen from figure 3.3 at low velocities, it is challenging to identity an appropriate function for friction force due to the non-linear nature of this force, which shows time-varied features [91]. If the static friction forces and Coulomb friction forces are included in F-load, then according to Kirchhoff's and Newton's law, the causal differential equation for the motion of the DC linear motor can be written as:

$$\frac{dv(t)}{dt} = \frac{Ki_t}{M} - \frac{F\,v(t)}{M} - \frac{F_{load}}{M} \quad \text{dynamics of motor velocity} \tag{3.4}$$

$$\frac{di_a}{dt} = -\frac{R_a i_a}{L} - \frac{K_t V}{L} - \frac{e_a(t)}{L} \quad \text{dynamics of motor current} \tag{3.5}$$

Where: R_a represents resistance of the armature resistance, L represents armature winding inductance, K_t represents static thrust, and $e_a(t)$ gives armature winding terminal voltage, while the armature current is given by i_a and V is the armature voltage. Following in Eq. (3.4), (3.5), the linear motor's state equation is given as follows:

$$\begin{bmatrix} \frac{dv(t)}{dt} \\ \frac{di_a}{dt} \end{bmatrix} = \begin{bmatrix} \frac{-F}{M} & \frac{K_t}{M} \\ \frac{-K_b}{L_a} & \frac{-R_a}{L_a} \end{bmatrix} \begin{bmatrix} V \\ i_a \end{bmatrix} + \begin{bmatrix} 0 \\ \frac{1}{L_a} \end{bmatrix} e_a(t) + \begin{bmatrix} \frac{1}{M} \\ 0 \end{bmatrix} F_{load} \tag{3.6}$$

Where v and i_a are the state variables of the DC linear motor. There is a single input and output for the linear motor, and thus, with the assumption that F_{load} is equal to zero, it is possible to rewrite the linear motor's state space equation in the following way:

$$\dot{X}_l\,(t) = AX_l\,(t) + Be_a(t) \tag{3.7}$$

$$v(t) = CX_l(t) \tag{3.8}$$

Where: A, B, C and $\dot{X}$ are the system matrix, input matrix, output matrix and derivative of the state vector with respect to time respectfully.

After taking the Laplace transform of equations (3.7), (3.8). The transfer function for velocity of slider of the DC linear motor $V(s)$ to the armature voltage $E_a(s)$ is given by:

$$\frac{V(s)}{E_a(s)} = \frac{\frac{K}{M\,L_a}}{s^2 + \left(\frac{F}{M} + \frac{R_a}{L_a}\right)s + \frac{FR_a + K^2}{M\,L_a}} \tag{3.9}$$

The position of the motor in relation to armature voltage is found by multiply the speed by integration in time, $1/s$ as it shows in the block diagram in Figure 3.4.

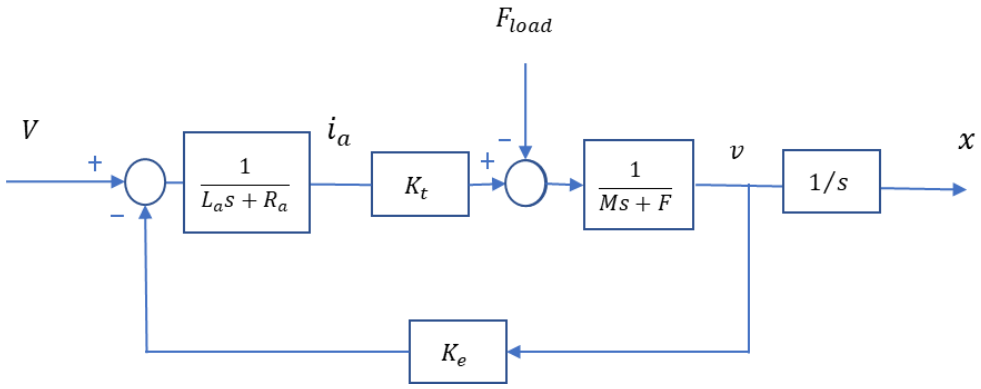

Figure 3.4. Block diagram showing transfer function of DC linear motor.

The transfer function of the DC linear motor can be described as a block diagram. Figure 3.4 shows the block diagram of the position control of the DC linear motor, where the input of the system is the armature voltage, and the output is the position.

From the block diagram, the transfer function of the position of the linear DC motor can be written as:

$$\frac{X(s)}{E_a(s)} = \frac{K}{L_a M S^3 + (R_a M + L_a F) S^2 + (R_a F + K^2) s} \tag{3.10}$$

Motor time constants are defined:

$$\frac{MR}{k_t^2} = T_m \qquad \frac{L_a}{R_a} = T_e \tag{3.11}$$

Where T_m and T_e are the mechanical time constant and the electrical time constant, respectively. Electrical time constant is much smaller than mechanical time constant usually neglected [92][93]. Reduced transfer function becomes:

$$\frac{X(s)}{E_a(s)} = \frac{b}{Ms^2 + as} \tag{3.12}$$

Where a is gain constant while b is system time constant, found as follows:

$$a = \frac{F R_a + K_b K_t}{R_a} \tag{3.13}$$

$$b = \frac{K_t}{R_a} \tag{3.14}$$

It should be noted that the two constants a and b are variable and do not have precise known values. In general, they are dependent on viscous friction and load mass [94]. The estimated parameters of the modelling linear DC motor are listed in Table 3.1.

Table 3-1 The estimated parameters of the modelling linear DC motor

Symbol	Description	Value
R_a	Armature resistance	7 Ω
L_a	Armature inductance	1.17 mH
M	Mover mass	7.9 kg
K_b	Back electromotive force constant	16.88 V/m/sec
K_t	Thrust constant	16.88 N/A
F	Viscous friction coefficient	32.07 N/m/sec

These parameters depend on the design of the motor such as type of motor, motor size thrust force ... etc. The mover has been chosen to contain 8 permanent magnets to make sure the movement is smooth when switching the energize of the coils. The winding has been designed to be the same size as the permanent magnet to get the highest force when it faces each other. The coil length influences the motor's force output, and the pole pitch affects the magnetic field distribution. These parameters have given the best results of the thrust force, linear motion and magnetic flux distribution in the modelling.

From electrical model of linear motor, thrust force is obtained, and from mechanical model of motor, position of the translator is attained.

$$M\ddot{x} + B\dot{x} + F_{load} = F_d \tag{3.15}$$

$$K_b\dot{x} + L_a\frac{dI_a}{dt} + R_aI_a = u \tag{3.16}$$

$$F_d = K_bI_a \tag{3.17}$$

Using equation 3.12~3.15, the simplified equation can be:

$$\ddot{x} = -a\dot{x} + bu - \frac{1}{M}(f_{\text{rip}} + f_{\text{fri}}) \tag{3.18}$$

3.2.1. Force ripple modelling

As mentioned earlier, cogging is a magnetic disturbance force resulting from the mutual attraction between the magnets of the translator and the iron cores. It is independent of the motor current and is solely determined by the relative position of these components. The fluctuation in the self-inductance of the windings regarding the corresponding location between the translator and the magnets causes the reluctance force. As a result, the reluctance force has a periodic connection with the location of the translator-magnet. The reluctance force occurs only when the motor current is greater than zero, and its absolute amount is determined by the needed force and the carriage's relative position. Cogging and reluctance force are often referred to as force ripple. In this research, the slot-less design has been used to reduce the cogging force.

Force ripple is particularly undesirable in terms of motion control. This can be reduced or even removed by designing the motor construction or the spatial arrangement of the magnetic materials differently, such as skewing the magnet, optimising the placement and breadth of the magnets, and so on. These techniques, however, frequently enhance the complexity of the motor framework. As a result, a control method that eliminates the impacts of force ripples is extremely desirable. Ripple models suggested by [95] will be utilized in this research. the force ripple can be described as:

$$f_{\text{rip}} = Asin(\omega x) = A_1 sin(\omega x) + A_2 cos(\omega x) \tag{3.19}$$

Where x represents the position of the motor carriage, A_1 and A_2 are the estimated coefficients, ω is the fundamental frequency.

The force ripple is modelled with an amplitude peak to peak is 5 (N), and ω is $14.15 * \pi * x_m$ (x_m is an actual position) which is modelled using MATLAB code as in figure 3.5 by using equation 3.18. These forces are applied as disturbance on the linear motor.

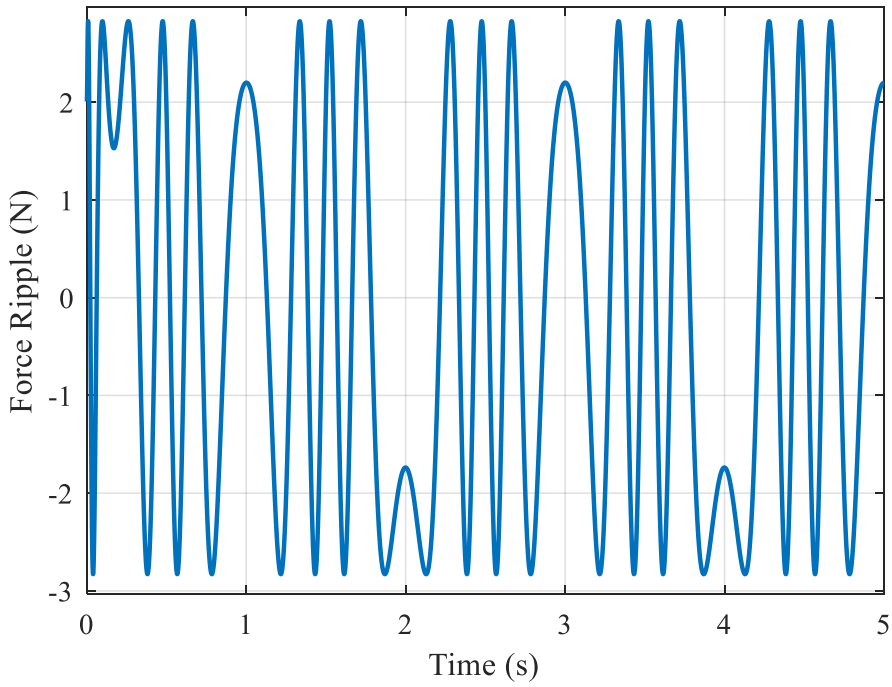

Figure 3.5 Estimated force ripple.

A simplified model for force ripple in a system dependent on the position of the mover can be represented using a sinusoidal or harmonic function. Force ripple often arises from periodic variations in the magnetic field, mechanical components, or control inputs

Figure 3.5 presents the simplified of modelling the force ripple which is dependent on the position of the mover.

3.2.2. Friction Modelling

The LuGre model will be utilised to model the friction force in this study. The LuGre model combines the Dahl model's dominant behaviour with the steady state friction prevalent in sliding regimes for example the Stribeck effect. The dynamic LuGre friction model's strength is its ability to represent a wide range of empirically observed friction occurrences [91].

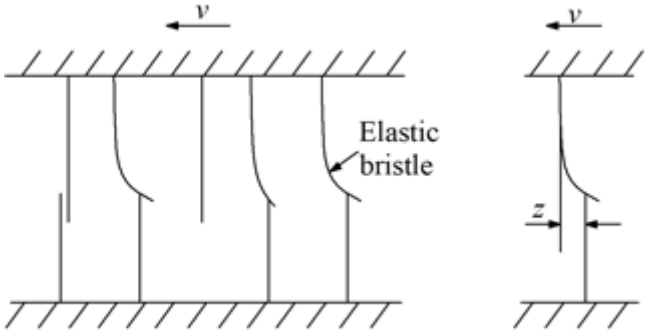

Figure 3.6 LuGre model [96]

The LuGre model is useful for representing the lower velocity motion of a linear motor. As shown in figure 3.6, the friction force may be described as a function of the state variable z and velocity v using the LuGre friction model [97].

The LuGre model is defined by [98]:

$$F_r = \sigma_0 + \sigma_1 \dot{z} + \sigma_2 v \tag{3.20}$$

where the parameters σ_0 , σ_1 and σ_2 are the stiffness coefficient, the micro-viscous friction coefficient, and the viscous friction coefficient, respectively. The interpretation of the internal state is linked to the bristle friction model; viz. the state variable z represents the average deflection of the elastic bristle:

$$\dot{z} = v - \sigma_0 \frac{|v|}{g(v)} z \tag{3.21}$$

where g (v) is a decreasing function for increasing velocity with an upper limit equal to the F_s static force and a lower limit equal to the F_c Coulomb friction force:

$$f_{\text{fri}} = sgn(\dot{x})\left(F_c + (F_s - F_c)e^{(\dot{x}/v_s)^2}\right) + B\dot{x} \tag{3.22}$$

Where F_s is static force, F_c is Coulomb friction force, B is the equivalent viscous friction coefficient, and v_s is the Strobeck velocity.

The static parameters can be estimated by construction between friction and velocity plan obtained from constant velocity motion. In Figure 3.7 friction function according to LuGre model has been illustrated via MATHLAB code with an estimated parameter of F_s =32.07(N), F_c=25.01(N), and v_s = 0.04(m/s).

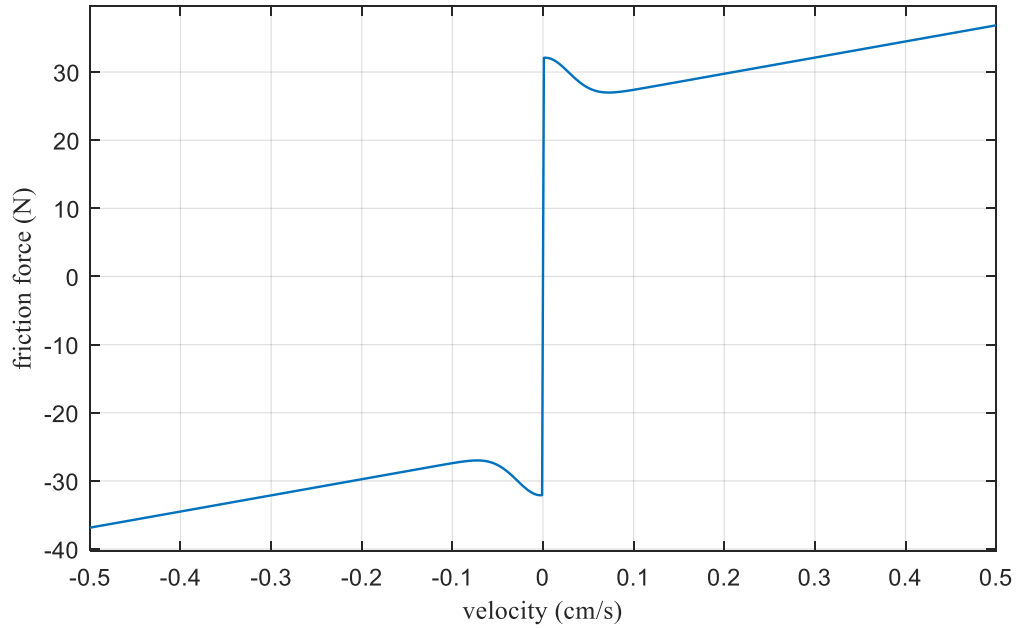

Figure 3.7 Steady state friction and velocity curve.

The friction forces along different sinusoidal trajectories were produced according to the friction model. And then injected into the system of the stage as disturbances. Figure 3.8 shows estimation of modelled friction forces.

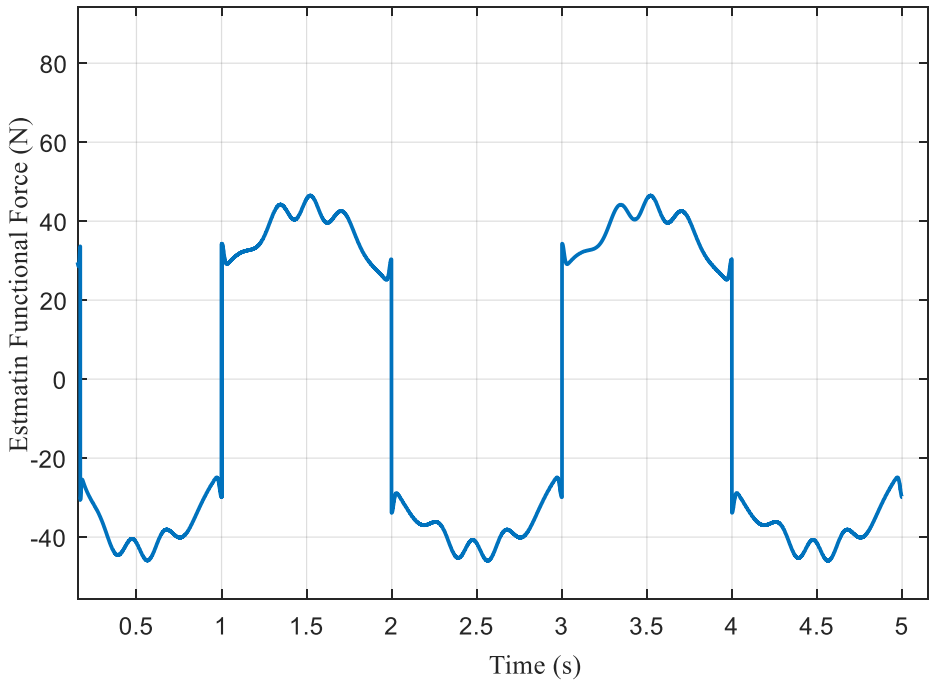

Figure 3.8 Estimation of modelled friction and ripple forces

To study the friction behaviour, a simulation and experiment were carried out to investigate the effects of friction and force ripple on the system response. Open loop simulations using MATHLAB/SIMULINK were performed to model the motion behaviour of a slotless DC linear motor under the influence of friction and force ripple, and then compared with the real time experiment. The step response is used as speed reference trajectory.

Figure 3.9 shows real-time and simulation of open-loop step response for the velocity of slotless DC linear motor with both friction and force ripple.

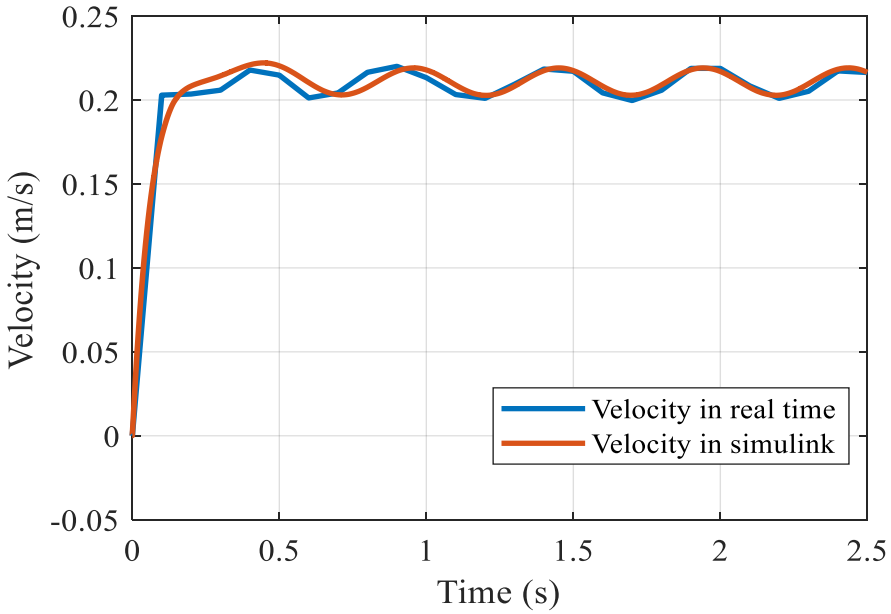

Figure 3.9 Comparison of simulation and measured velocity response of a linear motor

From the graph, it can be seen the effect of the force ripple and friction force on the velocity of the motor, also the simulation results match the real time experiment values aligns well, which means this model can predict the response of the real linear DC motor.

3.3. Modelling of slotless DC linear motor

The design of electric machines requires comprehensive knowledge of the quantitative and interrelation of the magnetic field in every part of the system, particularly the field distribution in the airgap region. In PM linear DC machines, the magnetic flux is

established by permanent-magnet and linked with the armature winding to generate thrust force. This force is proportional to the armature current and the flux linkage. Flux linkage and armature current are the key parameters to determine the characteristics of thrust force -speed curve in electric machines.

In order to acquire a comprehensive understanding of the machine characteristics and a more precise brushless DC linear motor design, a finite element method (FEM) analysis is initially performed according to the preliminary geometry [99]. The most important methods used for analysing the magnetic field in machine design are:

1. Finite Element Method (FEM)
2. Finite Difference Method (FDM)
3. Boundary Element Method (BEM)
4. Magnetic Equivalent Circuit (MEC)

The Finite Element Method (FEM) is a numerical technique used to analyse the behaviour of complex structures and systems, such as brushless linear DC motors. The FEM involves dividing the structure or system into smaller, simpler elements and applying mathematical equations to each element to determine its behaviour. These equations are then combined to analyse the behaviour of the entire structure or system.

To use the FEM for design and analysis of brushless linear DC motors, the following steps can be taken:

1. Define the geometry of the motor: This involves creating a computer-aided design (CAD) model of the motor, including its dimensions, materials, and other relevant properties.
2. Meshing: Divide the motor geometry into smaller elements or nodes to simplify the analysis. The size and shape of these elements will depend on the accuracy required and the complexity of the motor.
3. Define the physical properties: Assign physical properties to each element or node, such as conductivity, permeability, and magnetic properties.
4. Define the boundary conditions: Specify the environmental and operational conditions that will affect the motor, such as temperature, magnetic fields, and electrical currents.

5. Solve the equations: Use mathematical equations to solve for the behaviour of each element or node under the defined physical and boundary conditions.
6. Analyse the results: Examine the results of the FEM analysis to determine the behaviour of the motor under various conditions. This analysis can provide valuable insights into the design and optimization of the motor.
7. Optimize the design: Use the results of the FEM analysis to optimize the design of the motor, including its size, shape, and materials. Iterative FEM analyses can be used to refine the design until the desired performance is achieved [100].

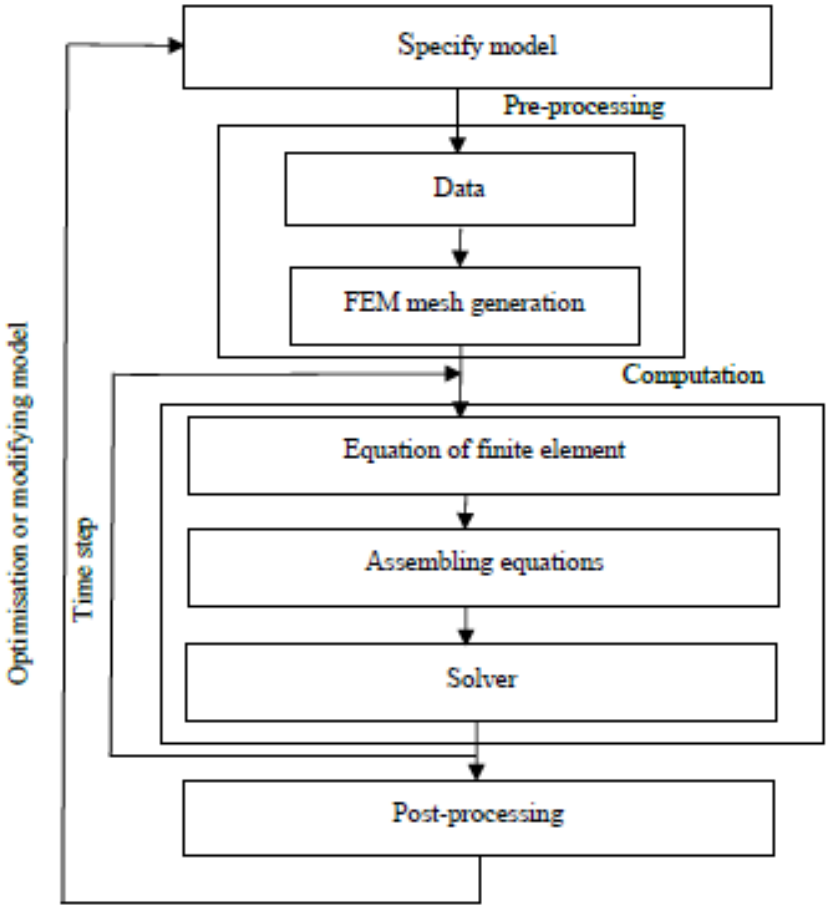

Figure 3.10 Finite element method simulation steps [100].

“MagNet” is a computer software that can be used to simulate the behaviour of a brushless linear DC motor. This software utilizes the finite element method (FEM) to model and analyse the electromagnetic and mechanical behaviour of the motor.

The software comprehensively models various motor elements, encompassing magnetic fields, current distribution, and mechanical deformation. It also simulates motion and force dynamics under diverse operational scenarios. To simulate a brushless linear DC motor using "MagNet," initial steps involve creating a detailed motor model within the software. This process includes defining the motor's geometry (incorporating stator, rotor, and specified materials) and setting operational conditions like voltage, current, and speed. "MagNet" then employs this data to simulate the motor's behaviour, covering magnetic field distribution, current flow, and resultant motion and force dynamics.

3.4. Selection of materials

Several factors were taken into consideration in designing the linear DC motor, including the thickness of the armature wire, armature core material and magnetic material. The choice of magnetic material for the motor is important, as it has to resist corrosion and withstand arduous environmental and climatic conditions. It must also have a high saturation flux density, to produce a motor with a high air-gap flux density and a very high output force.

3.4.1. Magnetic material properties

The magnetic material utilised in the motor design is critical. The magnetic material used to build the motor armature core should have a high saturation flux density, permeability, and the hysteresis loop should be as large as possible [101].

In an electric motor, the magnetic flux which is produced by the permanent magnet is guided by elements made of alloys of iron in order to close the magnetic circuit. If the magnetic flux to be guided has only a DC component, then the magnetic material used for the core and back iron can be a non-laminate iron alloy. However, if the magnetic flux has a high amplitude AC component and a high frequency, those magnetic material must be laminated in order to decrease as much eddy current losses as possible [102].

The flux densities in the teeth and cores are usually selected around the knee point of

the B-H curve. The material used for the construction of the armature core of dc linear motor is mild steel material, with a knee flux density around 1.4 T. However, with the improvement in magnetic material over the past few years, core materials with saturation flux densities as high as 2.2 T is employed [42].

3.4.2. Permanent magnet material

The choice of PM materials used is an important factor to consider in motor design. A permanent magnet with high remanence, high coercivity, wide range of temperature and low cost is highly desirable in the design of electromechanical energy converters [12]. Rare-earth permanent magnets are usually used for electrical motor design. The strength of the magnet makes it more practical to use, since it requires less space within an electric motor. The quality of the permanent magnet is judged based on its demagnetization curve, which is the part of the hysteresis loop that lies in the second quadrant between the residual flux density and the negative coercive force.

An important parameter to be considered when choosing a permanent magnet material is the point on the demagnetization curve where the B-H product is maximum. At this point the volume of the magnetic material required will be at its minimum. Magnet technology over the recent years has progressed rapidly due to the introduction of rare-earth materials, which have a high coercive force, a high flux density and large energy product [12].

A compromise between cost and performance was made in choosing the rare-earth magnet used. Samarium cobalt magnets (SmCo5) are most desirable. However, they are more expensive. NdFeB magnets are more expensive than ferrite and alinco but have high energy product density which provide an advantage of a compact size and efficiency.

For the motor design used in this project, the armature windings were excited for a very short period in other to eliminate the thermal effects. Therefore, the temperature requirement of permanent magnets is not strict. The magnets chosen were rectangular neodymium iron boron (NdFeB) magnets. The two major advantages of NdFeB magnets are that they can produce a higher energy product and are cheaper than Samarium cobalt magnets.

3.5. Modelling of slotless DC linear motor

In order to investigate the static characteristic of a thrust force and the air-gap magnetic flux density under the DC current excitation condition, while taking the nonlinear properties of iron materials used into account, the two-dimensional finite element method (FEM) is carried out using a “MagNet” software.

The motor is chosen and developed to be a DC linear slotless motor, and mover with 213 mm length which is consist of eight permanent magnet (NdFeB) blocks. Each side of the slider has four PMs arranged as N-S-N-S. These PMs are separated by three Tufnol blocks to isolate the magnets. The back iron was placed in the field housing in order to close the magnetic circuit generated by PMs. The armature core has been designed as a rectangular shaped armature core made of mild steel bar. Figure 3.11 shows the geometry of the proposed motor.

After an extensive review of pertinent research and an empirical investigation involving computer-based experimentation, the attributes featured in table 3.1 emerged as the most optimal parameters for designing a slotless DC linear motor, with the overarching objective of mitigating force ripple. Consequently, these attributes were incorporated into the motor's final design.

Table 3.2 shows the major characteristics and material specifications for the slotless linear DC motor.

Table 3-2 Dimensions and material specification of the linear dc motor.

Magnet dimensions [mm]	42x 20 x 30
Magnet type	Neodymium Iron Boron
Number of magnets	8
Core dimension [mm]	288 x 30 x 30
Core	Mild steel
Back iron dimension [mm]	99 x 30 x 5
Tufnol blocks [mm]	l5x30x20
Effective Air gap [mm]	20
Supply Current [A]	3

The armature windings are distributed along the armature core. There are twenty-eight independent multi-layer coil sections distributed along of the armature core with enamelled copper wire with 0.5mm.

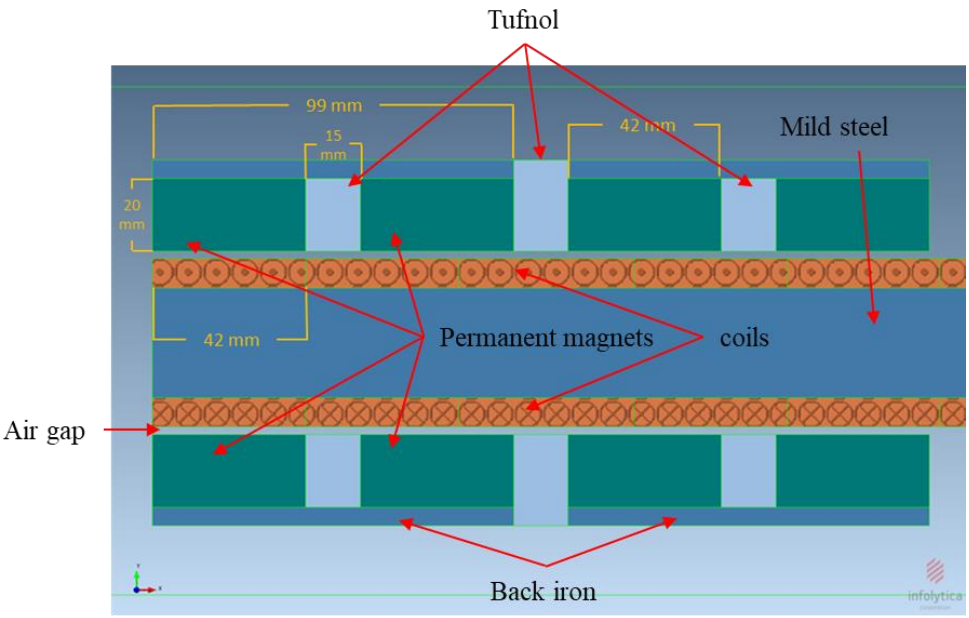

Figure 3.11 Layout of the proposed linear DC motor.

Before the post-processing stage of the simulation, an optimal mesh size has to be selected in order to achieve a better result. In the 2D finite element method of analysis, the solution domain is divided into a mesh of triangular elements. The accuracy of the solution depends upon the nature of the field and size of the mesh elements. In regions where the direction or magnitude of the field is changing rapidly, high accuracy requires smaller elements. One method of increasing the mesh density is to set the maximum element size for a component volume or specific face a component as in Figure 3.12.

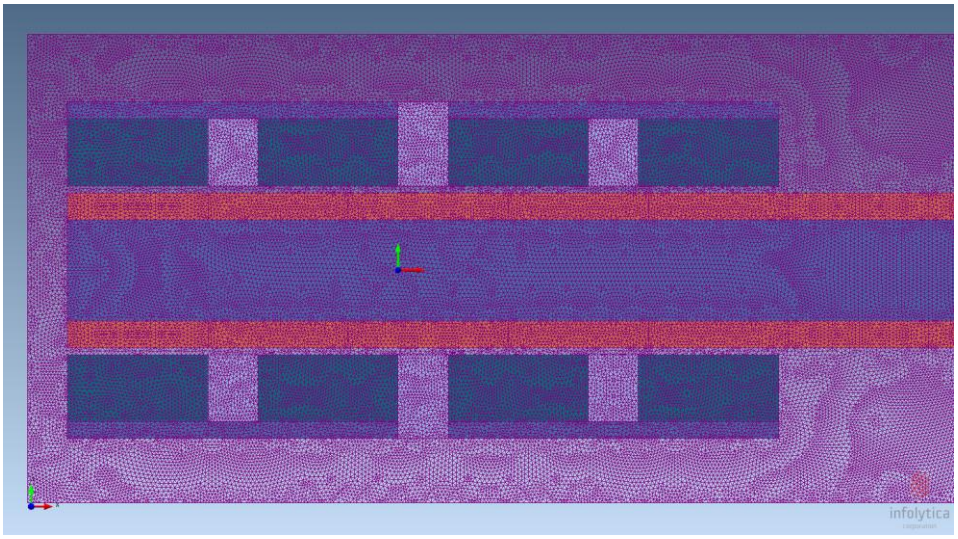

Figure 3.12 Mesh of 2D of the of the linear DC motor

3.6. Summary

This chapter presents a dynamic model of linear DC motor. In this work, a dynamic friction model is used to capture not only observed static friction phenomena but also dynamic friction phenomena, which is the prevailing friction phenomenon for high precision applications. Friction behaviours under step input were investigated. The friction force was modelled versus velocity according to LuGre model as in Figure 3.7, and the estimate modelled forces as in Figure 3.8 has injected to the system as disturbances. The results of experiments showed that the designed LuGre model could estimate such forces accurately. also in this chapter, a Finite Element Method (FEM) study utilising "MagNet" was employed to modelling and construct a slotless DC linear motor. The comparison is entail evaluating both the simulated and model designs, focusing on static thrust, air-gap flux density, and magnetic flux distribution. The methodology used to model magnetic materials and permanent magnets is extensively elucidated. This chapter gave further details the preparatory operations, encompassing mesh construction, defined boundary conditions, and the excitation sources utilized.

Chapter 4: Sliding Mode and Tuning Parameters Control using Bee's Algorithm.

4.1. Introduction

This chapter proposes a robust motion control framework which combines the merits of a reaching law-based sliding mode control and the disturbance estimation using a disturbance observer for precision tracking to address the practical issues of friction, and force ripple disturbances. The proposed control algorithm maintains the robustness of sliding mode control to parameter variations and external disturbances while attenuating the chattering which is often a major obstacle to practical implementation of sliding mode control.

4.2. Sliding mode control

The control solutions often use system models, these models may not be perfect representations of the actual systems due to simplifications in modelling techniques, variations in system parameters over time, and other factors. This recognition is crucial for understanding the limitations and potential inaccuracies in control systems based on these models. The model uncertainty refers to the disparity between the plant model and the actual system. Furthermore, the genuine system is constantly subjected to certain external disturbances while in operation. A well-designed control system must ensure the intended performance during model uncertainty and disruptions [103].

Inaccuracies in modelling can have a significant negative impact on nonlinear control systems. Robust control is one of the most essential techniques of coping with model uncertainty. The typical structure of a robust controller is composed of a nominal part, similar to a feedback control law, and additional terms aimed at dealing with model uncertainty.

Sliding mode controller design gives a systematic solution to the challenge of maintaining stability and consistent performance in the face of modelling imprecision for the class of systems to which it applies. On the other hand, by allowing the trade-

offs between modelling and performance to be measured in a straightforward manner, it may provide light on the whole design process [104].

4.2.1. Principles of sliding mode control systems

The process for sliding mode control SMC design consists of the following steps:

1. A sliding surface is predefined in a way that desired system dynamics are achieved during sliding mode.
2. A controller is designed to drive the closed-loop dynamics to reach and retain the sliding surface.

4.2.2. Sliding Mode Surface Design

Without loss of generality, the slotless dc linear motor can be considering the following linear time-invariant (LTI) equation: [111].

$$\dot{x}(t) = Ax(t) + Bu(t) \tag{4.1}$$

where $x \in R^n$ is the system state vector, $u \in R^m$ is the control input vector, $A \in R^{n\times n}$ and $B \in R^{n\times m}$ are constant system matrices.

Where $x(t) = \begin{bmatrix} v(t) \\ i_a(t) \end{bmatrix}$, $A = \begin{bmatrix} \frac{-F}{M} & \frac{K_t}{M} \\ \frac{-K_t}{L_a} & \frac{-R_a}{L_a} \end{bmatrix}$, $B = \begin{bmatrix} 0 \\ \frac{1}{L_a} \end{bmatrix}$

Define a sliding variable vector $s(t) \in R^m$ passing through the state space origin:

$$s(t) = Cx(t) \tag{4.2}$$

where $C \in R^{n\times m}$ is the sliding mode parameter vector and $|CB| \neq 0$. The equation (4.1) is said to attain a sliding mode surface when the state variable vector reaches and remains on the intersection of the m switching plane variables. The method of equivalent control is a way to determine the system motion restricted to the sliding mode surface $s(x) = 0$. On the sliding mode surface, $s(x) = 0$ and $\dot{s}(x) = 0$, using equations (4.1) and (4.2), become:

$$\dot{s}(t) = C\dot{x}(t) = 0 \tag{4.3}$$

$$C\left(Ax(t) + Bu_{eq}(t)\right) = 0 \tag{4.4}$$

where $u_{eq}(t)$ is viewed as equivalent control.

From equation (4.4), the equivalent control can be expressed as:

$$u_{eq}(t) = -(CB)^{-1}CAx(t) \tag{4.5}$$

Substituting (4.5) into (4.1) yields the following equation.

$$\dot{x}(t) = [I - B(CB)^{-1}C]Ax(t) \tag{4.6}$$

The equation (4.6) is called the equivalent system equation which describes the dynamic motion of the equation (4.2) on the sliding mode surface.

The dynamical behaviour of the equivalent system is independent of the control input. Thus, the determination of the matrix C (sliding mode parameter vector) may be completed without prior knowledge of the form of control input. Generally, the sliding parameter C is designed in a manner that the system response confined on the sliding mode surface equation (4.6) has a desired behaviour such as asymptotic stability and prescribed transient response. According to the linear control theory, in order to guarantee the solution of the equation (4.6) to be asymptotically stable, the sliding mode parameter vector C should be chosen, such that all the eigenvalues of the equation (4.6) have negative real parts. What's more, though the sliding surface is linear, it indeed could be any other forms with nonlinearity to ensure a finite time convergence of system dynamics in sliding mode.

4.2.3. Reaching Phase

SMC design includes reaching phase and sliding phase. The reaching phase is crucial in the sense that the system dynamics are guaranteed to reach the sliding surface and be retained on it thereafter. For a case in point, the idea of a sliding mode of a second order system can be depicted in Figure 4.1

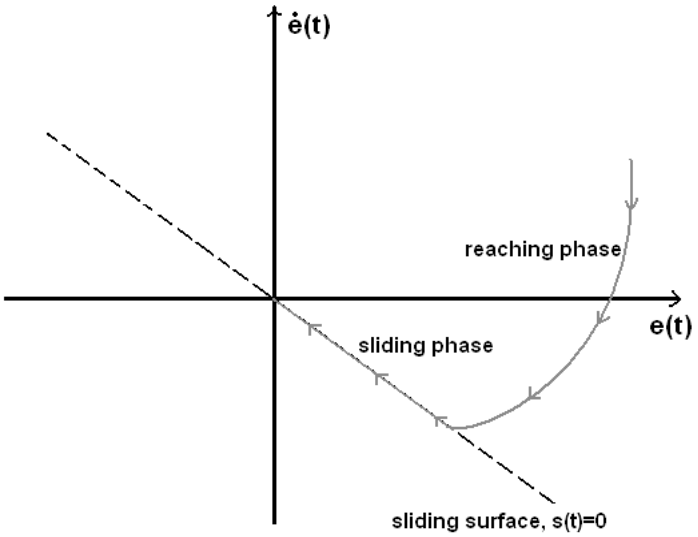

Figure 4.1 Phase trajectory

The phase trajectory in sliding mode control demonstrates the evolution of the system's state variables concerning time or any other independent variable, typically plotted in the state space. The state space represents the complete set of the system's state variables. When the system is in sliding mode, the phase trajectory essentially follows the sliding surface or stays very close to it. The objective of sliding mode control is to force the system state to stay on this surface, exhibiting a behaviour determined by the control law. The dynamics in sliding mode control are often characterized by the fast motion along the sliding surface, achieving robustness against uncertainties and disturbances. This characteristic behaviour can be observed in the phase trajectory, illustrating how the system state variables evolve while adhering to the sliding surface.

The next important problem is how to design a controller to guarantee the reachability of the sliding variable to the sliding mode surface. Therefore, the task of the sliding mode controller is to drive the sliding variable s to converge to zero, and then the desired system dynamics prescribed in (4.6) will be obtained.

4.2.4. Reaching Condition

In fact, the condition for the switching plane variables to reach the sliding mode surface is a convergence problem. Therefore, the Lyapunov's direct method has been widely used in SMC designs as a stability condition to ensure the convergence of the sliding

mode variable onto the sliding surface during the reaching phase. All too often, the following Lyapunov function candidate is used in the sliding mode controller design:

$$V = \frac{1}{2} * s^2 \tag{4.7}$$

Where V is Lyapunov function

In order to guarantee the asymptotic stability of the equation (4.1) about the equilibrium point $x(t) = 0$, the following reaching condition must be satisfied:

$$\dot{V}(t) = s^2(t)\dot{s}(t) < 0 \text{ for } s(t) \neq 0 \tag{4.8}$$

The condition (4.8) indeed acts as a sufficient condition to ensure the existence of the sliding mode. It is worth noting that most of the sliding mode controllers are designed based on the reachability condition in (4.8) to ensure the sliding mode controller can drive the sliding variable $s(t)$ to asymptotically converge to zero.

4.2.5. Lyapunov Stability

As the nonlinearities and possible time-varying parameters exist in the nonlinear systems, linear stability criteria, e.g., Routh's stability criterion or Nyquist stability criterion cannot be generalized and carried over into the systems for stability analysis. The Lyapunov stability theory introduced in this section is the most general approach to determine the stability of the linear or nonlinear dynamical systems. A system can be described by

$$\dot{X} = f(X, t) \tag{4.9}$$

Where $X \in R^n$ is the state variable and $f(X, t) \in R^n$ is a set of functions of $x(t)$. A solution $x(t)$ of the equation $\dot{X} = f(X, t)$ usually corresponds to a curve in the state-space as t varies from zero to infinity. This curve is generally referred to as a state trajectory or a system trajectory.

4.2.6. Reaching Laws

SMC can be designed based on reaching laws to guarantee the existence of the sliding mode. Some possible types of reaching laws are given in [27]. In general, reaching law can be generalized in the following form:

$$\dot{s} = -ksign(s) - f(s),\ k > 0 \tag{4.10}$$

Where k is a positive constant, $f(0) = 0$ and $f(s) > 0$ when $s \neq 0$.

In practice, three special reaching laws commonly used can be derived from equation above.

In this research the power rate reaching law will be used which can be described as:

$$\dot{s} = -ksign(s),\ k > 0 \tag{4.11}$$

This law constrains the switching variable to reach the switching manifold at a constant rate k. The merit of this reaching law is its simplicity.

It is evident that the above reaching laws can satisfy the reaching condition, and thus ensure the existence of the sliding mode. It is worth nothing that a reaching law method simultaneously takes care of ensuring the reaching condition, influencing the dynamic quality of the system during the reaching phase, and providing the means for controlling the chattering level. Thus, a reaching law method can be applied to both linear and nonlinear SMC systems with system perturbations and external disturbance, in order to improve the performance of the reaching phase and reduce the amplitude of chattering[105].

4.3. Equivalent Controller Design

In most of the Variable structure control (VSC) schemes, the control input usually consists of two components as follows:

$$u(t) = u_{eq}(t) + u_s(t) \tag{4.12}$$

where the linear component $u_{eq}(t)$ is defined as in (5.5) and the nonlinear signal incorporates the discontinuous component given below

$$u_s(t) = -\eta(CB)^{-1}sign(s(t)) \tag{4.13}$$

where $\eta > 0$ is a constant control gain.

Substituting (5.5) and (5.13) into (5.8) leads to

$$\dot{V}(t) = s^2(t)CAx(t) + s^2(t)CBu(t) \tag{4.14}$$

$$= -\eta|s(t)| < 0$$

From the equation (4.16), it can be concluded that the sliding mode variable is guaranteed to reach the sliding mode surface in finite time[104].

After the sliding variable vector $s(t)$ is driven to zero, the closed-loop system dynamics are only determined by the desired dynamics in (4.7) and thus, the closed-loop system is insensitive to system uncertainties on the sliding mode surface. For this reason, SMC systems possess the property of robustness with respect to system uncertainties, that SMC becomes a powerful tool in the control of uncertain systems and significantly motivates the subsequent researchers in the area. However, it should be noted that the system remains affected by the perturbations during the reaching phase before the sliding surface has been reached.

Robustness property is an important feature of SMC system. The system uncertainties and disturbances are always factored in an SMC controller design. With consideration of system uncertainties and disturbances, the LTI system in (4.1) can be generalized as

$$\dot{x}(t) = (A + \Delta A)x(t) + (B + \Delta B)u(t) + d(t) \tag{4.15}$$

where ΔA and ΔB are the system uncertainties and $d(t)$ is the external disturbances.

Equation (5.15) can be rewritten in the following form:

$$\dot{x}(t) = Ax(t) + Bu(t) + f(t) \tag{4.16}$$

where $f(t) = \Delta Ax(t) + \Delta Bu(t) + d(t)$ is the lumped uncertainty. Following the concept of equivalent control, one can design the controller form of (4.12), where $u_s(t)$ is defined as in (4.13) and the equivalent control is given by the following equation:

$$u_{eq}(t) = -(CB)^{-1}C(Ax(t) + f(t) \tag{4.17}$$

4.4. Design the Controller

In the proposed design of SMC, two parts are included, namely, the appropriate sliding surface selection to model the performance of the specific closed loop required; and the generation of the control law which force the trajectory of the system state in the direction of the surface. Prior to reaching the sliding surface, the system state trajectory is called the reaching phase. This phase system dynamics remain subject to influence from uncertain factors. The optimal situation is that control switching occur at a frequency in which infinitely high, as this would prevent deviations from the sliding manifold. In practical work, however, finite switching intervals is not possible, meaning that unwanted chattering is always present in the application of controls. The negative consequences of chattering come from its excitation of high-frequency plant dynamics not included in the modelling, which leads to unpredictable variations instability [106]. The general state-space equations can be rewritten as follows:

$$\text{State space equation } \dot{X} = AX + \text{Bu}$$

$$\text{Output equation } y = C\text{X}$$

Where X is the state vector and u is the control vector.

Next, sliding surface $s(e,t)$ can be selected through:

$$s\,(e,t) = \{e: \lambda^T\, e = 0\} \tag{4.18}$$

Where e is the error and t time.

That $\lambda \in R^{\text{n}}$ represents the coefficients, or slope of the sliding surface.

Typically, s (t) is a time-varying sliding surface with a simple definition within R^{n} as a state-space through the scalar equation as follows:

$$s\,(e,t) = \left(\frac{d}{dt} + \lambda\right)^{n-1} e = 0 \tag{4.20}$$

Where λ represents sliding surface slope as a strictly positive constant. This, assuming a value of 2 for n (within a 2nd order system)

$$s = \lambda e + \dot{e} \tag{4.21}$$

The position-tracking error is given as:

$$e = (x_r - x_m) \tag{4.22}$$

And

$$\dot{e} = (\dot{x}_r - v) \tag{4.23}$$

Where, x_r is the position reference signal, and the real position is x_m, with λ representing a positive constant. Therefore, the sliding surface (s) expressed in equation (4.21) is formed as the weighted sum of position and velocity error. Here, a stabilisation problem in the first order replaces the previous n-order tracking problem, and in the new problem, s scalar is held at a value equal to zero through controlling a reaching condition. Lyapunov function's second theorem is selected to write the stability condition,

$$v(x) = \frac{1}{2} * s^2 \tag{4.24}$$

The equation below then always meets reaching condition.

$$\dot{v}(x) = s\dot{s} < 0 \tag{4.25}$$

During sliding mode operation, chattering in the system's response occurs at $s = 0$. From equation (4.25), it is possible to rewrite existence and convergence condition:

$$s\dot{s} \leq \eta s \tag{4.26}$$

It can be shown that the sliding condition in equation (4.26) is always satisfied by:

$$u = u_{eq} - k * sgn(s) \tag{4.27}$$

Where equivalent control input, u_{eq} is found through $\dot{s} = 0$, while k represents a strictly positive constant.

The control signal can be found if state equation of system, which can be shown in (4.18), is substituted in (4.21), is acquired.

$$u = \frac{1}{b}\left[\ddot{x_r} + \lambda * \dot{x_r} + (a - \lambda)\dot{x_m} + \frac{1}{M}d + k.sgn(s)\right] \quad (4.28)$$

The boundary layer approach consists of inserting a boundary layer near the sliding surface so that a continuous control action replaces the discontinuous one when the system is inside the boundary layer [107]. More specifically, the sign function $\boldsymbol{sign}(\boldsymbol{s})$ of the discontinuous control component is often replaced with the saturation function $\boldsymbol{sat}(\boldsymbol{s})$, which can be expressed as:

$$sat(s) = \begin{Bmatrix} 1 & s > \Delta \\ ks & s \leq \Delta \\ -1 & s < -\Delta \end{Bmatrix} \quad (4.29)$$

Where Δ denotes the boundary layer, k=1/Δ. The essence of the saturation function is the adoption of the switching control outside the boundary layer and the linear feedback control inside the boundary layer [108].

In order to eliminate the chattering phenomenon, the sat function is adopted to replace the $sign$ function of the control law, where the sat function was defined as:

$$sat(s) = \begin{cases} sgn(s), & if|s| \geq \delta \\ \frac{s}{\delta}, & if|s| < \delta \end{cases} \quad (4.30)$$

Where, δ is a small positive constant that defines the boundary layer.

A large boundary layer leads to a larger steady-state error whereas a too small boundary layer leads to high frequency switching. Therefore, the designer must select the value of δ carefully.

To compensate for force ripple in a linear DC motor, the sliding surface can be chosen to be a function of the force ripple itself, as well as the desired force output and the actual force output of the system. The control law can then be designed to force the system to follow the sliding surface, which will in turn compensate for the force ripple.

One way to implement sliding mode control for a linear DC motor is to use a sliding mode controller that includes a feedback loop. The feedback loop can be used to measure the actual force output of the system, and then adjust the control law accordingly to keep the system on the sliding surface.

Another approach is to use a disturbance observer technique with sliding mode control, which uses an observer to estimate the actual state of the system, which can then be used to eliminate the disturbance.

4.5. Disturbance Observer

A disturbance observer (DOB) is a control system component that is used to estimate and compensate for external disturbances or uncertainties in a system. Disturbances can be caused by various factors, such as changes in the environment, mechanical wear and tear, or measurement noise.

A disturbance observer works by measuring the difference between the actual output of a system and the output that would be expected if there were no disturbances or uncertainties present. This difference is called the disturbance error, and the disturbance observer uses it to estimate the size and frequency of the disturbances.

Once the disturbances are estimated, the disturbance observer can generate a compensating signal that is added to the control signal in order to counteract the disturbances and improve the system's performance. This compensating signal can be used in a variety of control systems, including servo systems, robotics, and automotive control systems, to improve the system's robustness and stability.

The disturbance observer (DOB) has been proposed to eliminate the disturbance which is difference between the actual system and nominal model as a mentioned above. The nominal model represents the desired model based on the desired control specifications. It makes the actual system to become a given nominal model. Figure 4.2 shows the classic structure of DOB for a single input single output (SISO) plant [109]. The output of DOB, $\hat{d}$ is an estimated disturbance which consists of the parametric errors between the actual plant and the nominal model of DOB and disturbance forces such as the force ripple, friction force, and load variation [110].

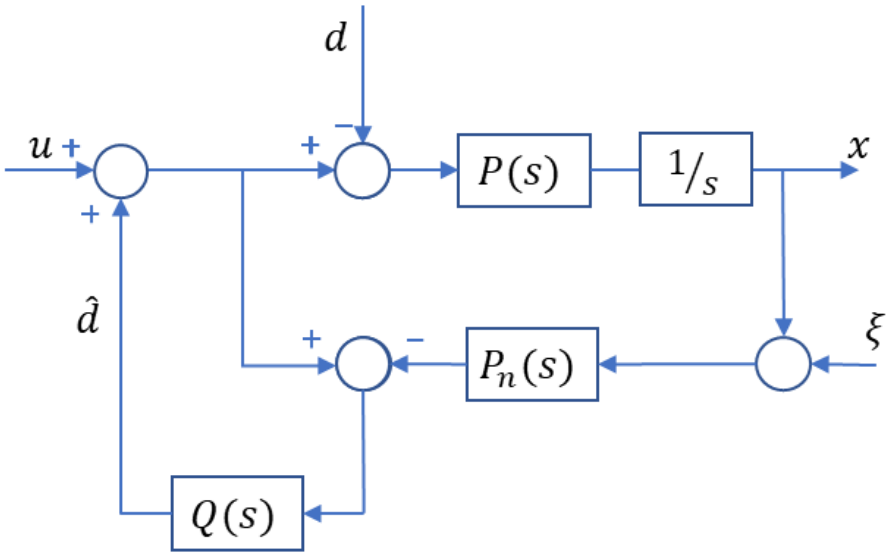

Figure 4.2 Classic structure of DOB [111].

The classic structure of a Disturbance Observer typically involves a few key components to estimate and compensate for disturbances affecting a control system. The main idea behind a Disturbance Observer is to estimate the disturbances affecting the system and then use this estimation to generate a compensatory signal to improve the system's performance.

Figure 4.2 shows the classic structure of DOB, where $P(s)$, $P_n(s)$, $Q(s)$, d, $\hat{d}$, u, x, ξ are actual plant, nominal plant transfer function, a low-pass filter, the disturbance (the force ripple, friction force, and load variation), the estimated disturbance the control input, the position of mover and the sensor noises, respectively [112].

4.6. Design of the lowpass filter parameter

The characteristics of a closed-loop system depends upon the choice of parameter Q(s), which is the most critical component in the DOB design. The design of the low-pass filter concerns the trade-off between 1- Q(s) and Q(s) to maintain insensitivity to both model uncertainty and measurement noise. The filter used in this study is a first order filter to have a simple computation [113][114]. The equation of the filter is expressed as the following equation.

$$Q(s) = \frac{1}{T_e s+1} \tag{4.31}$$

Where: T is the filter time constant which can be obtained by the electrical time constant of the DC linear motor as:

$$T_e = \frac{L_a}{R_a} \tag{4.32}$$

Assume that the current of the DC motor is well controlled. Then, the transfer function of a plant can be given by

$$P(s) = \frac{K_t}{Ms+F} \tag{4.33}$$

And the nominal plant is:

$$P_n(s) = \frac{Ms+F}{K_t} \tag{4.34}$$

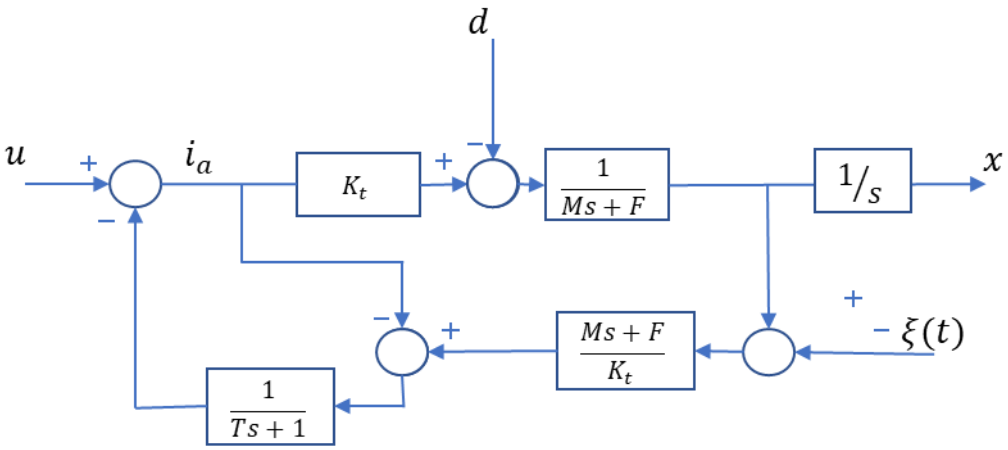

Figure 4.3 . Disturbance observer with the DC linear motor

The block diagram illustrating a system with a disturbance observer, where the parameters of the observer are derived from the parameters of the motor. Additionally, the diagram contains components such as the actual system, nominal system, low-pass filter, disturbance, and sensor noise.

From Figure 4.3, the input-output relationship can be obtained as:

$$x = \frac{PP_n}{G}u + \frac{PP_n(1-Q)}{G}d(t) - \frac{PQ}{G}\xi \tag{4.35}$$

Where:

$$G = 1/(P_n + (P - P_n)Q) \tag{4.36}$$

Assume that the low pass filter is stable and below the cut-off frequency $Q(s) \approx 1$, then the output can be simplified as

$$x = P_n\, u - \xi \tag{4.37}$$

Here the sensor noise ξ is much smaller than the force ripple so it can be neglected. The nominal input-output relation become as: $x = P_n\, u$ which is desired [109]. Consider the DC linear motor system in Figure 4.3 can be modified to the system as shown in Figure 4.4 using the equation below:

$$\frac{1}{T_e s+1}\ \frac{(Ms+F)}{K_t} = \frac{1}{K_t}\left(\frac{M}{T_e} - \frac{\frac{M}{T_e}+F}{T_e s+1}\right) \tag{4.38}$$

The final suggested DOB for DC linear motor is shown in Figure 5.4.

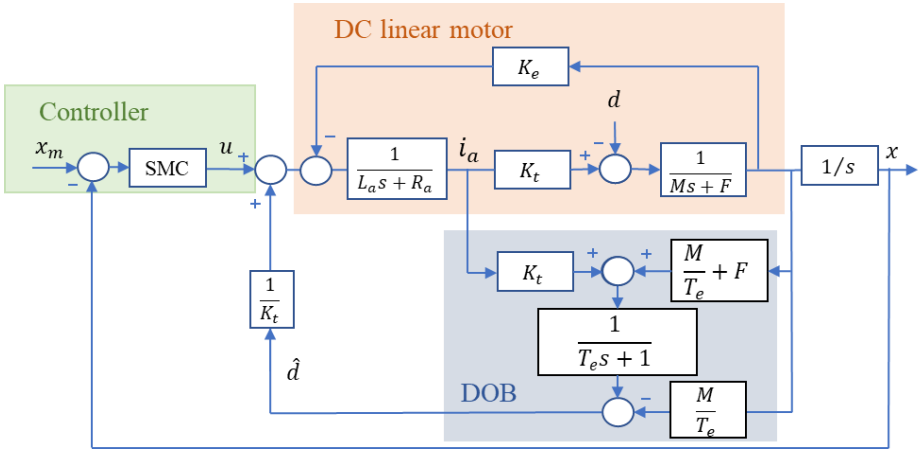

Figure 4.4 Suggested DOB-based DC linear motor.

The block diagram describes the final disturbance observer with a DC linear motor, where all parameters of the motor and the DOB are included. this block will be used in practice to reduce the force ripple.

The addition of the Disturbance Observer (DOB) to the control scheme enhances its capability to compensate for the presence of disturbances.

4.7. Simulation results and discussion.

Simulation analysis is carried out to verify the performance of the proposed nonlinear controller with disturbance observer and the effectiveness of the control strategy for speed and position tracking response of DC linear motor with the disturbance. The

simulations are implemented in MATLAB/SIMULINK, and the normal values of the linear DC motor parameters are listed in Table 3.1. This simulation includes two parts; the first part uses the reference trajectory for position as step response which has chosen to be as:

$$x_d = 0.250\ (meter)$$

second part is controlling the velocity of the same system by applying step function with speed *0.25 m/s.*

The frictional force is modelled as in Figure 3.3 using equation (3.22) with estimated parameters of F_s =32.07(N), F_c=25.01(N), and v_s = 0.04(m/s).

Also, the force ripple is considered with an amplitude peak to peak is 5 (N), and ω is $14.15 * \pi * x_m$ which is modelled as in Figure 3.1 by using equation (3.19), these forces are applied as a disturbance on the linear motor.

In order to avoid the chattering phenomenon, the switch function of sliding mode control law in (4.28) is replaced by saturated function in simulation.

The final control law that has been applied in Simulink with the nominal plant parameters and estimated force ripple is:

$$u = \frac{1}{2.411}\left[\ddot{x_r} + \lambda * \dot{x_r} + (72.77 - \lambda)\dot{x_m} + \frac{1}{7.9}(f_{\text{fri}} + f_{rip}) + k.sat(s)\right] \quad (4.39)$$

The parameters of the controller are chosen to be $\delta = 0.01, \lambda = 10\ and\ \ k = 450$, and the parameters of the DOB can be calculated from Table 3.1.

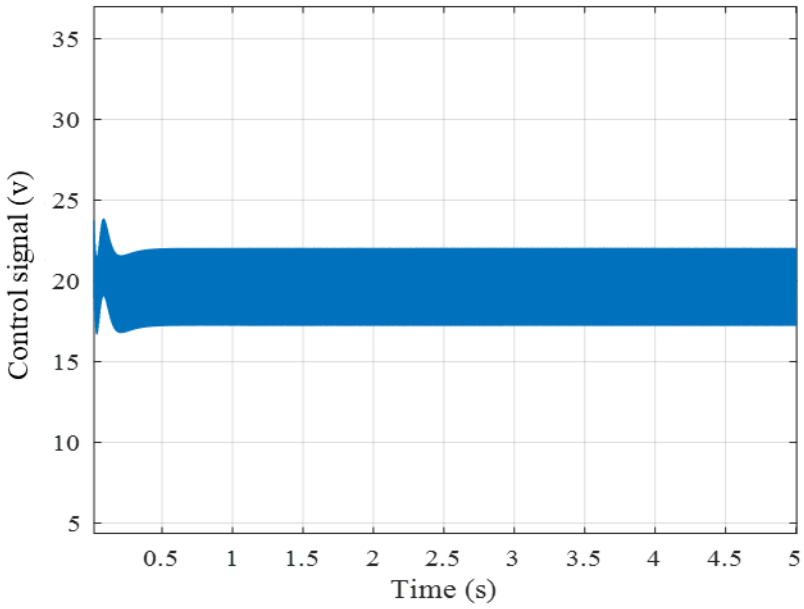

Figure 4.5 Actual control signal

When applying sliding mode control to the system, the controller generates a control signal based on the system parameters and controller gains. This signal is expected to exhibit a high switching frequency. Figure 4.5 illustrates the control signal of the sliding mode control (SMC).

The two-mode behaviour of the SMC controlled system is observable in Figure 4.6. The high frequency switching of control signals governs the trajectories of the system onto a designated surface referred to as the sliding surface. This surface is pivotal, as the system's output action is manifested through movement along it. The Sliding Mode Control (SMC) method endeavours to guide the system's states from the sliding surface to the origin. The progression within the sliding surface denotes the sliding mode, and the phase leading to this mode is known as the reaching mode. Notably, the system's states remain unaffected by changes in parameters and external disturbances. The primary objective of SMC is to ensure that the system's output precisely follows the desired reference, generating a signal 'u' that minimizes tracking errors. The system attains the sliding surface by transitioning between stable and unstable trajectories, ultimately achieving zero error convergence on the sliding surface. In this case, the chattering phenomenon is evident. To reduce this chattering, a the commonly used technique is the boundary layer around the switching surface has been used, and a continuous control has applied within the boundary as show in Figure 4.7.

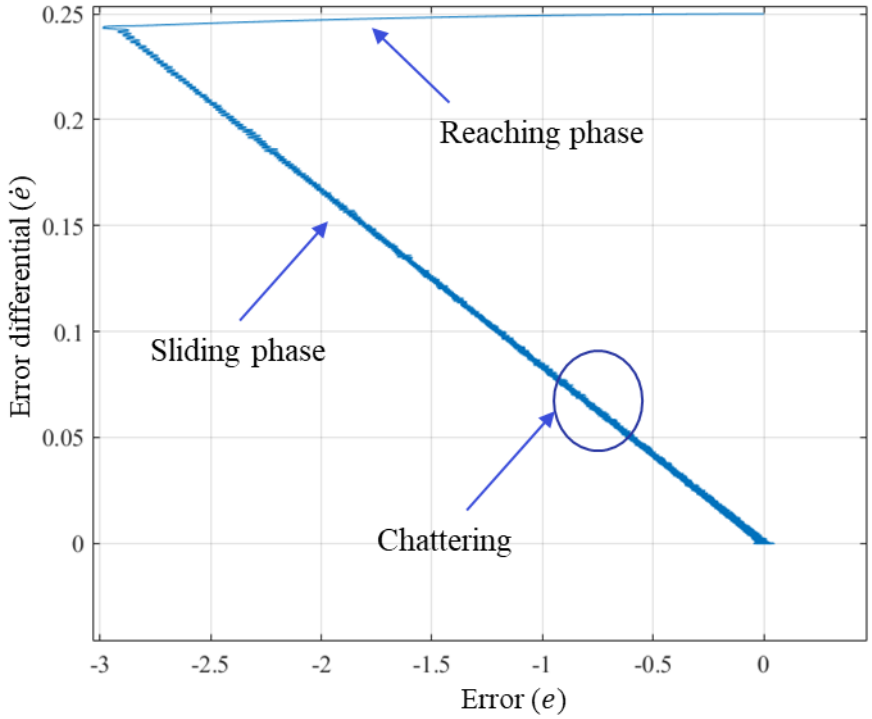

Figure 4.6 Phase trajectory with (sign) function

It seems that the proposed technique for eliminating chattering is effective Figure 4.7. However, some level of chattering is still present. As a result, a trade-off between system performance and acceptable chattering levels must be made. This trade-off can be critical in ensuring that the system operates efficiently while also meeting the desired control objectives. The level of acceptable chattering depends on the application and the specific requirements of the system. For some applications, chattering may be tolerable if it does not significantly impact the overall performance of the system. In other applications, however, even a small amount of chattering may be unacceptable. Therefore, it is important to carefully evaluate the level of chattering and its impact on the system's overall performance. This evaluation can be performed by analysing the system's response to different input signals and disturbances. Once the acceptable level of chattering is determined, the system can be adjusted to achieve the desired balance between performance and chattering reduction.

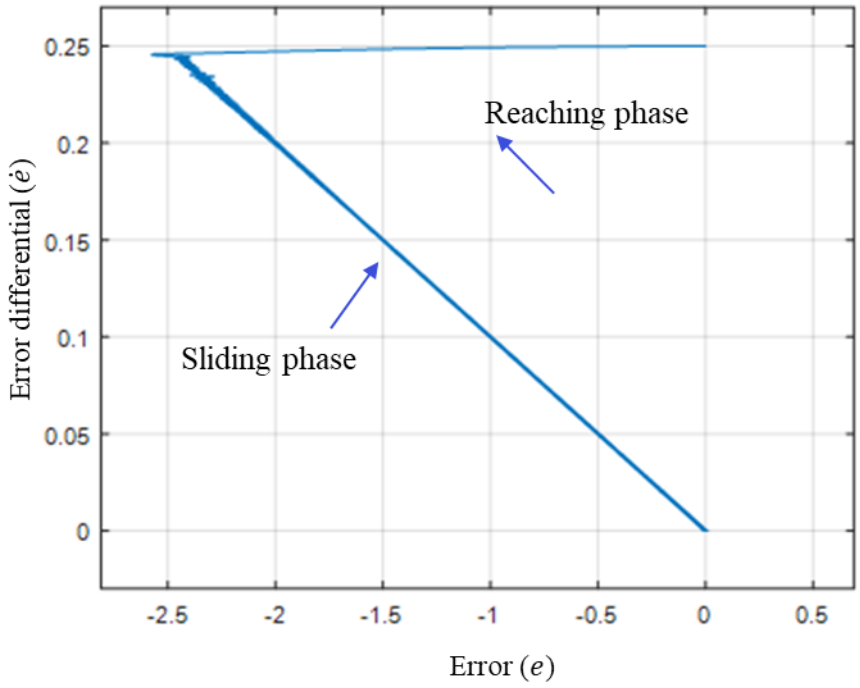

Figure 4.7 Phase trajectory with (sat) function.

Figure 4.7 shows a common solution to address the chattering phenomenon in control systems by substituting the sign function with a boundary layer. Chattering, characterized by rapid and erratic changes in control signals, can lead to system instability. The replacement aims to introduce a smoother transition in the control signals by leveraging the damping effect or filtering properties associated with a boundary layer near system boundaries. This adjustment is designed to mitigate the abrupt variations that contribute to chattering, offering a potential means of enhancing system stability and performance. The effectiveness of this solution depends on the specific characteristics and requirements of the control system in question.

Figure 4.8 shows the dynamic response of the DC linear motor implement SMC-with DOB and SMC-without DOB, and the characteristics of the response are given in Table 4.1, where the values of undershoot, overshoot, settling time, and rise time are illustrated.

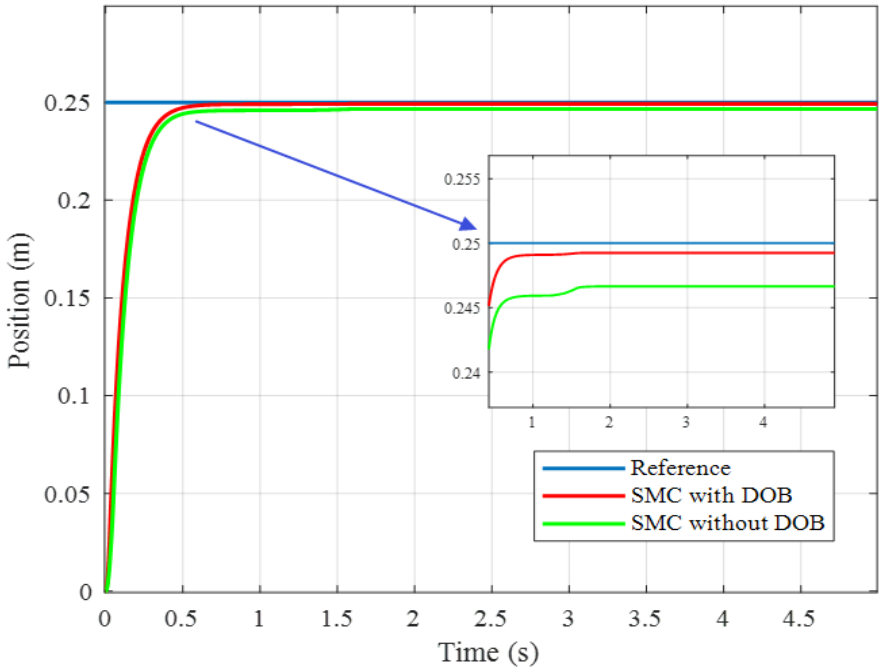

Figure 4.8 Step response of position control.

Table 4-1 The dynamic performance of the system with SMC for position tracking.

Control method	**Steady-State Error (per unit)**	**Overshoot (%)**	**Undershoot (%)**	**Rise time (sec)**	**Settling time (sec)**
SMC-with DOB	$\mathbf{0.759 \times 10^{-3}}$	0	0	0.2224	0.4110
SMC-without DOB	$\mathbf{3.357 \times 10^{-3}}$	0	0	0.2295	0.4259

The table presents the characteristics of the step response of both controller (SMC-with DOB and SMC-without DOB) parameters observed in a step response include the rise time (the time it takes for the system output to go from a specified lower value to a specified higher value), settling time (the time it takes for the system output to settle within a specified range around the final value), overshoot (the extent by which the system output exceeds the final value before settling), and steady-state error (the difference between the final value and the actual output in the long run). Analysing the step response is crucial in evaluating and tuning the performance of position control systems, providing insights into their transient and steady-state characteristics.

From Figure 4.8 and Table 4.1, an obvious improvement in the performance of the system is obtained when the proposed SMC is utilized. Moreover, it can be noted that SMC-DOB gives a better dynamic response in all aspects having a slightly smaller undershoot. Also, there is a slight effect of force ripple on the position between 1 and 2 seconds on the controller SMC. While, in the controller SMC with the disturbance observer, the error has been reduced, where the DOB works on the difference between the actual motor and the nominal design, then compensating the error and Injection with a control signal. The steady-state error is also reduced from 3.357×10^{-3} to 0.759×10^{-3} (per unit). These results suggest that the SMC-DOB system is more robust and efficient, with better disturbance rejection and tracking performance.

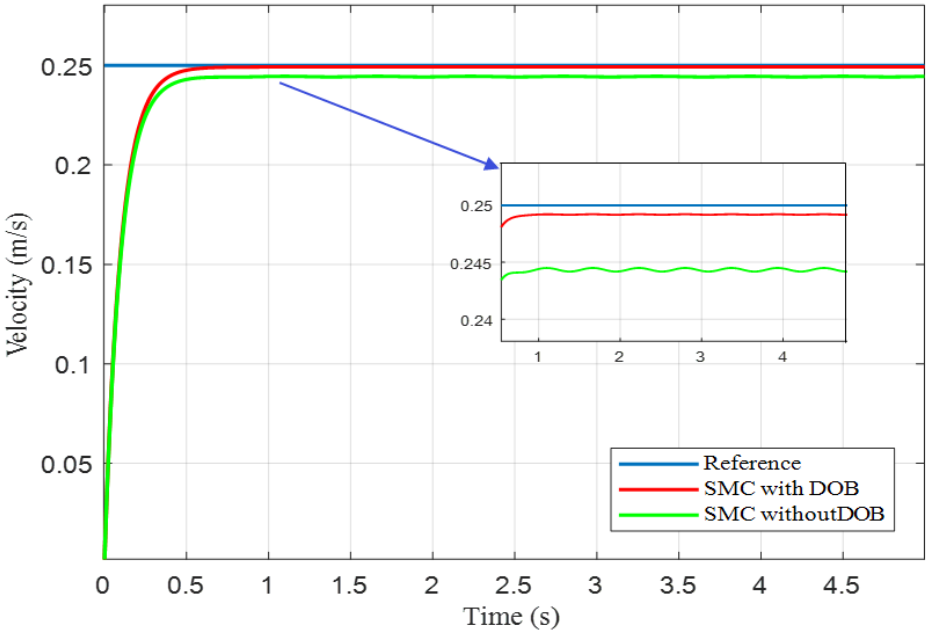

Figure 4.9 Step response of speed control.

Figure 4.9 presents the step response of the speed control with and without a Disturbance Observer (DOB) for the slotless DC linear motor. It is evident that the controller with the DOB reduces both the error and the force ripple when compared to the controller without the DOB. The Disturbance Observer operates to compensate for the error resulting from the force ripple. More details of the figure 4.9 presents in table 4.2.

The sliding mode control (SMC) has been used to achieve velocity tracking of a system, and the performance of the controller has been evaluated in the presence of a disturbance

(force ripple) both with and without a disturbance observer (DOB). From the description, it appears that the controller without DOB is affected by the force ripple, leading to a tracking error of around 5.795×10^{-3} (per unit). This suggests that the force ripple is causing deviations from the desired trajectory and is affecting the overall performance of the controller. On the other hand, the SMC with DOB appears to be more effective at compensating for the force ripple, resulting in a tracking error of only 0.781×10^{-3}(per unit). This suggests that the DOB can estimate the disturbance accurately and compensate for it effectively, leading to improved tracking performance.

Overall, these results show that the SMC with DOB is a more effective controller for position tracking in the presence of disturbances such as force ripple. However, it is important to note that the effectiveness of the controller will depend on the specific system being controlled and the characteristics of the disturbance being experienced.

Table 4-2 The dynamic performance of the system with SMC for velocity tracking.

Control method	**Steady-State Error (p u)**	**Overshoot (%)**	**Undershoot (%)**	**Rise time (sec)**	**Settling time (sec)**
SMC-with DOB	$\mathbf{0.781 \times 10^{-3}}$	0	0	0.2198	0.3903
SMC-without DOB	$\mathbf{5.795 \times 10^{-3}}$	0	0	0.2200	0.3914

The table displays the features of the step response of the speed for two controllers: Sliding Mode Control with Disturbance Observer (SMC-with DOB) and Sliding Mode Control without Disturbance Observer (SMC-without DOB). The parameters observed in the step response analysis encompass the rise time (duration for the system output to transition from a specified lower value to a specified higher value), settling time (time taken for the system output to stabilize within a specified range around the final value), overshoot (the magnitude by which the system output surpasses the final value before stabilization), and steady-state error (the discrepancy between the final value and the actual output in the long run).

The simulation results proved that the proposed method was able to provide fast response and good control performance with reduced force ripple. Similarly, in order to mitigate the chattering effects. a sliding-mode control with a boundary layer was

presented to cope with chattering and static friction simultaneously. A modified saturation function was used to replace the switching function.

There is no simple method for obtaining SMC parameters. In order to have these parameters found, it is necessary to perform simulations and analyse results to find the best values of the parameters that guarantee the required performance of the system. This process is potentially highly time-consuming requiring multiple attempts. Therefore, parameter selection brings in significant complexity in the process of designing controllers. Hence, soft computing techniques are available to identify the parameter vector [$\delta, \lambda, \ k$] [107]– [109].

The control system design begins with an exploratory phase where parameters are selected through trial and error to minimize tracking error. Subsequently, to enhance the efficiency and effectiveness of the control system, an optimization algorithm is introduced to systematically determine the optimal values for the SMC parameters. This transition from manual tuning to algorithmic optimization is expected to yield improved control system performance.

4.8. Tuning Parameters Control using Bees Algorithm

To address a variety of optimization challenges, several optimization algorithms and techniques have been created. These algorithms may generally be split into two major classes: stochastic algorithms and deterministic algorithms [4]. The majority of common optimization algorithms are deterministic algorithms that depend on the objective function values either directly (direct deterministic or gradient-free algorithms) or indirectly (indirect deterministic or gradient-based algorithms) to determine the optimum. Finding the ideal answer is guaranteed by deterministic algorithms. Methods based on gradients might be thought of as effective means of resolving optimization issues. However, it's possible that an objective function's derivative won't be accessible, won't be accurate, or will take too long to compute. Although employing function values alone is not a practical strategy, free-gradient approaches are derivative-free. Although free-gradient methods are derivative-free, the thorough search involved makes using function values alone an impractical strategy. Every combination of answers must be considered in a thorough search, and the time needed to complete this study is undesirable and could possibly be impossible.

As a result, many scholars began to consider alternative strategies that can find workable answers in an appropriate amount of time and while taking up an appropriate amount of space. Stochastic algorithms are now in use as a result. Stochastic optimization algorithms, by definition, are a category of algorithms distinguished by their utilization of random rules in decision-making processes. Unlike deterministic counterparts, stochastic algorithms introduce an element of randomness to efficiently explore solution spaces. The primary objective is to discover excellent solutions, meaning optimal or high-quality outcomes, in an effective manner. This randomness allows for a more versatile exploration of potential solutions, enhancing the algorithm's ability to find superior results compared to methods that rely solely on deterministic rules [118].

4.9. The Bees Algorithm

The Bees Algorithm is a metaheuristic optimization algorithm inspired by the foraging behaviour of honeybees. It was first proposed by Pham in 2005 [119].

Bees Algorithm (BA) is inspired by the foraging behaviour of honeybees in nature and was designed to search for the best solution to a given optimisation problem. A solution in the search space is thought of as a nectar source. Scout bees randomly sample the solution space and appraise the quality of the visited locations through the fitness function. Foragers are recruited to exploit the most promising (m) locations found by the scout bees. Each scout directs several foragers to the neighbourhood of the solution found. The scouts that found the (e) top-rated locations recruit (nre) foragers, the scouts that found the remaining m-e most promising solutions recruit ($nrb < nre$) foragers. The neighbourhood of a solution is regarded as a ‘flower patch’. Overall, the original BA employs a combination of local exploitative and global exploratory search techniques. For the global search, scout bees are sent to random points of the search space to look for potential solutions. For the local search, foragers are sent to the neighbourhood of the most favourable solutions [120].

The parameters need to be set for the basic algorithm are the number of scout bees (n), the number of patches selected for the local search (m), the number of top-rated patches (elite) in selected patches (e), the number of foragers recruited for the top patches

(nre), the number of foragers to be recruited for the other selected patches (nrb), the initial size of each patch (ngh) and finally the stopping criteria [120].

The algorithm repeats the above steps until a stopping criterion is met, such as a maximum number of iterations or a satisfactory solution is found.

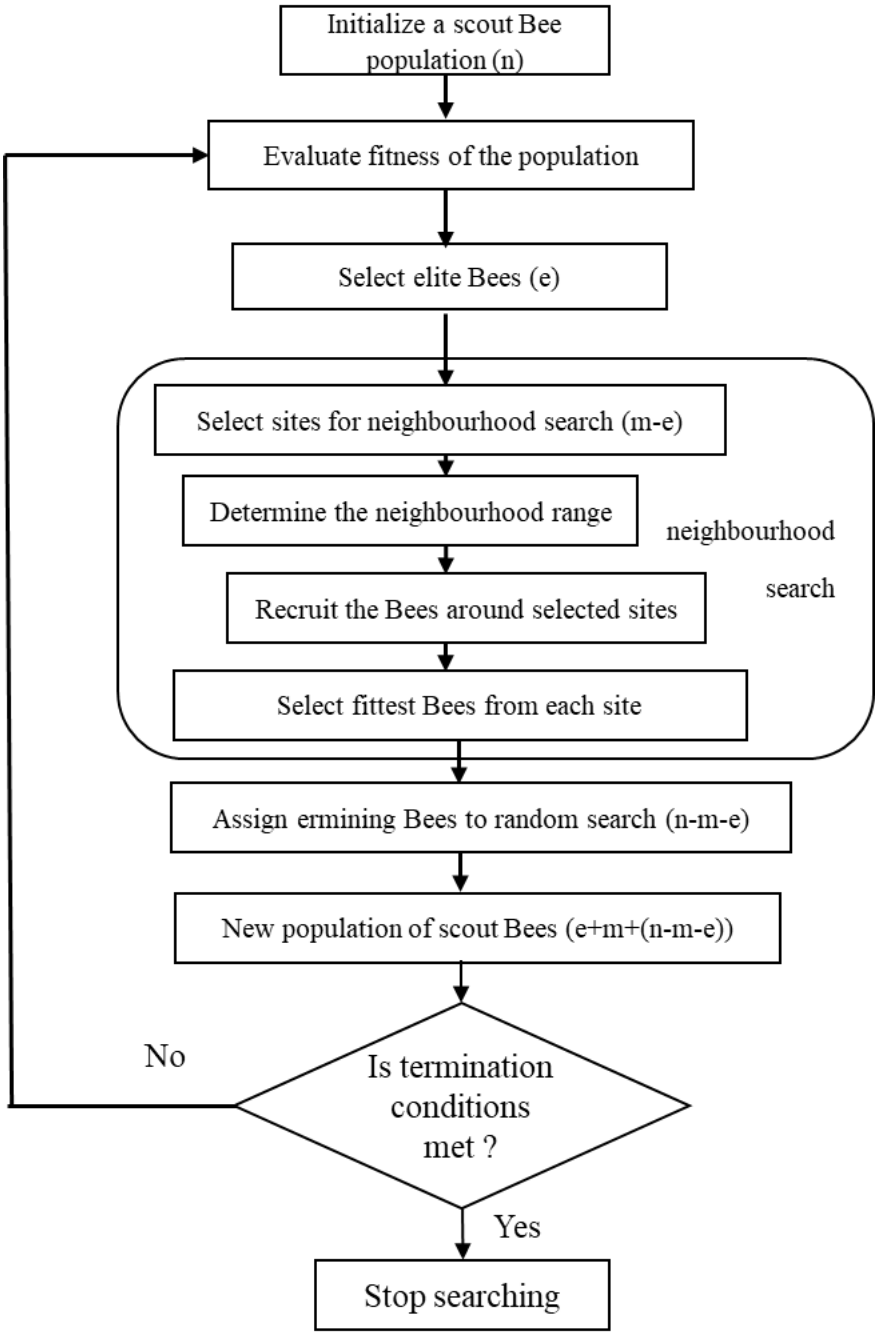

Figure 4.10 The flow chart of the basic Bees Algorithm.

The Bees Algorithm has been shown to be effective in solving various optimization problems, including continuous, discrete, and multi-objective problems. BA has been successfully applied to problems in many fields, such as control engineering [121], [122], manufacturing [123], [124], classification / mining [125], [126], project scheduling problems [127], and many other applications [128]–[137] .

4.9.1. Sliding Mode Control Optimised by the Bees Algorithm

In sliding mode control design, the sliding surface s(t) is a key step to define the desired behaviour of the investigated system. The function of SMC is to always keep the state of the system as close as to this surface. The proposed sliding surface is given in Equation (4.1).

Soft computing techniques can indeed be useful in identifying the parameter vector for the sliding surface in the proposed design. Soft computing encompasses a range of computational methods that can effectively handle uncertainty, imprecision, and force ripple.

The sliding surface of the proposed design has three parameters [δ, λ, k]. The selection of these parameters is critical to the performance of the control system. A well-designed sliding surface can provide fast and accurate control of the system, even in the presence of disturbances or uncertainties. On the other hand, a poorly designed sliding surface can lead to unstable or oscillatory behaviour, which can cause the system to be unstable.

In the realm of modern controller design and for various controlled systems, there exists an inherent challenge in achieving a delicate balance between stable performance and rapid response. While stability is essential for preventing erratic behaviour and ensuring a system settles predictably, the pursuit of a fast response, often necessary for dynamic environments, can introduce the risk of instability or overshooting. Striking an optimal compromise between these conflicting requirements is a central concern in control system engineering, where designers navigate trade-offs to meet the specific demands of each application, aiming to provide both reliability and responsiveness within the constraints of the system at hand. Therefore, a compromise between quick response and excellent stability is considered when designing a controller, which is achievable by adequately selecting an appropriate controller and designing it by minimizing a properly

selected cost/objective function with the aid of an optimization algorithm. The objective function used to tune the controller mainly relies on a performance criterion that considers the overall closed-loop response of the system. Many objective functions have been proposed in the control design, in which several kinds are the most often used for DC linear motors. Because of their better performance compared to the other criteria [117]. The Integral of Square Error (ISE) illustrated in Equation (6.1) is used in this work. Therefore, SMC with DOB controller is designed for the DC linear motor by minimizing the defined objective functions with the help of the Bees Algorithm and other techniques.

$$ISE = \sum_{t=0}^{T}(e(t))^2 \tag{4.40}$$

Where the sampled time is given as t, $e(t)$ represents error signal differentiating the actual and desired values for the parameters targeted for optimisation. The entire running time of the algorithm to optimise the controller gains is given as T. The limit of each parameter is constrained in the range of: [$(0 < k < 1000)$, $(0 < \lambda < 10)$ and $(0 < \delta < 0.9)$]. The parameters of the BA are set in this work as given in Table 6.1.

Table 4-3 The parameters of the BA

Parameter	**Value**
Number of iterations	100
Scout bee population, n	50
Number of best scouts, m	5
Selected elite bees, e	2
Number of bees called to top locations, nep	5
Number of bees called to remaining locations, nsp	3
size of patches, ngh	0.11

The significance of population size in the Bees Algorithm (BA) is evident from prior research, indicating that enlarging the population diminishes the necessary iteration count and heightens the likelihood of success. Nevertheless, this expansion concurrently results in an escalation of function evaluations. Notably, a surplus of elite sites doesn't notably influence performance; thus, a modest number of elite sites, even if minimal, suffices. Typically, the population of scout bees (n) is selected to fall within the range of 30 to 100. In this research, the population of scouts has been chosen to be 50. Other parameters were determined depending on the population number. The number of selected sites (m) was 10% of the population size, and the number of elite sites (e) among those selected was 40% of m.

Neighborhood search holds fundamental importance for evolutionary algorithms. In this research, the shrinking neighborhood approach was employed, systematically reducing the neighborhood size at each iteration. This method enables more refined searches in subsequent iterations by utilizing smaller neighborhood values [127][131]. All these parameters have been chosen depending on the prior research which gives the best results.

4.9.2. The teaching learning-based optimisation

The teaching learning-based optimisation (TLBO) algorithm has been developed from the concept of teaching and learning processes, with teachers influencing outputs from class-based learners. TLBO involves two fundamental learning phases, the first being the ‘teacher phase’, in which learning occurs via the teacher, and the second being the ‘learner phase, which involves learner-learner interactions which inform learning. In TLBO, a learner group forms the population, while the various subjects that a learner can study are equated to the varying design parameters in the optimisation problem, with the outcomes for learners equating to the problem’s fitness value [131]. For the total population, the teacher is considered the optimal solution. Each design variable represents a parameter within the optimisation problem’s objective function, with the optimal solution set as the optimal objective function value [132].

4.10. Simulation results and Discussion.

The bee's algorithm has been used to modify the controller settings repeatedly until the required closed-loop system performance is reached in order to achieve the design objectives for the entire system. Rise time, overshoot, settling time, and steady-state error are all metrics used to describe how well a closed-loop system performs. In general, it is preferred to have a system with a quick ascent, quick settling time, no steady-state error, and nearly no overshoot. So, in this study, the integrated squared error (ISE), settling time, and overshoot is decreased by employing BA to deliver the desired performance.

To compare the results of the performance of the proposed controller, the parameters are tuned also using the Teaching-Learning-Based Optimization (TLBO) algorithm. TLBO is another meta-heuristic optimization algorithm that is effective in solving various optimization problems.

In this case, the proposed control parameters with disturbance observer for the position control are only tuned and tested.

The optimal gains of the proposed SMC design obtained using the proposed BA and TLBO algorithms by minimising ISE objective function are depicted in Table 6.2.

Table 4-4 The SMC optimum parameters obtained by BA and TLBO

Controllers	**Parameters**		
	k	**λ**	**δ**
SMC-BA	953.45	12.26	0.0972
SMC-TLBO	520.59	7.92	0.4538

Table 4.4 shows The SMC optimum parameters obtained by BA and TLBO. These parameters have been tuned by algorithms to achieve an optimal balance between convergence speed and chattering reduction. This strategic choice enhances the step response characteristics of the controlled system.

Figure 6.2 shows the step response of the testbed system based on the proposed SMC-DOB design. Table 6.2 provides the characteristics that summarise the performance of each technique. From Figure 6.2 and Table 6.2, it is obvious that SMC-DOB tuned by BA gives the best response in terms of overshoot and settling time. Increasing the gain of the sliding mode controller (k) enhances its responsiveness to changes in the position behaviour of the motor, leading to a shorter settling time and reduced steady-state error (as shown in the results). However, increasing the gain too much can lead to instability and oscillations in the plant's response. Therefore, the BA algorithm was used to achieve the balance between increasing the gain and the fast response. Also, proper selection of the parameter (δ) in the controller is important for achieving high-precision tracking performance. A smaller value of (δ) can result in better accuracy, but this can also lead to highly discontinuous control inputs, which can be detrimental to the system's performance. Therefore, there is a need to find a trade-off between the desired tracking error and the level of input discontinuity that is acceptable for the specific application. Nonetheless, the proposed control law has the capability to handle unknown system parameters and compensate for factors such as friction and ripple force. It is also observed that the obtained responses are slightly different in regard with settling time, rise time and the steady-state error which is eliminated in all cases. Importantly, a considerable improvement in the performance of the system is achieved using BA.

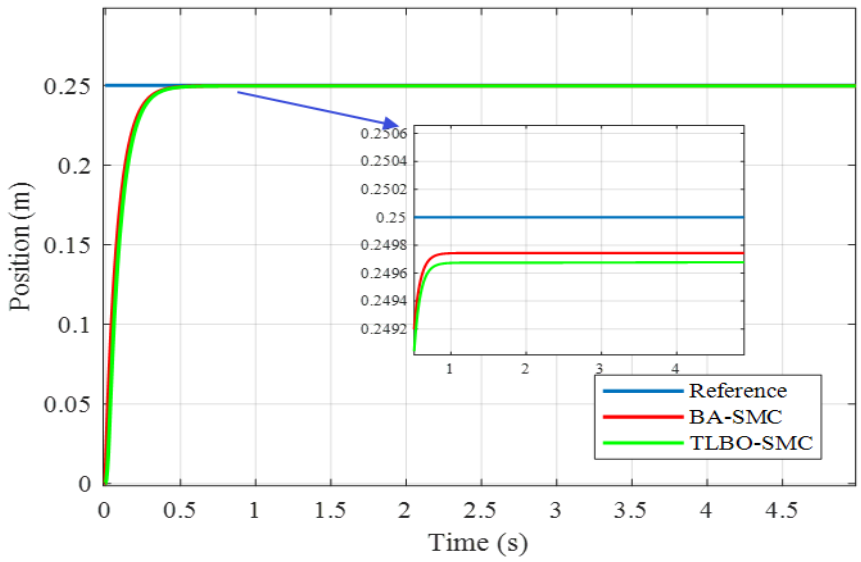

Figure 4.11 Response of position SMC-DOB control tuned by BA and TLBO.

Table 4-5 The dynamic performance of the system with SMC-DOB tuned by different optimization algorithms.

Control method	Steady-State Error (p u)	Overshoot (%)	Undershoot (%)	Rise time (sec)	Settling time (sec)
BA-SMC	$\mathbf{0.102 \times 10^{-3}}$	0	0	0.1831	0.3260
TLBO-SMC	$\mathbf{0.135 \times 10^{-3}}$	0	0	0.1837	0.3400

The table 4.5 and figure 4.11 display the features of the step response of position control using Sliding Mode Control with Disturbance Observer (SMC-with DOB). The algorithms employed to achieve optimal controller parameters for step response analysis include rise time (the duration for the system output to transition from a specified lower value to a specified higher value), settling time (the time taken for the system output to stabilize within a specified range around the final value), overshoot (the magnitude by which the system output surpasses the final value before stabilization), and steady-state error (the discrepancy between the final value and the actual output in the long run.

Based on the information provided in Table 6.3, it seems that BA-SMC has a slightly better steady-state error 0.102×10^{-3} compared to TLBO-SMC 0.135×10^{-3}. Both methods have zero overshoot and undershoot, which means they are stable and have no oscillations. The rise time for both methods is also similar, with BA-SMC being slightly faster at 0.1831 seconds compared to TLBO-SMC at 0.1837 seconds. However, TLBO-SMC has a slightly longer settling time of 0.34 seconds compared to BA-SMC at 0.326 seconds, which means it takes slightly longer for the output to reach and stay within a certain range of the setpoint. Overall, both methods seem to perform relatively well.

The simulation result presented in Figure 6.3 the phase trajectory which clearly shows that the chattering has been reduced in the state plan response.

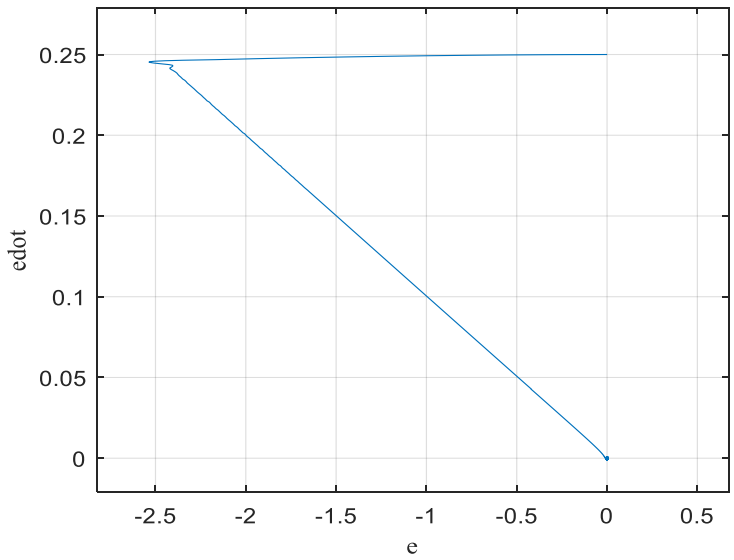

Figure 4.12 Phase trajectory

Compared to Figure 5.6 in last chapter, the chattering phenomenon have successfully reduced by using the replacement of the sign function with the saturation function and optimizing δ using Bee's algorithm. Moreover, as mentioned earlier, a trade-off between system performance and acceptable chattering levels has been made using the algorithm.

The sliding mode surface is converged to zero in finite time as shows in Figure 6.4. And the reaching time is about 0.64s.

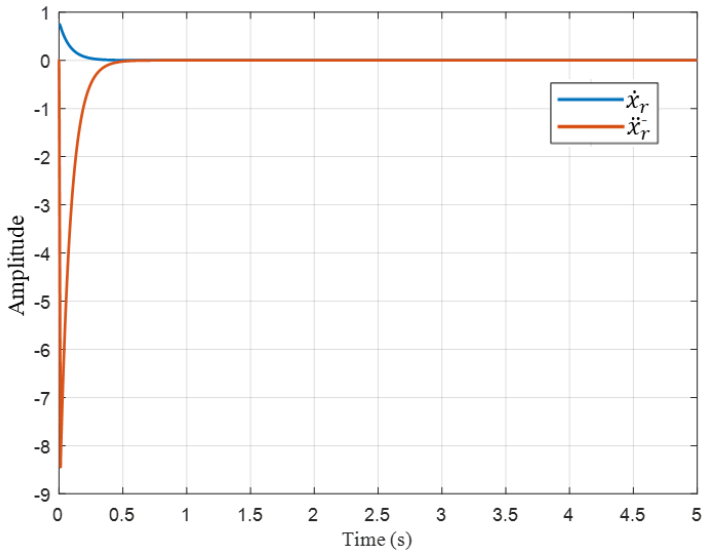

Figure 4.13 System state responses

Convergence characteristics for BA and PSO algorithms with SMC are demonstrated in Figure 6.5. From the figure, it is observed that the Bees Algorithm is slightly better than TLBO.

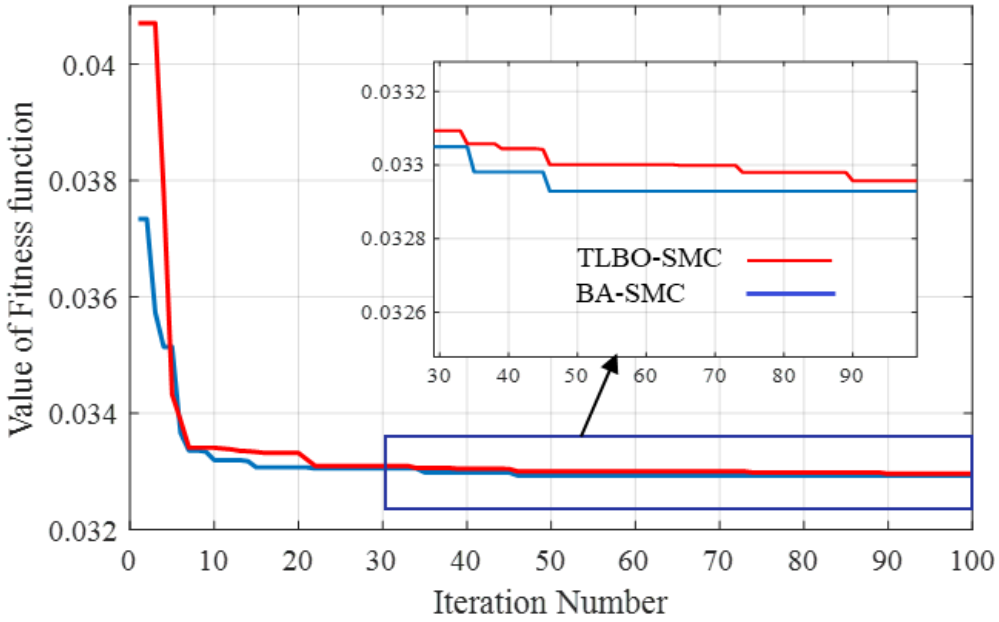

Figure 4.14 Convergence characteristics for BA and TLBO.

In figure 4.14 shows the convergence simulation of the fitness function (integrated squared error), where the BA gets the best result just after 45 iterations, while TLBO in iteration 90

The obtained results show that the best performance was achieved with SMC tuned by BA as it provides the fastest response and Steady-State Error in comparison with SMC optimised by TLBO. Moreover, TLBO has proved to be a successful optimisation tool as SMC tuned by this algorithm has also provided a satisfactory response in terms of settling time and rise time.

Table 4-6 Comparison of the dynamic performance of the system in SMC, SMC-LTBO and SMC-BA

Control method	**Steady-State Error (p u)**	**Percentage (%)**
SMC	0.759×10^{-3}	0
TLBO-SMC	0.135×10^{-3}	82.21%
BA-SMC	$\mathbf{0.102 \times 10^{-3}}$	86.56 %

The table above presents values describing the steady-state error and its percentage for each case: sliding mode without tuning parameters, sliding mode control with tuning parameters using TLBO, and sliding mode control with tuning parameters using BA

Table 6.4 provides a result of the performance of the control strategy with two different algorithms (SMC-DOB tuned by TLBO and SMC-DOB tuned by BA) in terms of tracking error. Both sets of results show a significant improvement in tracking error when compared to the initial tracking error of 0.759×10^{-3}. In the first case (SMC-DOB tuned by TLBO) the maximum tracking error, dropped from 0.759×10^{-3} to 0.135×10^{-3}, with a decrease of almost 82.21%. whereas in the second case (SMC-DOB tuned by BA) the maximum tracking error, dropped from 0.759×10^{-3} to 0.102×10^{-3} , with a decrease of almost 86.56%.

4.11. Summary

The theory of variable structure control has been briefly surveyed in this chapter. Since SMC exhibits many superiorities, it can be preferably expressed to control linear or nonlinear systems with uncertain dynamics. Although robustness can be achieved without the exact knowledge of the control system, the system performance and control quality depend very much on the choice of the sliding parameters and the estimate of bounding functions of the unknown components. In practice, excessive control input and severe control chattering which may excite unmodelled high-frequency dynamics are highly undesired. Therefore, how to capitalize on the SMC's merits to develop more intelligent control techniques for the purpose of improving the performance of the SMC systems or SMC based ones as well as relaxing the constraint on the bound information of the uncertain dynamics has become a demanding topic which will be thoroughly studied in the subsequent chapters. The presence of the force ripple is causes deviations from the desired trajectory when the controller without DOB is used. This indicates that the force ripple is affecting the performance of the controller and reducing its ability to accurately track the desired trajectory. However, the SMC with DOB is able to compensate for the force ripple more effectively. Force ripple, a fluctuation in force affecting system performance, is effectively compensated for by the DOB, which accurately estimates the disturbance and applies corrective measures. This integration

of SMC with DOB results in enhanced tracking performance, allowing the system to more precisely follow desired trajectories despite the presence of disturbances such as force ripple. The paragraph emphasizes the capability of this combined approach to minimize the impact of disturbances, showcasing its potential for improving the overall stability and performance of the control system in the face of external variations.

Sliding Mode Control with disturbance observer (SMC-DOB) was designed and implemented for the control position of the DC linear motor under the force ripple effect. Then the suggested BA was utilised to optimise the parameters of the SMC. A comparison between BA-based SMC and other techniques was conducted. Simulation results evidenced that the proposed BA-based SMC-DOB implemented in the testbed system is robust and improved the proposed control. The simulation results show that the SMC adjusted by BA performs better than SMC optimised by TLBO in terms of response time and steady-state error. Moreover, SMC adjusted using TLBO method has also delivered a suitable response in terms of settling time and rising time, demonstrating the efficacy of TLBO as an optimization technique.

Chapter 5: Experimental Work, Testing, Verification and Validation

5.1. Experimental Setup

In order to perform experimental tests on a brushless DC linear motor, a test setup is required that can accurately measure the performance of the motor under different operating conditions. The test setup typically includes a power supply to provide electrical power to the motor, a load to simulate the application that the motor is intended for and sensors to measure various parameters such as current and position.

The effectiveness of the proposed control scheme can be verified by measuring the performance of the motor under different operating conditions with and without the control scheme implemented. The performance of the motor can be evaluated based on parameters such as speed, thrust, efficiency, and accuracy of motion. By comparing the performance of the motor with and without the control scheme, it can be determined whether the control scheme is effective in improving the performance of the motor.

5.1.1. Force sensor

The load cell RS 632-742 was used to measure the actual force output of the motor. The load cell has a sensitivity of 2 mV and was calibrated with a ratio of 1 mV = 12.5 N, which means that for every 1 mV increase in the output voltage of the load cell, there is a corresponding increase of 12.5 N in applied load.

To determine the actual force output of the motor, the output voltage of the load cell needs to be measured using an appropriate measurement device, such as a digital Multimeter. The output voltage can then be converted into the corresponding force value using the calibration ratio as in Appendix B.

5.1.2. Controller Board

The microcontroller chosen for this project is the "Arduino Mega." It is an affordable and user-friendly microcontroller designed for developing interactive sensor applications. The microcontroller is based on the "Atmel 328" microcontroller chip, which is an 8-bit microcontroller that runs at a clock speed of 16 MHz.

The Arduino Mega has 54 digital input/output (I/O) pins, of which 14 can be used as Pulse Width Modulation (PWM) outputs. PWM is a technique used to simulate an analogue output using a digital signal. The microcontroller also has 16 analog input pins, which can be used to read analog signals from sensors. Additionally, the microcontroller has 4 UARTs (hardware serial ports), which can be used for serial communication with other devices.

The Arduino Mega also includes a 16 MHz crystal oscillator, which provides accurate timing for the microcontroller. Finally, the microcontroller has a USB connection, which can be used to program the microcontroller and communicate with a computer.

5.1.3. Motor Driver Board

The driver board used in this project is Cytron 10A 5-30V Dual Channel DC Motor Driver, which is based on an H-bridge circuit. The H-bridge circuit is a common way to control the direction and speed of a DC motor. The driver board consists of four transistors that are used to control the voltage applied to each winding of the BDCLM. The board is designed to work with PWM commands from the controller board to control the switching of the MOSFETs.

The driver board supplies the DC voltage to the motor windings and allows the motor to move in both directions by reversing the polarity of the motor supply voltage. This is accomplished by controlling the switching of the MOSFETs. The board is capable of handling up to 30 A (peak 10 seconds) of current during start-up and normal operation of the motor.

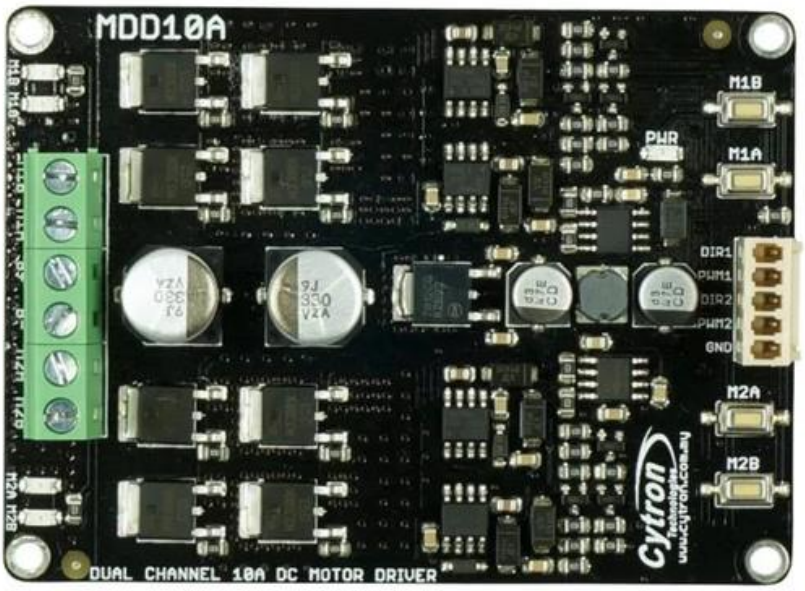

Figure 5.1 Dual Channel DC Motor Driver [135]

The driver motor board has the following features:

H-bridge circuit: The H-bridge circuit allows for control of the direction and speed of the motor.

PWM control: The board can be controlled using PWM commands from the controller board, allowing for precise control of the motor speed.

Dual motor control: The board is designed to control two motors independently, which is useful for applications where multiple motors need to be controlled.

Overcurrent protection: The board has overcurrent protection to prevent damage to the board or the motor in the event of a current overload.

5.1.4. Laser Distance Sensor

Laser Distance Sensors measure over the complete measuring range with an accuracy of +/-1 mm and with a repeatability of 0.3 mm. The measuring range is between 0 and 5 meters. The devices work with a measuring rate up to 250 Hz and have an output rate up to 1 kHz.

Figure 5.2 Laser Distance Sensor

In order to verify the effectiveness of the proposed control scheme, experimental tests have been performed. The experimental set-up consists of a slotless DC linear motor, a laser distance sensor, power supply, an Arduino Mega microcontroller, and a computer. A schematic diagram illustrating the experimental setup is shown in Figure 7.3.

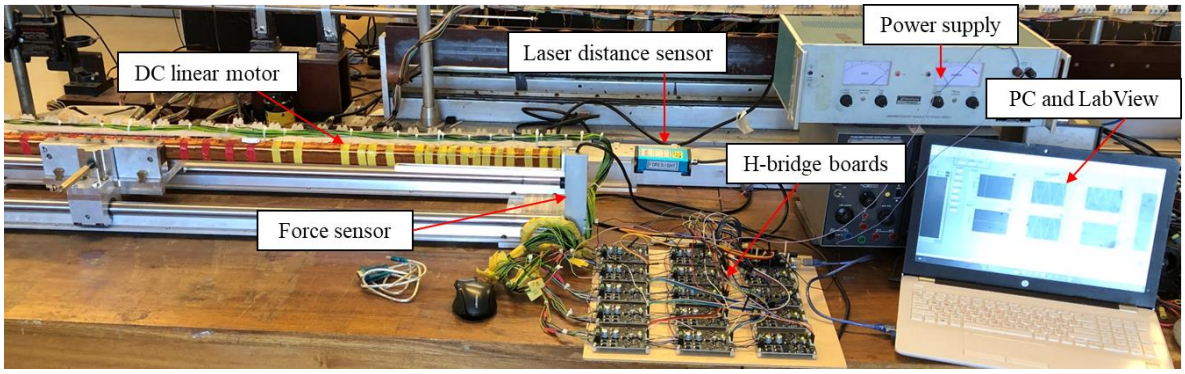

Figure 5.3 The experimental set-up

The controller is developed in LabVIEW. Where the SMC-DOB has been designed via LabVIEW math script module. The position and velocity constraints are applied, and the algorithm is developed in step function. The current applied to the armature winding was around 5 A for the coils in the position control.

In the DC linear machine drive the power-switching H-bridge circuit acts as an electronic commutator, which switches the DC between the windings according to the instantaneous mover position. The commutation strategy is described as the switching

sequence of driver voltage across the armature winding section, which is necessary to ensure the continuous motion of the slider. The commutation was arranged such that only the coils under the influence of the field at a given moment were carrying current.

The main goal of the commutation is to produce maximum thrust and a continuous motion. For the force to be produced on the slider continuously, the armature sections just under the magnets must be energised, but other sections should not be energised in order to avoid a reversal force from acting on the moving carriage, thereby causing a brake that decreases the motor speed.

For closed-loop position control, the laser distance sensor was implemented via LabVIEW using the VISA function which can read the specified number of bytes from the position sensor and return the data in the read buffer.

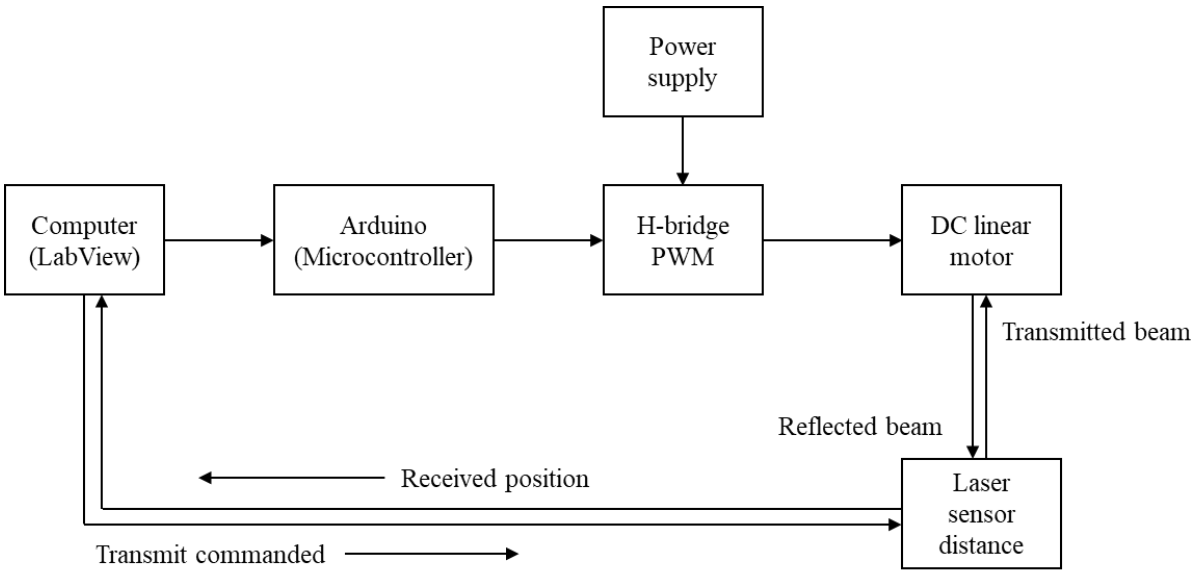

Figure 5.4 A schematic diagram of the experimental set-up

The experimental set-up, depicted in Figure 7.2, consists of a schematic diagram. The control process initiates from the computer, utilizing the LabVIEW program. Initially, the desired position to control or access is determined by the control system. Subsequently, the position of the mover is detected using a laser sensor, which is processed through the LabVIEW program. Based on the mover's position, the controller

facilitates the commutation of the armature winding via an Arduino board. The Arduino then generates voltage signals directed to the H-bridge driver board. This driver board supplies current to the coils, resulting in a force exerted on the permanent magnets within the mover, leading to its movement.

Before activating the motor, the Laser sensor distance accurately measures the motor's position. Based on this position, the microcontroller transmits a control signal to the H-bridge motor drivers, enabling the energization of the armature windings for continuous movement. Each time the mover moves, three armature windings are energized (as indicated in the table 7.1). The motor is controlled to move forward until it reaches a predetermined travel distance.

Once the mover reaches the correct position, the motor automatically stops.

Table 5-1 Armature winding energising algorithm at armature current 3 A.

Position(mm)	**W 1**	**W 2**	**W 3**	**W 4**	**W 5**	**W 6**	**W 7**	**W 8**	**W 9**	**W 10**	**W 11**	**W 12**
0	+	-		+								
06	+	-		+								
12	+		-	+								
18	+		-	+								
24	+		-	+								
30		+	-	+								
36		+	-	+								
42		+	-		+							
48		+	-		+							
54		+		-	+							
60		+		-	+							
66		+		-	+							
72			+	-	+							
78			+	-	+							
84			+	-		+						
90			+	-		+						
96			+			+						
102			+		-	+						
108			+		-	+						
114				+	-	+						
120				+	-	+						
126				+	-		+					
132				+	-		+					
138				+	-		+					
144				+		-	+					
150				+		-	+					
156					+	-	+					

162					+	-	+					
168					+	-		+				
174					+	-		+				
180					+	-		+				
186					+		-	+				
192					+		-	+				
198						+	-	+				
204						+	-	+				
210						+	-		+			
216						+	-		+			
222						+	-		+			
228						+		-	+			
234						+		-	+			
240							+	-	+			
246							+	-	+			
252							+	-		+		
258							+	-		+		
264							+	-		+		
270							+		-	+		
276							+		-	+		
282								+	-	+		
294								+	-	+		

5.2. Mechanical design

The mechanical design of the linear motor requires careful analysis of the specifications, that is the material, dimension, and size. The principal objective was to achieve a high thrust, reduce force ripple and an accurate positioning of the mover. Furthermore, due to its topology, it can be used as a brushless linear stepping motor. The main physical constraints originate from the permanent magnets, mild steel used for the armature core and the copper windings.

The top and side view of the linear DC motor model prototype is presented as shown in Figure 3.4. The motor is designed to be a double side (U sharp) moving permanent magnet. The field system was mounted inside the carriage, and it was installed on aluminium rails with linear bearings parallel to the armature length to guide its movement. In this model, the air gap is designed to be adjustable to study the effect of the change in the air gap on the thrust of the motor.

From the motor setup shown in Figure 3.4, it can be observed that there are two sources of magnetic field, which are the permanent magnet which provides the main magnetic

flux, and the armature windings which carries the DC current. When the position of the moving magnet unit is detected by laser position sensor, the driver circuits of the related armature coils directly under the magnets, turns on and the current flows into the armature coils. Then, the moving magnet unit moves according to Fleming's left-hand rule. The direction of the armature current is dependent on the polarity of the moving magnet. Although the stator of the DC linear motor consists of Twenty-eight armature coils, only three coils facing the moving magnet are in the on-state in order to provide a smooth movement.

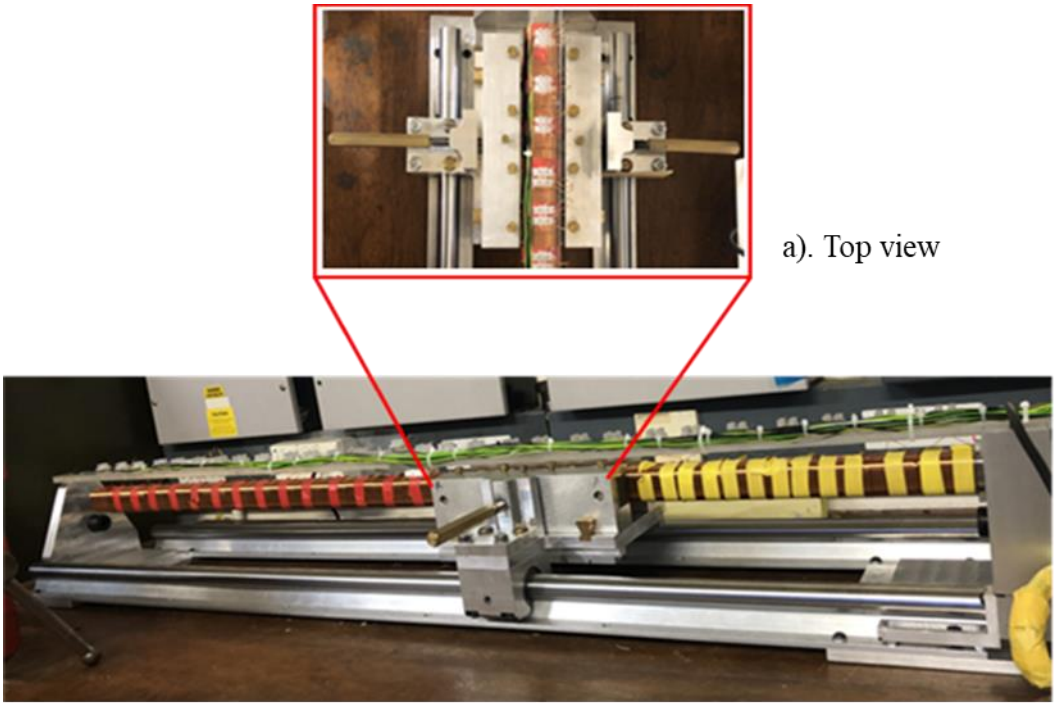

Figure 5.5 The proposed linear DC motor, a) top view, b) side view.

The mover component was a permanent magnet installed inside the carriage that represented the field system. Figure 3.5 depicts the simulation and real-time setup of a permanent magnet moving unit, where this design ensures a seamless motion when switching the energise of the coils.

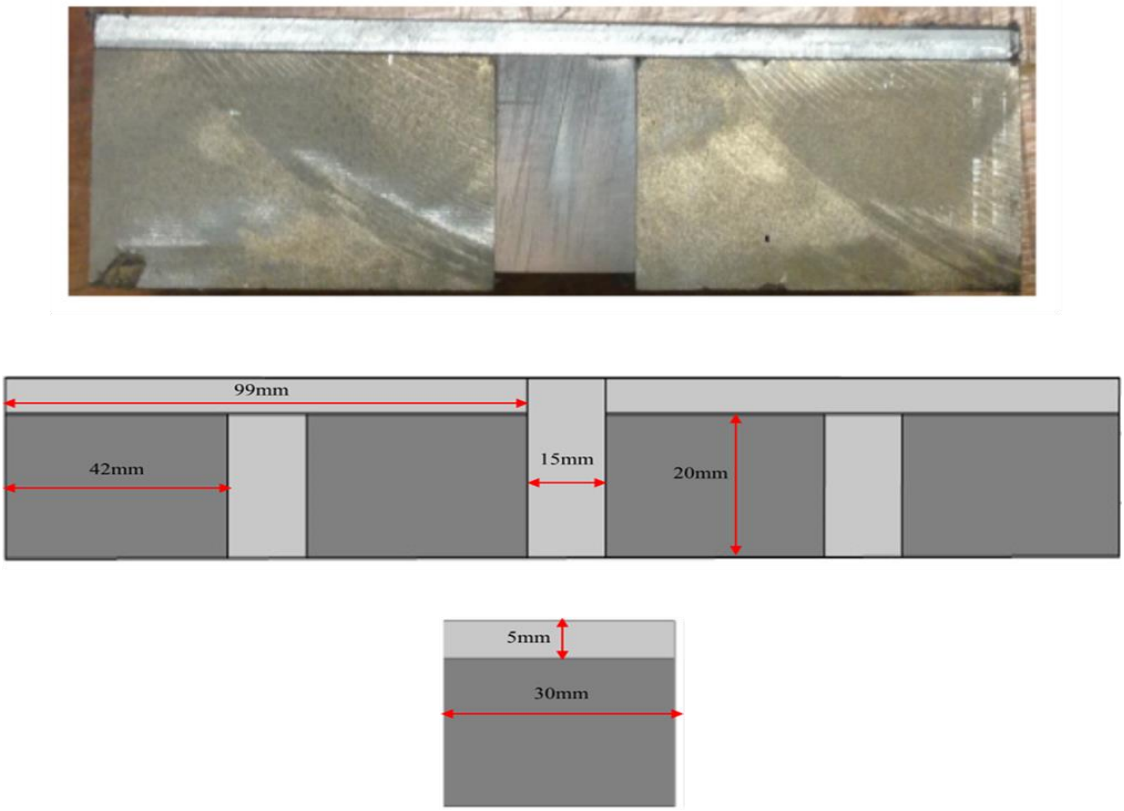

Figure 5.6 Configuration of permanent magnet moving unit Simulink and real time.

The armature windings were designed while taking the power of the motor, the current carrying capability of the armature windings and the track length into consideration. The armature core was designed with a 1.2-metre-long mild steel bar with a cross-sectional area of 25 mm x 25 mm, which determines the travelling distance of the motor.

5.2.1. Coil arrangement

The armature windings that were distributed along the armature core are shown in Figure 3.6. On the armature core, twenty-eight separate multi-layer coil sections are spaced out evenly and made of enamelled copper wire that is 0.5 mm in diameter, or the same size as 24 AWG wire. This permits a maximum DC of 29 A to flow. Additionally, the armature windings are electrically separate from one another.

The smaller the diameter of the wire, the greater the number of turns per-metre length for a given length of armature winding section, hence, the greater the force produced and the less the current carrying capability of the wire. Therefore, using 24 AWG

enamelled copper wire, a compromise was made between the force produced and the maximum current that can pass through the windings without causing any damage.
The ends of the copper wires terminate at the connector blocks which were fixed to a rail directly above the armature and connected to the power supply through switching circuits. The current density in the armature winding was relatively high. However, there was no need to cool the armature winding since it was subjected to a large current for a short period.

The armature winding was wound around the core with dimensions of 30 mm x 30 mm x 42 mm. Each coil section had 670 turns and was fed with a DC. Commutation is achieved by energizing the armature sections in a sequence with the aid of a microcontroller.

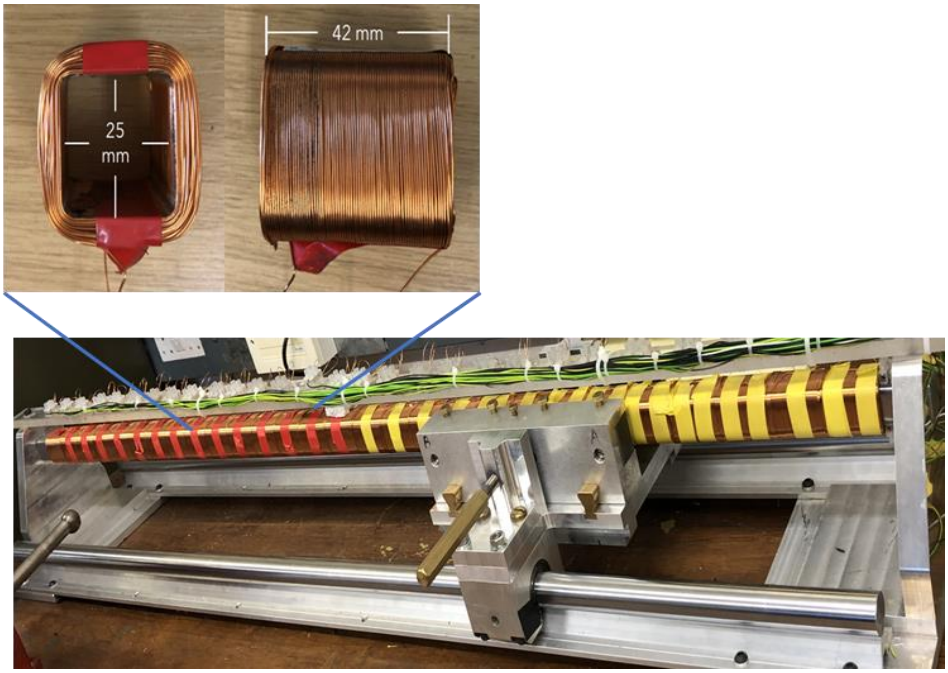

Figure 5.7 Configuration of the winding.

A linear movement occurs when the armature windings located under the permanent magnets are properly fed with currents. A magnetic thrust force will be created on the mover and hence, the latter moves accordingly. The developed thrust depends on the air-gap magnetic flux density which is produced by the permanent magnet and the

current density vector in the armature windings.

5.3. Simulation and experimental results

A prototype of the linear motor presented in Figure 3.2 was constructed and it helped to validate the analytical model by means of measurement of thrust forces. A test rig was designed for the experimental part of the study. Measurements of forces under static conditions were taken using a load cell (force sensor). The output voltage of the load cell is linearly proportional to the applied load and was calibrated with (1 mV = 12.51 N). The sensitivity of the load cell is 2 mV. Figure 5.8 presents the testing apparatus for the measurement of thrust force. During the tests, only three coils located under permanent magnets with normal magnetization were fed by current.

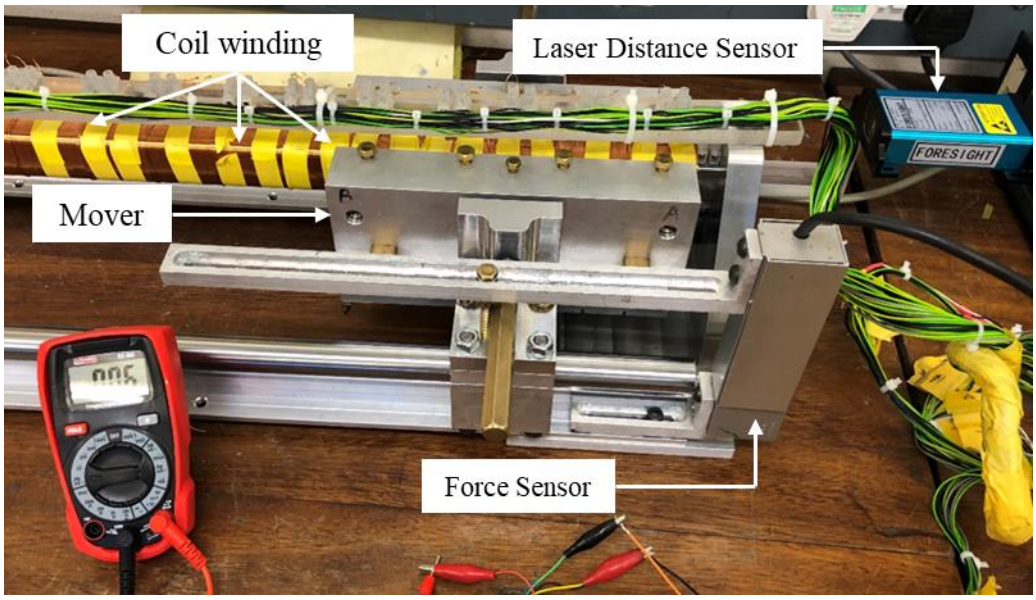

Figure 5.8 Measurement of static thrust

Magnetic flux is considered one of the most important parameters in analysing the performance of any electrical machine. The distribution of the magnetic flux density throughout the entire cross-section of the motor and the surrounding air space is illustrated in Figure 5.9 and the lines represent the flux direction. The magnetic flux was mostly concentrated at the back iron with a value of 2.5 T and about 1.07 T in the armature core.

A plot of the computed magnetic vector potential distribution throughout the cross-section of the motor and airspace is illustrated in Figure 5.9. As can be observed, there are three leakage field components from the moving unit. These are the leakage field from the edges of the moving unit, the leakage field across the inter-polar space separating the opposite magnet, and the leakage field from the yoke. However, the region between the two opposite magnets produces the highest leakage flux.

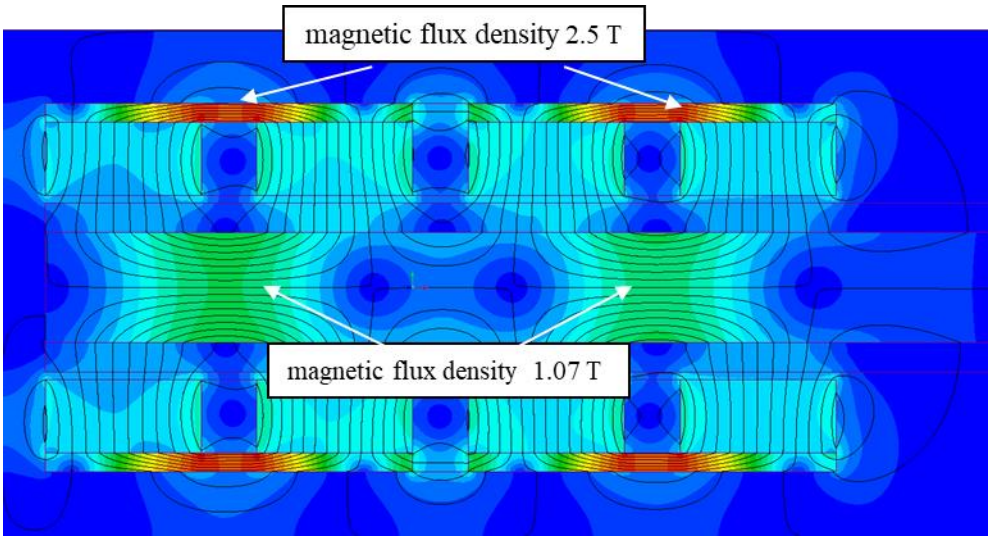

Figure 5.9 Magnetic vector potential distribution throughout the cross-section of the motor

Figure 5.10 presents the graphs of the y-component of the magnetic flux density vector in the air gap. between the armature winding and the magnet. In the region of the coils, the distribution of the y-component of the magnetic flux density vector presented a shape very close to a sinusoidal behaviour. As can be seen from figure 5.10, the peak radial flux density in the airgap occurs in the area opposite the centre of the magnet. Whereas radial flux density becomes almost zero in the area opposite the space between the two magnets.

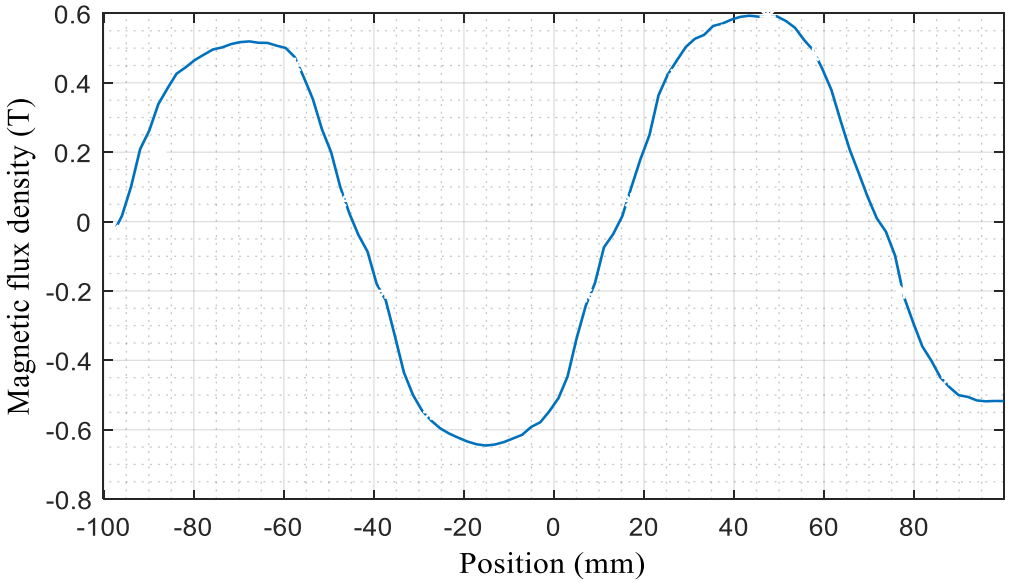

Figure 5.10 Flux density in airgap

For comparison and validation of the simulation model, results are obtained by measurements, under the same conditions of current and position used in the analytical method. The measured values were obtained by means of a gaussmeter “LakeShore 480”. The behaviour of the magnetic flux density presents a sinusoidal shape. The results of the magnetic flux density vector, as shown in figure 5.11, demonstrate that the difference between the simulated and observed peak values is 7.14 %.

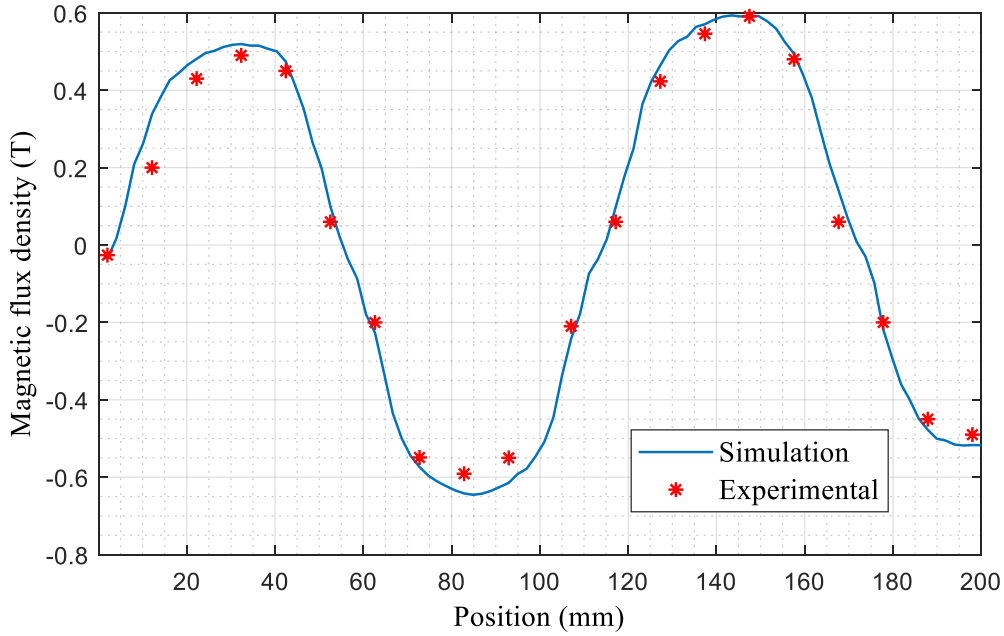

Figure 5.11 Measurement and simulate results of the flux density T.

Figure 5.12 shows a comparison between the experimental and computed static thrust as the armature current is varied. There is a percentage error between the slopes of the simulated and measured values of the static thrust. This is due to the leakage field, frictional force and the normal force produced by the unbalanced force of attraction between the magnetic poles and armature core on either side of the motor.

The results indicate that the measured and computed results are in good agreement and that the static thrust is proportional to the exciting current. Based on the results obtained, the maximum deviation between the computed and measured data is 8.07%. Hence, one can conclude that there is a reasonable agreement between the computed and measured results.

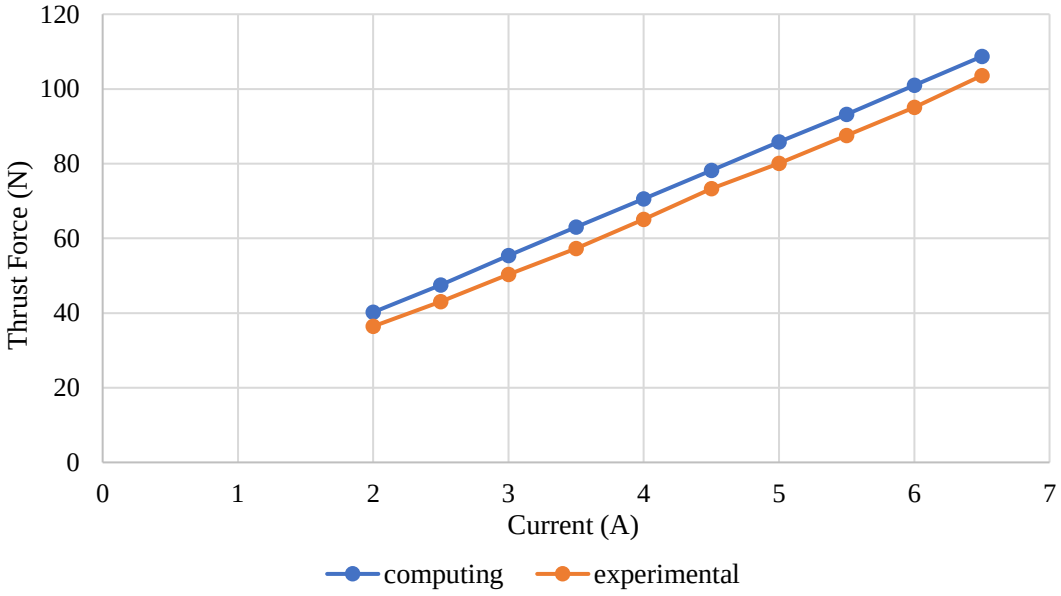

Figure 5.12 Comparison between the experimental and computed static thrusts.

The present study also helped to analyse the behaviour of the developed thrust of the motor as a function of the air gap length. Figure 5.13 shows the graph of the thrust force with different values of air-gap length, when the current in the coil located under the permanent magnets with normal magnetization is 6 A in total.

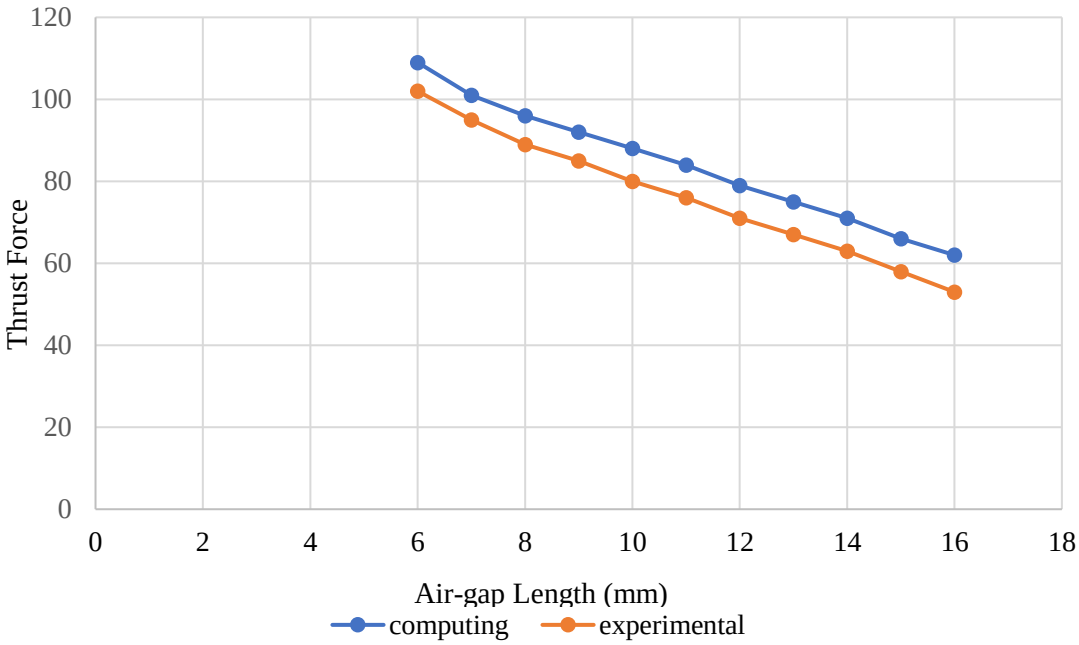

Figure 5.13 Thrust force with different values of airgap lengths.

It can be observed that the thrust decreases with increasing air gap because of the mechanical restriction guidance of the moving unit a minimum air gap of 6 mm was chosen for this model which represents the mechanical clearance between the armature winding and the moving magnets. Figure 5.13 thrust force presented a nonlinear behaviour with respect of the variation of the airgap length. The developed thrust difference between the simulated and measured values is 5.02 %.

5.4. Position control

The experimental results with tuning the parameters of the proposed controller are shown in Figure 5.14, and Table 5.2. The system is controlled using a feedback loop, where the reference position was set to be 250 mm, and then compared with the actual position to track the error.

Different experimental tests are performed using different reference positions (250 mm, 445 mm, and 650 mm), and the average accuracy of the position error is found to be 0.752 mm.

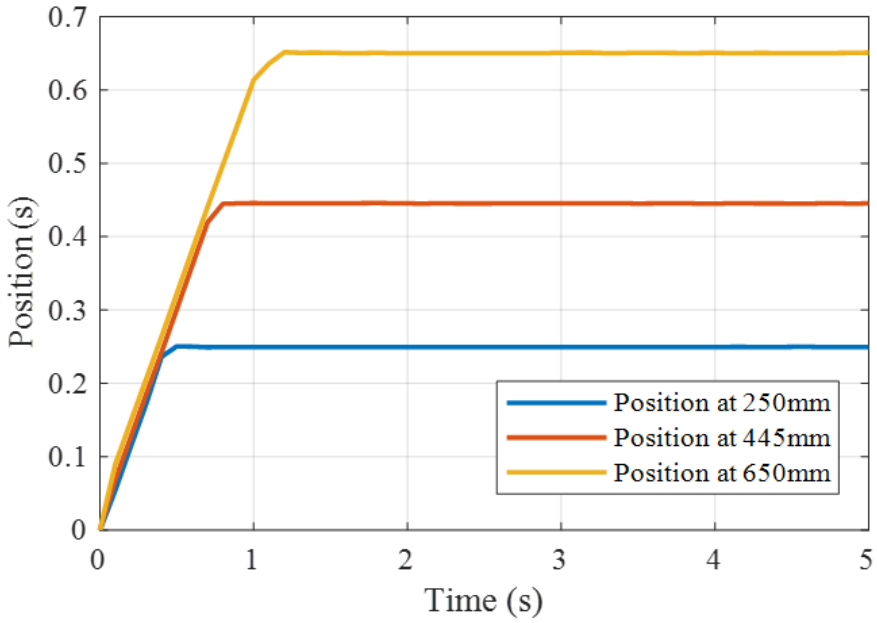

Figure 5.14 Different position control (m)

In Figure 7.5, a different position of the motor is controlled, therefore the reference positions have been chosen to be 250mm, 440mm, and 650mm. A reference 250 mm was taken to analyse the dynamic performance of the system and compare it with the simulation.

With the same tuned control parameters and conditions that were applied in the simulation, it can be noted that the proposed controller gives a good performance with a small steady-state error of around 0.752mm (2.98 %) as seen in Table 5.2. With comparing the simulation in Figure 4.11 and Table 4.5, there is a difference in the tracking performance, where the difference was around 13.6%.

The error in the position of the experimental test was 0.752 mm, and the error in the simulation was 0.102 mm. The rise and stilling time were found 0.403s and 0.519s respectively, while in the simulation were 0.1831s and 0.3260s.

Table 5-2 The experimental dynamic performance of the system with SMC-DOB

Control method	**Steady-State Error (mm)**	**Overshoot (%)**	**Undershoot (%)**	**Rise time (sec)**	**Settling time (sec)**
BA-SMC	**0.754**	0	0	0.403	0.519

Figure 5.15 shows the tracking error of the real position control of DC linear motor by applying the proposed control via LabVIEW.

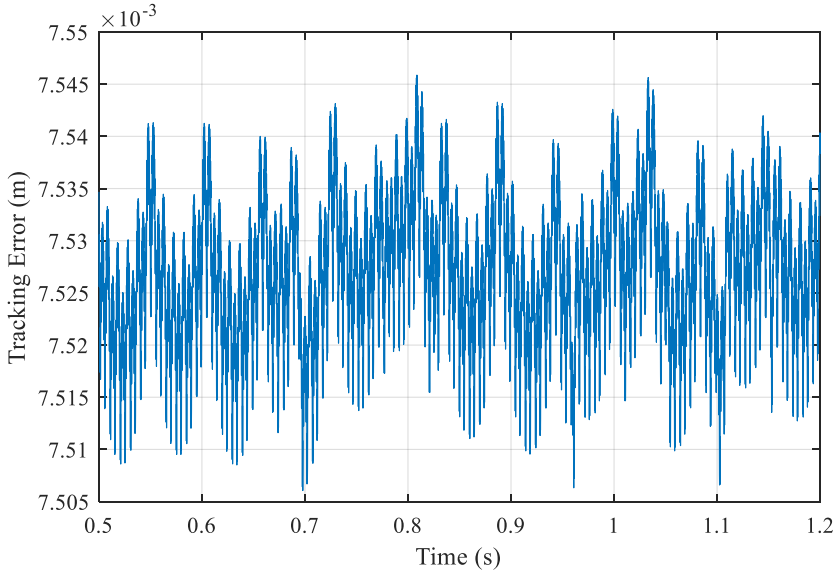

Figure 5.15 The tracking error

The average error is around 0.752mm with a very small ripple. Which means the controller gives a good agreement between the experimental and simulation results.

Robustness analysis of the controller is carried out by load variation of the DC linear motor. Where a load of 10 kg was added to the mover for more tests of the robustness of the control strategy. Figure 5.16 and Table 5.3 show the obtained results from the experiment. As can be seen from Figure 5.16, there is an overshoot due to a load increase.

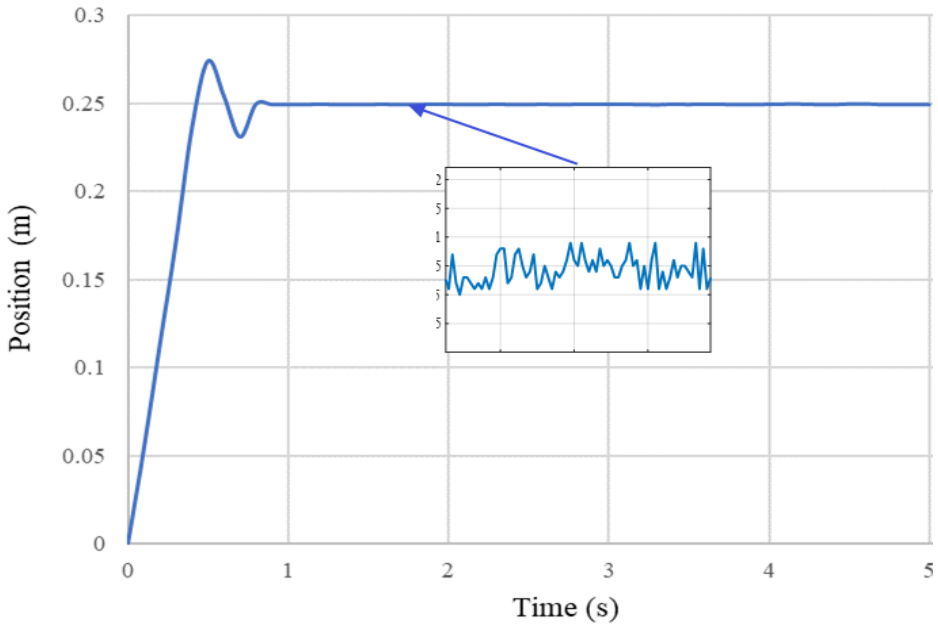

Figure 5.16 Control position with 10 kg payload

The step response of the position control, with a 10 kg increase in load, is shown in Figure 5.16. The step reference is adjusted to 0.25 m. As seen in the figure, the increase in load has an effect on the position of the mover, resulting in a slight overshoot.

The percentage of overshoot and settling time of control setpoint is presented in Table 5.3, the increasing of the load caused an overshoot of the position by 7.5% and undershoot by 2.935 %. However, after 0.8 second the system became stable with small steady-state error around 1mm. The rise time and settling time are similar compared with the performance of the system without force load in Table 5.1.

5-3 The experimental dynamic performance of the system with 10-kg force load.

Steady-State Error (mm)	**Overshoot (%)**	**Undershoot (%)**	**Rise time (sec)**	**Settling time (sec)**
0.947	7.54	2.984	0.430	0.821

The table presents the parameters observed in the step response analysis of position control with external disturbance (mover load 10 Kg) which include the rise time, settling time, overshoot, and steady-state error.

Form the Figure 5.16 and Table 5.3, it can conclude that, although the load is applied, the result of the proposed control shows that, only a slight increase in the overshoot of the system response. However, the output response is still within acceptable limit.

5.5. Speed control

In the experimental studies, the speed control of a DC linear motor using SMC and DOB controller have been employed. The experiment result was presented in Figure 5.17, which showed that the system was stabilized with a slightly ripple. The setpoint for velocity was set to 0.25 m/s, and the system response did not exhibit any overshoot or undershoot.

The rising time was 0.235 seconds, which is the time taken by the system response to reach 90% of the steady-state value from the initial value. The settling time was 0.379 seconds, the SMC and DOB controllers were effective in stabilizing the system and achieving the desired speed control of the DC linear motor, with some minor ripple in the system response.

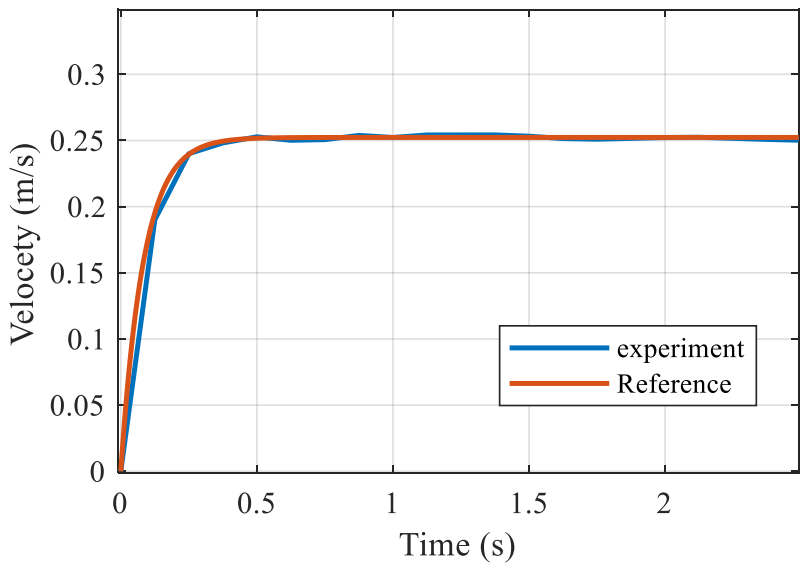

Figure 5.17 The experimental velocity measurement

Real time and simulation of the velocity control of the slotless dc linear motor is shows in figure 5.17, where the effect of the ripple has been reduced.

Figure 5.18 shows that, the effect of increasing the current on speed of the DC linear motor.

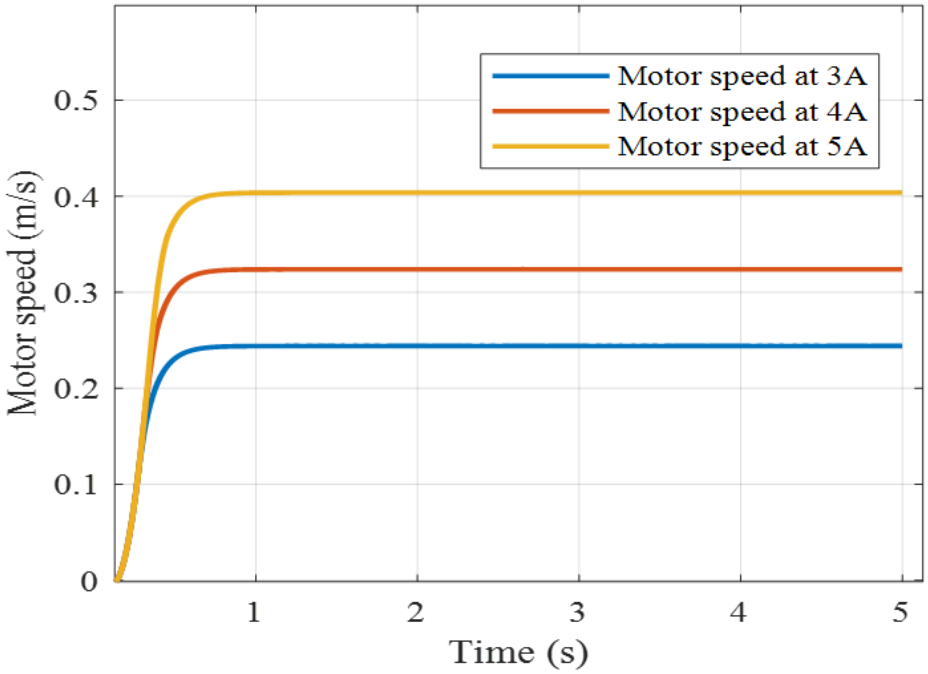

Figure 5.18 Velocity at different current level

Table 5-4 Different speed when apply different armature current.

Armature current (A)	**Speed (m/sec)**
3	0.25
4	0.33
5	0.41

The most significant contribution of this thesis is the creation of a control approach to decrease force ripple and preserve the position of a DC linear motor in the presence of this disturbance. The objective of the control approach is to increase the motor's performance by decreasing force ripple using control methods.

To evaluate the effectiveness of the proposed control method, the current of the DC linear motor was measured in three different cases. The first case involved an open-loop

system where there was no control applied to the motor. As it can be seen in Figure 5.19 that there is ripple of the total current due to static friction and ripple force. also due to asynchronization in switching polarities between coils and energise at the specified time. In the figure, the x axis presents the time (s) and y axis present the current (A).

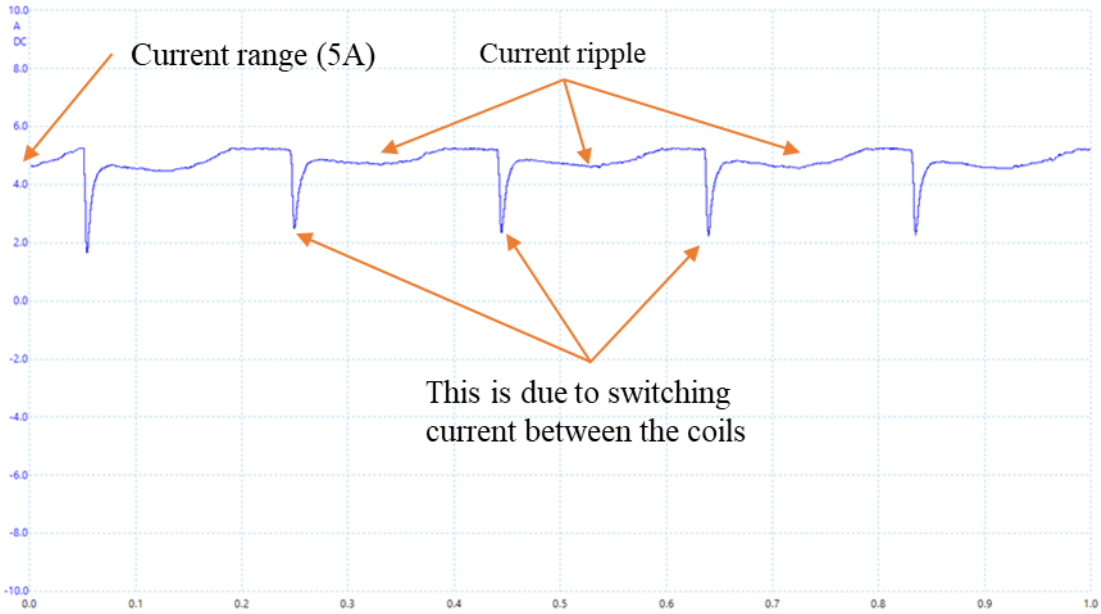

Figure 5.19 The current measured in open loop

The second case involved a closed-loop system without disturbance observer (DOB) and tuning parameters for the controller. It can be seen that, the ripple is reduced compared with first case. Figure 5.20 show the measured current of the linear motor. Where the x axis presents the time (s) and y axis present the current (A).

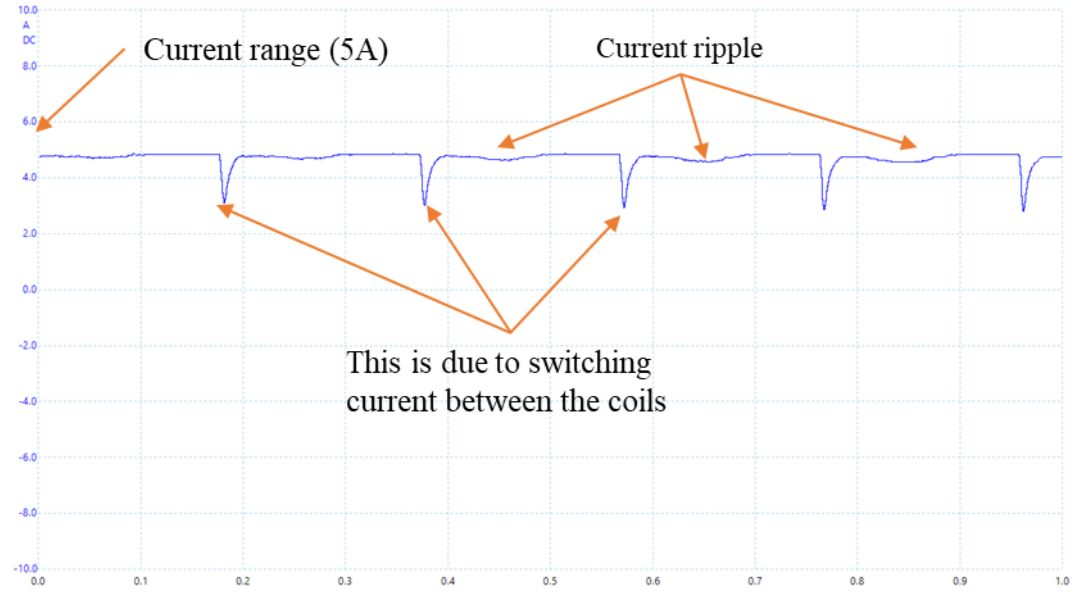

Figure 5.20 The current measured in controlled close loop

The third case involved a closed-loop system with DOB and tuned parameters of the sliding mode controller (SMC) by BA. From Figure 5.21 it can be concluded that, the proposed controller with DOB and tuned parameters are reducing of the force ripple.

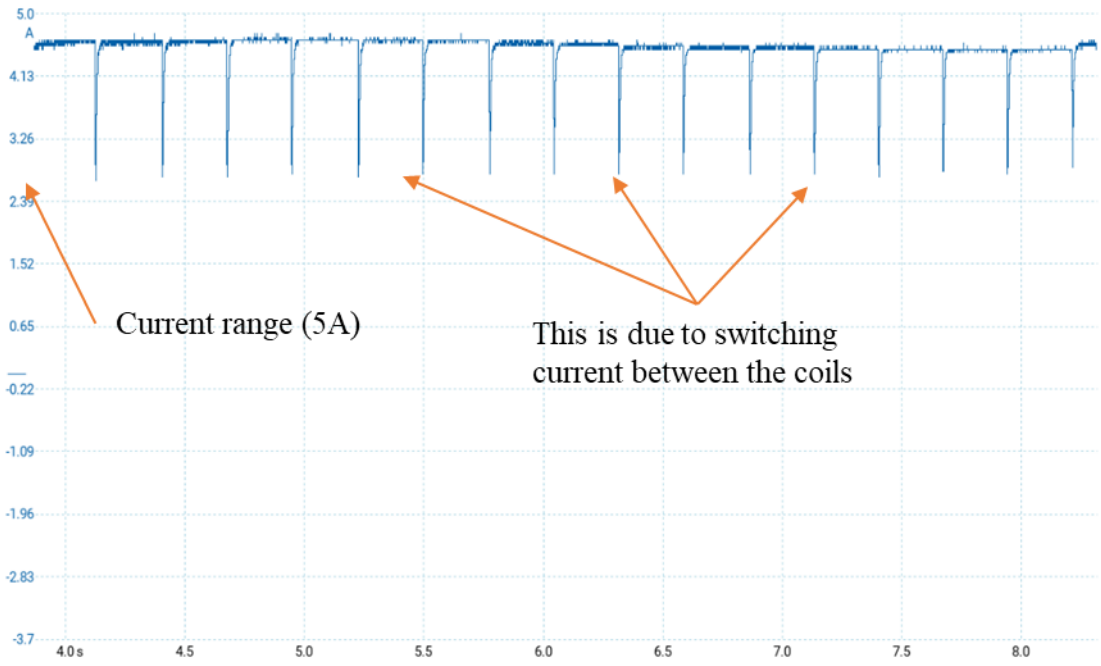

Figure 5.21 the current measured with SMC-DOB tuned by BA.

The results of the study showed that the proposed control method was effective in reducing force ripple and maintaining the position of the motor under disturbance. The closed-loop system with DOB and tuned SMC parameters performed better than the open-loop system and the closed-loop system without DOB and tuning parameters for the controller.

Overall, the study demonstrates the importance of control methods in improving the performance of DC linear motors and highlights the effectiveness of the proposed control method in reducing force ripple and maintaining motor position.

5.6. Summary

In this chapter, a Finite Element Method (FEM) study utilising "MagNet" was employed to modelling and construct a linear DC motor. The thrust force, air-gap flux density, and static thrust force at various airgaps were compared in simulation and real time. The result showed that the magnetic flux density presents a sinusoidal shape in both the simulation and measurement, where peak values of the error was around 7.14%. Also, a comparison was made for thrust force as the armature current has different value, where the results show that the different between the experimental and computed of peak values was 8.07%. The error was 5.02 % between the measured and simulated when the thrust force was measured at the different air gap lengths. This error is due to the leakage field, frictional force and the normal force produced by the unbalanced force of attraction between the magnetic poles and armature core on either side of the motor. It is important to note that different control methods have their advantages and limitations, and the choice of a control method depends on the specific application requirements and constraints. In the case of the experiments mentioned, the tuned SMC-DOB controller by BA was found to be effective in handling the force ripple and balancing the trade-off between acceptable chattering levels and performance. For example, PID controllers are widely used due to their simplicity and ease of implementation, but the design process can be challenging as stability needs to be carefully considered. Feed-forward compensation can also be a useful method to

achieve high performance, but it may only be suitable for repetitive motions and may not be able to handle various trajectories.

Overall, the choice of control method depends on the specific application requirements and constraints, and a balance needs to be achieved between effort and performance. The experiments mentioned in this chapter illustrate the effectiveness of the tuned SMC-DOB controller in handling force ripple.

Chapter 6: Conclusion, Major Findings, Recommendations and Future Work

6.1. Conclusions and major findings

In this research programme, the slotless DC linear motor has been modelled and designed using “MagNet” software to analyse the electromagnetic and mechanical behaviour of the motor, where the results showed that the difference between the practical and simulated is 7.14% of the flux density in air-gap and 8.07% of the thrust force. Also, sliding mode control has been designed to achieve the desired system performance, such as reducing the force ripple of the linear DC motor. Once the system's trajectory is on the sliding surface, the sliding mode control law is used to ensure that the system remains on the surface despite any disturbances or uncertainties.

The disturbance observer has been used in conjunction with the SMC technique to estimate and compensate for the external disturbances and uncertainties that may affect the system's performance. The DOB estimates the unknown disturbances based on the difference between the measured output and the estimated output of the system. The estimated disturbance is then used to update the control input to compensate for the effect of the disturbances.

The “LuGre” dynamic friction model has been investigating both the static and dynamic friction phenomena, such as the presiding displacement that is the prevailing friction phenomenon for high precision applications. Force ripple is also incorporated into the comprehensive model to examine its effect in smoothing the position and the velocity output.

The combination of SMC and DOB provides a robust and reliable control system that effectively reduces the force ripple of the slotless DC linear motor. By using this approach, the tracking error can be minimized, and the system's performance can be improved. The results that have been provided in this thesis, the SMC-DOB tuned by TLBO and SMC-DOB tuned by BA were both effective in reducing the maximum

tracking error, with BA showing slightly better performance in terms of the percentage decrease in tracking error.

6.2. Recommendations and Future Work

Many methods have been documented for reducing force ripple generation, however, the most efficient method ultimately relies on the constraints of the application and the controller used. Fuzzy control, adaptive control, and neural networks are all examples of control methods. The signals that must be processed to verify the chosen topology and the system's inputs and outputs determine the complexity of the methodologies used to design and test the system. While deciding on the best approach and necessary hardware, complications arise from the need to modify or add to existing hardware. During the modelling, several approaches have been used. Unfortunately, the implementation phase of the case is quite delicate. Therefore, it is necessary to consider a broader range of criteria while deciding on the best approach. When high-performance controllers, including digital signal controllers and digital signal processors, are needed to execute a control, it's important to consider the associated costs.

This study may be expanded in the following ways in future studies:

1. The strength of the permanent magnet and the length of the armature core can cause the motor to stop by attracting the motor core, resulting in bending. To prevent this, the air gap should be at least 5 mm, or the shape of the metal core should be changed to a rectangle, with its small face opposite the magnet.

2. A frictional suspension can be used as a feed-forward to improve the accuracy of the controller. The friction parameters can be optimized for better results using BA and another algorithm.

3. Implementing state-space-based control algorithms requires a velocity signal, but when a velocity sensor is not available, a calibration can be used to calculate the speed from the position sensor signal. However, there is a delay between the sensor and the computer, which can result in an error. Therefore, sensor-less process monitoring can be employed to address this issue.

References

[1] WEG S.A, ‘Specification Guide Electric Motors’, 2018. https://static2.weg.net/medias/downloadcenter/ha0/h5f/WEG-motors-specification-of-electric-motors-50039409-brochure-english-web.pdf

[2] T. D. Cox, ‘Development of Novel Linear Drive Machines’, Doctoral dissertation University of Bath, 2008.

[3] S. N. Huang, K. K. Tan, and T. H. Lee, ‘Adaptive Precis ion Control of Permanent Magnet Linear Motors’, *Asian J. Control*, vol. 4, no. 2, pp. 193–198, Jun. 2002, doi: 10.1111/j.1934-6093.2002.tb00345.x.

[4] M. Salman, ‘Analysis, design and control aspects of linear machines using co-simulation’, KTH Royal Institute of Technology, Sweden, 2012.

[5] S. Evans, ‘Design and optimization of a permanent magnet linear reluctance motor for reciprocating electro-mechanical systems’, Doctoral dissertation, Loughborough University of Technology, 1996.

[6] A. Egeland and C. Simon Wedlund, ‘Birkeland’s Electromagnetic Cannon’, *IEEE Trans. Plasma Sci.*, vol. 46, no. 6, pp. 2154–2161, Jun. 2018, doi: 10.1109/TPS.2018.2834980.

[7] P. J. Markey, ‘Linear Induction Motors’, in *Electromechanical Prime Movers: Electric Motors*, London: Macmillan Education UK, 1972, pp. 84–91. doi: 10.1007/978-1-349-01592-4_11.

[8] A. Egeland and C. Simon Wedlund, ‘Birkeland’s Electromagnetic Cannon’, *IEEE Trans. Plasma Sci.*, vol. 46, no. 6, pp. 2154–2161, 2018, doi: 10.1109/TPS.2018.2834980.

[9] A. Basak, *Permanent-magnet DC linear motors*. Oxford: Oxford universtiy press, 1996.

[10] E. R. Laithwaite, ‘Linear electric machines—A personal view’, *Proc. IEEE*, vol. 63, no. 2, pp. 250–290, 1975, doi: 10.1109/PROC.1975.9734.

[11] J. F. Gieras, Z. J. Piech, and B. Tomczuk, *Linear Synchronous Motors*. CRC Press, 2018. doi: 10.1201/b11105.

[12] E. R. Laithwaite, *A History of Linear Electric Motors*. London: Macmillan Education UK, 1987. doi: 10.1007/978-1-349-08296-4.

[13] S. Pan, ‘Development of permanent magnet tubular linear motor and position feedback device based on Hall sensor’, 2016, [Online]. Available: http://ro.uow.edu.au/cgi/viewcontent.cgi?article=5873&context=theses

[14] M. H. Nagrial, J. Rizk, and A. Hellany, ‘Design and performance of interior permanent magnet motors with saturating magnetic bridge’, in *2009 IEEE*

International Electric Machines and Drives Conference, IEMDC '09, 2009, pp. 922–927. doi: 10.1109/IEMDC.2009.5075314.

[15] N. Prasad, S. Jain, and S. Gupta, 'Electrical Components of Maglev Systems: Emerging Trends', *Urban Rail Transit*, vol. 5, no. 2, pp. 67–79, 2019, doi: 10.1007/s40864-019-0104-1.

[16] T. Hama and K. Sato, 'High-speed and high-precision tracking control of ultrahigh-acceleration moving-permanent-magnet linear synchronous motor', *Precis. Eng.*, vol. 40, pp. 151–159, 2015, doi: 10.1016/j.precisioneng.2014.11.005.

[17] N. Braiwish, 'Design Optimisation of Brushless Permanent Magnet Synchronous Motor for Electric Vehicles', Doctoral dissertation, Cardiff University, 2016.

[18] G. Otten, T. J. A. De Vries, J. Van Amerongen, A. M. Rankers, and E. W. Gaal, 'Linear motor motion control using a learning feedforward controller', *IEEE/ASME Trans. Mechatronics*, vol. 2, no. 3, pp. 179–187, 1997, doi: 10.1109/3516.622970.

[19] H. Yajima, H. Wakiwaka, K. Minegishi, N. Fujiwara, and K. Tamura, 'Design of linear DC motor for high-speed positioning', *Sensors Actuators, A Phys.*, vol. 81, no. 1, pp. 281–284, 2000, doi: 10.1016/S0924-4247(99)00175-2.

[20] K. K. Tan, S. N. Huang, H. F. Dou, T. H. Lee, S. J. Chin, and S. Y. Lim, 'Adaptive robust motion control for precise trajectory tracking applications', *ISA Trans.*, vol. 40, no. 1, pp. 57–71, 2001, doi: 10.1016/S0019-0578(00)00037-9.

[21] A. Röhrig, C., Jochheim, 'Motion Control of Linear Permanent Magnet Motors with Force Ripple Compensation System Modeling', *IFAC Proc. Vol.*, pp. 85–90, 2002.

[22] A. Saadha, C. V. Aravind, P. Krishna, and F. Azhar, 'Analysis of taper width variations in linear reluctance machine', *J. Eng. Sci. Technol.*, vol. 13, no. Special Issue on the ninth eureca 2017, pp. 17–26, 2018, [Online]. Available: https://doi.org/10.1051/matecconf/201815204001

[23] WATTS JL, 'Linear motors', *Mach. Prod. Eng.*, vol. 118, no. 3057, pp. 909–912, 1971, doi: 10.1007/978-3-642-22647-2_100380.

[24] P. Khong, 'Magnetic Guidance for Linear Drives', 2011. http://tuprints.ulb.tu-darmstadt.de/id/eprint/2756 (accessed Aug. 15, 2022).

[25] R. Cited, O. City, and R. U.-A. Data, 'MEMS Flow Sensor', vol. 1, no. 12, pp. 0–4, 2003, doi: 10.1016/j.(73).

[26] R. B. Oswald, 'Investigation of Control Methods for Segmented Long Stator Linear Drives', Doctoral dissertation, Technische Universität, 2008.

[27] S. Chevailler, 'comparative study and selection criteria of linear motors', Institut d'Electricité et de Microtechnique, 2006. doi: https://doi.org/10.5075/epfl-thesis-3569.

[28] S. A. Evans, I. R. Smith, and J. G. Kettleborough, 'Permanent-magnet linear actuator for static and reciprocating short-stroke electromechanical systems', *IEEE/ASME Trans. Mechatronics*, vol. 6, no. 1, pp. 36–42, 2001, doi: 10.1109/3516.914389.

[29] I. R. Smith, J. G. Kettleborough, and Y. Zhang, ‘Simplified modelling and dynamic analysis of a Laws’ relay actuator’, *Mechatronics*, vol. 9, no. 5, pp. 463–475, 1999, doi: 10.1016/S0957-4158(99)00007-0.

[30] J. Karlsson and O. Söderström, ‘Review of Magnetic Materials Along With a Study of the Magnetic Stability and Solidity of Y40’, *Uppsall Universitet*, no. June, 2012.

[31] Nasiri-Zarandi, R., Mirsalim, M. and Cavagnino, A., 2015. Analysis, optimization, and prototyping of a brushless DC limited-angle torque-motor with segmented rotor pole tip structure. IEEE Transactions on Industrial Electronics, 62(8), pp.4985-4993.

[32] Budig, P.K., 2000, August. The application of linear motors. In Proceedings IPEMC 2000. Third International Power Electronics and Motion Control Conference (IEEE Cat. No. 00EX435) (Vol. 3, pp. 1336-1341). IEEE.

[33] I. Boldea and S. A. Nasar, ‘Linear electric actuators and generators’, *IEEE Transactions on Energy Conversion*, vol. 14, no. 3, pp. 712–717, 1999, doi: 10.1109/60.790940.

[34] Wapler, M.C., Leupold, J., Dragonu, I., von Elverfeld, D., Zaitsev, M. and Wallrabe, U., 2014. Magnetic properties of materials for MR engineering, micro-MR and beyond. Journal of magnetic resonance, 242, pp.233-242.

[35] Dobrzański, L.A., Drak, M. and Ziębowicz, B., 2006. Materials with specific magnetic properties. journal of achievements in materials and manufacturing engineering, 17(1-2), pp.37-40.

[36] J. M. Powers, ‘LECTURE NOTES ON ENGINEERING COMPUTING’, no. November, 2013.

[37] Shirane, T. and Ito, M., 2012. Measurement of hysteresis loop on soft magnetic materials using lock-in amplifier. IEEE transactions on magnetics, 48(4), pp.1437-1440.

[38] ‘Hard Magnetic Materials | Electrical4U’, https://www.electrical4u.com/. [Online]. Available: https://www.electrical4u.com/hard-magnetic-materials/

[39] A. Inoue and F. Kong, ‘Soft Magnetic Materials’, in *Encyclopedia of Smart Materials*, 2021, pp. 10–23. doi: 10.1016/B978-0-12-803581-8.11725-4.

[40] J. M. Powers, *Lecture Notes on Engineering Computing*, no. November. 2013.

[41] Venzon, A.F., Carlson, R. and Sadowski, N., 2020. Design And Optimization Of A Brushless Motor Applied To A Formula SAE Vehicle. IEEE Latin America Transactions, 18(04), pp.756-763.

[42] O. Farrok, R. Md Islam, R. I. Md Sheikh, Y. Guo, J. Zhu, and G. Lei, ‘A novel method to avoid degradation due to demagnetization of PM linear generators for oceanic wave energy extraction’, in *2017 20th International Conference on Electrical Machines and Systems, ICEMS 2017*, 2017. doi: 10.1109/ICEMS.2017.8056471.

[43] Mouttouvelou, A., Balakrishna, V., Maruthachalam, S., Muthusamy, S., Panchal, H., Ramachandran, M. and Ammasi, V., 2023. An optimal selection of slot/pole combination and its influence on energy efficient PMSM for submersible water pumping applications. *International Journal of Ambient Energy*, 44(1), pp.654-667.

[44] A. Ismael, 'Microprocessor-controlled brushless DC linear stepping motor', This thesis is submitted for the degree of Doctor of Philosophy, Cardiff University, 2018. [Online]. Available: http://orca.cf.ac.uk/id/eprint/119080

[45] A. M. Technologies, 'Soft Magnetic Applications Guide', p. 19, 2015.

[46] R. Demirci, 'adaptive control of DC linear motors', university of wales college of cardiff, 1998.

[47] S. R. C. Ahmad *et al.*, 'Modeling and analysis of double stator slotted rotor permanent magnet generator', *Energies (Basel)*, vol. 10, no. 3, pp. 1–16, 2017, doi: 10.3390/en10030411.

[48] W. Huang, Y. Xue, G. Song, and Y. Sun, 'Analysis of end force and optimization design for linear permanent magnet brushless DC motor', in *2012 6th International Conference on Electromagnetic Field Problems and Applications, ICEF'2012*, IEEE, 2012, pp. 1–4. doi: 10.1109/ICEF.2012.6310373.

[49] P. Van Den Braembussche, J. Swevers, H. Van Brussel, and P. Vanherck, 'Accurate tracking control of linear synchronous motor machine tool axes', *Mechatronics*, vol. 6, no. 5, pp. 507–521, 1996, doi: 10.1016/0957-4158(95)00090-9.

[50] B. Yao and L. Xu, 'Adaptive robust motion control of linear motors for precision manufacturing', *Mechatronics*, vol. 12, no. 4, pp. 595–616, 2002, doi: 10.1016/S0957-4158(01)00008-3.

[51] K. K. Tan, T. H. Lee, H. Dou, and S. Zhao, 'Force ripple suppression in iron-core permanent magnet linear motors using an adaptive dither', *J Franklin Inst*, vol. 341, no. 4, pp. 375–390, 2004, doi: https://doi.org/10.1016/j.jfranklin.2004.01.003.

[52] J. E. Brittain and E. R. Laithwaite, 'A History of Linear Electric Motors', *Technol Cult*, vol. 31, no. 2, p. 337, 1990, doi: 10.2307/3105689.

[53] J. J. Brough, 'INTRODUCTION THE LINEAR D. C. MOTOR.', *Electronics and Power*, vol. 20, no. 15, pp. 628–632, 1974, doi: 10.1049/ep.1974.0462.

[54] G. Ratcliff and J. Griffiths, 'A linear d.c. motor', *J Sci Instrum*, vol. 41, no. 5, pp. 267–268, May 1964, doi: 10.1088/0950-7671/41/5/311.

[55] J. Griffiths and P. L. Jones, 'The direct current linear motor and its applications', in *4th University Power Engineering Conference scientific instruments*, Nottingham: University of Nottingham, 1969, pp. 98–99.

[56] Gieras, J.F., 2013, December. Linear electric motors in machining processes. In J. Int. Conf. Electr. Mach. Syst (Vol. 2, pp. 380-389).

[57] C. W. Green and R. J. A. Paul, ‘Application of d.c. linear machines as short-stroke and static actuators’, *Proceedings of the Institution of Electrical Engineers*, vol. 116, no. 4, p. 599, 1969, doi: 10.1049/piee.1969.0119.

[58] A. ’Basak, ‘An investigation of DC linear motor.’, university of wales, 1975.

[59] M. S. M. O. F. Yamaguchi, ‘Linear Direct Current Motor’, no. 19, 1993.

[60] A. Dascalescu, L; Morar, R; Iuga, ‘Ferrite-field DC Linear Motors for Electrode-positioning Systems of Electrostatic Separators’, in *An International Conference on Electric Machines and Drives*, Institution of Engineers, Australia, 1987, p. 473.

[61] A. Basak, ‘Generalised theory of ferrite-field dc linear motors’, *International Journal of Electrical Engineering Education 16.1*, pp. 43–49, 1979.

[62] A. Dascalescu, L; Morar, R; Iuga, ‘Ferrite-field DC Linear Motors for Electrode-positioning Systems of Electrostatic Separators’, in *An International Conference on Electric Machines and Drives*, 1987, p. 473.

[63] R. Akmese and J. F. Eastham, ‘Design of Permanent Magnet Flat Linear Motors for Standstill Applications’, *IEEE Trans Magn*, vol. 28, no. 5, pp. 3042–3044, 1992, doi: 10.1109/20.179711.

[64] A. Basak and F. J. Anayi, ‘A DC linear motor with a square armature’, *IEEE Transactions on Energy Conversion*, vol. 10, no. 3, pp. 462–469, 1995, doi: 10.1109/60.464869.

[65] F. J. Anayi and A. Basak, ‘Brushless NdFeB permanent magnet D.C. linear motors’, in *IEE Conference Publication*, 1989, pp. 71–75.

[66] A. Basak and A. F. Flores Filho, ‘Investigation of a novel double armature brushless D.C. linear motor’, in *Conference Record - IAS Annual Meeting (IEEE Industry Applications Society)*, 1995, pp. 789–795. doi: 10.1109/ias.1995.530379.

[67] A. Basak and A. F. Flores Filho, ‘Investigation of a novel double armature brushless D.C. linear motor’, in *Conference Record - IAS Annual Meeting (IEEE Industry Applications Society)*, 1995, pp. 789–795. doi: 10.1109/ias.1995.530379.

[68] A. Basak and A. F. F. Filho, ‘utation of Force in a Novel Brushless’, *IEEE Trans Magn*, vol. 3, no. 2, pp. 2030–2032, 1997.

[69] A. Basak and F. J. Anayi, ‘A DC linear motor with a square armature’, *IEEE Transactions on Energy Conversion*, vol. 10, no. 3, pp. 462–469, 1995, doi: 10.1109/60.464869.

[70] A. Basak and A. F. F. Filho, ‘utation of Force in a Novel Brushless’, *IEEE Trans Magn*, vol. 3, no. 2, pp. 2030–2032, 1997.

[71] P. E. F. Duggan, ‘Linear Dc Permanent Magnet Motor’, Art. no. 4,369,383, 1983.

[72] M. Wang, L. Li, and R. Yang, ‘Overview of thrust ripple suppression technique for linear motors’, *Chinese Journal of Electrical Engineering*, vol. 2, no. 1. pp. 77–84, 2016. doi: 10.23919/CJEE.2016.7933117.

[73] W. Huang, Y. Xue, G. Song, and Y. Sun, ‘Analysis of end force and optimization design for linear permanent magnet brushless DC motor’, in *2012 6th International Conference on Electromagnetic Field Problems and Applications, ICEF’2012*, IEEE, 2012, pp. 1–4. doi: 10.1109/ICEF.2012.6310373.

[74] S. Wang, X. Wang, X. Xu, and J. Cao, ‘Study on minimizing the detent force of PM linear brushless DC motors’, in *Proceedings of the 11th International Conference on Electrical Machines and Systems, ICEMS 2008*, 2008, pp. 3430–3434.

[75] N. Baatar, H. S. Yoon, M. T. Pham, P. S. Shin, and C. S. Koh, ‘Shape optimal design of a 9-pole 10-slot PMLSM for detent force reduction using adaptive response surface method’, *IEEE Trans Magn*, vol. 45, no. 10, pp. 4562–4565, 2009, doi: 10.1109/TMAG.2009.2022640.

[76] Z. P. Xi and D. Howe, ‘Redluction of cogging force in slotless linear per im a n e n’, *Power*, 1997.

[77] H. H. Luo, J. Wu, and W. Sen Chang, ‘Minimizing thrust fluctuation in moving-magnet permanent-magnet brushless linear DC motors’, *IEEE Trans Magn*, vol. 43, no. 5, pp. 1968–1972, 2007, doi: 10.1109/TMAG.2007.892081.

[78] Y. W. Zhu, D. H. Koo, and Y. H. Cho, ‘Detent force minimization of permanent magnet linear synchronous motor by means of two different methods’, *IEEE Trans Magn*, vol. 44, no. 11 PART 2, pp. 4345–4348, 2008, doi: 10.1109/TMAG.2008.2001320.

[79] S. Zhen, P. Chen, X. Chen, F. Qin, and H. Zhou, ‘Force Ripple Modeling and Minimizing of an Ironless Permanent-Magnet Linear Synchronous Motor’, *International Journal of Precision Engineering and Manufacturing*, vol. 20, no. 6, pp. 927–935, 2019, doi: 10.1007/s12541-019-00065-5.

[80] N. Bianchi, S. Bolognani, and A. D. F. Cappello, ‘Reduction of cogging force in PM linear motors by pole-shifting’, *IEE Proceedings: Electric Power Applications*, vol. 152, no. 3, pp. 703–709, 2005, doi: 10.1049/ip-epa:20045082.

[81] M. Wang, L. Li, and R. Yang, ‘Overview of thrust ripple suppression technique for linear motors’, *Chinese Journal of Electrical Engineering*, vol. 2, no. 1. pp. 77–84, 2016. doi: 10.23919/CJEE.2016.7933117.

[82] S. J. Imen and M. Shakeri, ‘Feed forward adaptive control of a linear brushless DC motor’, in *Proceedings of the SICE Annual Conference*, 2007, pp. 2200–2204. doi: 10.1109/SICE.2007.4421353.

[83] B. Yao and L. Xu, ‘Adaptive robust motion control of linear motors for precision manufacturing’, *Mechatronics*, vol. 12, no. 4, pp. 595–616, 2002, doi: 10.1016/S0957-4158(01)00008-3.

[84] J. Wu, C. Liu, Y. J. Liu, Z. Xiong, and H. Ding, ‘Force ripple compensation of the directly-driven linear motors via iterative tuning feed-forward controller’, *Proceedings of the Institution of Mechanical Engineers. Part I: Journal of Systems and Control Engineering*, vol. 233, no. 9, pp. 1239–1247, 2019, doi: 10.1177/0959651819827707.

[85] S. Zhao and K. K. Tan, ‘Adaptive feedforward compensation of force ripples in linear motors’, *Control Eng Pract*, vol. 13, no. 9, pp. 1081–1092, 2005, doi: https://doi.org/10.1016/j.conengprac.2004.11.004.

[86] W. J. Shi and D. C. Zhang, ‘Adaptive robust control of linear motor with ripple force compensation’, in *Proceedings - PACCS 2011: 2011 3rd Pacific-Asia Conference on Circuits, Communications and System*, IEEE, 2011, pp. 1–4. doi: 10.1109/PACCS.2011.5990177.

[87] K. Cho, J. Kim, S. Ben Choi, and S. Oh, ‘A high-precision motion control based on a periodic adaptive disturbance observer in a PMLSM’, *IEEE/ASME Transactions on Mechatronics*, vol. 20, no. 5, pp. 2158–2171, 2015, doi: 10.1109/TMECH.2014.2365996.

[88] S. L. Chen and T. H. Hsieh, ‘Repetitive control design and implementation for linear motor machine tool’, *Int J Mach Tools Manuf*, vol. 47, no. 12–13, pp. 1807–1816, 2007, doi: 10.1016/j.ijmachtools.2007.04.009.

[89] T. H. Lee, K. K. Tan, S. Y. Lim, and H. F. Dou, ‘Iterative learning control of permanent magnet linear motor with relay automatic tuning’, *Mechatronics*, vol. 10, no. 1–2, pp. 169–190, 2000, doi: 10.1016/S0957-4158(99)00074-4.

[90] W. Qian, S. K. Panda, and J. X. Xu, ‘Torque ripple minimization in PM synchronous motors using iterative learning control’, *IEEE Trans Power Electron*, vol. 19, no. 2, pp. 272–279, 2004, doi: 10.1109/TPEL.2003.820537.

[91] M. Wang, L. Li, and D. Pan, ‘Detent force compensation for PMLSM systems based on structural design and control method combination’, *IEEE Transactions on Industrial Electronics*, vol. 62, no. 11, pp. 6845–6854, 2015, doi: 10.1109/TIE.2015.2443096.

[92] M. S. Manna, S. Marwaha, A. Marwaha, and C. Vasudeva, “Analysis of permanent magnet linear induction motor (PMLIM) using finite element method,” *ARTCom* 2009 - *International Conference on Advances in Recent Technologies in Communication and Computing*, pp. 540–542, 2009, doi: 10.1109/ARTCom.2009.42

[93] H. N. Phyu, “Numerical Analysis of a Brushless Permanent Magnet Dc Motor Using Coupled Systems,” UNIVERSITY OF SINGAPORE, 2004.

[94] A. Sitzia, “Book Review: Permanent Magnets in Theory and Practice, 2nd Ed.,” *The International Journal of Electrical Engineering & Education*, vol. 26, no.3, pp. 266-267, Jul. 1989, doi: 10.1177/002072098902600317.

[95] S. A. Evans, “Design and optimization of a permanent magnet linear reluctance motor for reciprocating electro-mechanical systems.” Sep. 14, 2016.

[96] Y. Fastest, S. To, and A. B. Design, “2D & 3D Tutorials.” 2015.

[97] P. J. Ramírez and A. R. Guesalaga, ‘A Friction Model Describing Limit Cycles in Positioning Servos’, *The Journal of Defense Modeling and Simulation: Applications, Methodology, Technology*, vol. 6, no. 4, pp. 177–184, 2009, doi: 10.1177/1548512909354614.

[98] F. Melmuka, ‘Abwasserneutralisation Mit Rauchgas, Ein Relativ Billiges Behandlungsverfahren’, *Melliand Textilberichte*, vol. 56, no. 2, pp. 158–159, 1975.

[99] M. Dursun and A. Saygın, ‘A New Design of Single Side Brushless Direct Current Linear Motor’, vol. 3, no. 4, pp. 336–342, 2015, doi: 10.12720/joace.3.4.336-342.

[100] M. Tomizuka, ‘Design of linear DC motor for high-speed positioning’, vol. 43, no. 1, pp. 48–55, 1996.

[101] S. Urushihara, T. Kamano, T. Suzuki, and H. Harada, ‘High-Performance Positioning System with Linear DC Servo Motor under Self-tuning Fuzzy Control’, vol. 5008, 2010, doi: 10.1080/153250001300003403.

[102] K. K. Tan, S. N. Huang, and T. H. Lee, ‘Robust adaptive numerical compensation for friction and force ripple in permanent-magnet linear motors’, *IEEE Trans Magn*, vol. 38, no. 1 II, pp. 221–228, 2002, doi: 10.1109/20.990111.

[103] X. Bo Tran, V. Lai Nguyen, and K. Duong Tran, ‘Effects of friction models on simulation of pneumatic cylinder’, *Mechanical Sciences*, vol. 10, no. 2, pp. 517–528, 2019, doi: 10.5194/ms-10-517-2019.

[104] K. J. Astrom and C. Canudas-De-Wit, ‘Revisiting the LuGre Friction Model’, *IEEE Control Syst*, vol. 28, no. 6, pp. 101–114, 2008, doi: 10.1109/MCS.2008.929425.

[105] B. Qin, R. Zeng, X. Li, and J. Yang, ‘Design and performance analysis of the hydropneumatic suspension system for a novel road-rail vehicle’, *Applied Sciences (Switzerland)*, vol. 11, no. 5, pp. 1–16, 2021, doi: 10.3390/app11052221.

[106] M. S. Manna, S. Marwaha, A. Marwaha, and C. Vasudeva, ‘Analysis of permanet magnet linear induction motor (PMLIM) using finite element method’, *ARTCom 2009 - International Conference on Advances in Recent Technologies in Communication and Computing*, pp. 540–542, 2009, doi: 10.1109/ARTCom.2009.42.

[107] H. N. Phyu, ‘Numerical Analysis of a Brushless Permanent Magnet Dc Motor Using Coupled Systems’, UNIVERSITY OF SINGAPORE, 2004.

[108] A. Sitzia, ‘Book Review: Permanent Magnets in Theory and Practice, 2nd Ed.’, *The International Journal of Electrical Engineering & Education*, vol. 26, no. 3, pp. 266–267, Jul. 1989, doi: 10.1177/002072098902600317.

[109] C. C. Soon, R. Ghazali, H. I. Jaafar, and S. Y. S. Hussien, ‘Sliding Mode Controller Design with Optimized PID Sliding Surface Using Particle Swarm Algorithm’, in *Procedia Computer Science*, The Author(s), 2017, pp. 235–239. doi: 10.1016/j.procs.2017.01.216.

[110] M. Babaie, M. Sharifzadeh, M. Mehrasa, and K. Al-Haddad, ‘Optimized based algorithm first order sliding mode control for grid-connected packed e-cell (PEC) inverter’, in *2019 IEEE Energy Conversion Congress and Exposition, ECCE 2019*, IEEE, 2019, pp. 2269–2273. doi: 10.1109/ECCE.2019.8913100.

[111] M. Yahiaoui, A. Kechich, and I. K. Bouserhane, ‘Adaptive Sliding Mode Control of PMLSM Drive’, vol. 8, no. 2, pp. 639–646, 2017, doi: 10.11591/ijpeds.v8i2.pp639-646.

[112] J. Fang, Z. Long, M. Y. Wang, L. Zhang, and X. Dai, ‘Multi-mode sliding mode control for precision linear stage based on fixed or floating stator’, vol. 025115, no. February 2016, 2019, doi: 10.1063/1.4942641.

[113] L. Yu, J. Huang, W. Luo, S. Chang, H. Sun, and H. Tian, ‘Sliding-Mode Control for PMLSM Position Control—A Review’, *Actuators*, vol. 12, no. 1, p. 31, 2023, doi: 10.3390/act12010031.

[114] K. Cho, J. Kim, H. Park, and S. Choi, ‘Periodic adaptive disturbance observer for a Permanent Magnet Linear Synchronous Motor’, in *2012 IEEE 51st IEEE Conference on Decision and Control (CDC)*, 2012, pp. 4684–4689. doi: 10.1109/CDC.2012.6426591.

[115] Z. Has, A. H. Muslim, and N. A. Mardiyah, ‘Adaptive-fuzzy-PID controller based disturbance observer for DC motor speed control’, in *2017 4th International Conference on Electrical Engineering, Computer Science and Informatics (EECSI)*, 2017, pp. 1–6. doi: 10.1109/EECSI.2017.8239165.

[116] N. Saikumar, R. K. Sinha, and S. Hassan Hossein Nia, ‘Resetting disturbance observers with application in compensation of bounded nonlinearities like hysteresis in piezo-actuators’, *Control Eng Pract*, vol. 82, pp. 36–49, 2019, DOI: 10.1016/j.conengprac.2018.09.026.

[117] C. Xu, Y. Jin, and J. Na, ‘Performance improvement of a sigma-delta modulator using fractional-order disturbance observer’, *Journal of Vibroengineering*, vol. 20, no. 4, pp. 1907–1918, 2018, doi: 10.21595/jve.2017.18954.

[118] T. Umeno and Y. Hori, ‘Robust speed control of DC servomotors using modern two degrees-of-freedom controller design’, *IEEE Transactions on Industrial Electronics*, vol. 38, no. 5, pp. 363–368, 1991, doi: 10.1109/41.97556.

[119] M. Tomizuka, ‘Model based prediction, preview and robust controls in motion control systems’, in *Proceedings of 4th IEEE International Workshop on Advanced Motion Control - AMC ’96 - MIE*, 1996, pp. 1–6 vol.1. doi: 10.1109/AMC.1996.509370.

[120] R. V. Rao and V. Patel, ‘An elitist teaching-learning-based optimization algorithm for solving complex constrained optimization problem’, vol. 3, pp. 535–560, 2012, doi: 10.5267/j.ijiec.2012.03.007.

[121] M. Babaie, M. Sharifzadeh, M. Mehrasa, and K. Al-Haddad, ‘Optimized based algorithm first order sliding mode control for grid-connected packed e-cell (PEC) inverter’, in *2019 IEEE Energy Conversion Congress and Exposition, ECCE 2019*, IEEE, 2019, pp. 2269–2273. doi: 10.1109/ECCE.2019.8913100.

[122] J. Brownlee, *Clever Algorithms: Nature-Inspired Programming Recipes*. Melbourne, 2011.

[123] D. T. Pham, A. Ghanbarzadeh, E. Koç, S. Otri, S. Rahim, and M. Zaidi, ‘The Bees Algorithm — A Novel Tool for Complex Optimisation Problems’, in *Intelligent Production Machines and Systems*, Elsevier, 2006, pp. 454–459. doi: 10.1016/B978-008045157-2/50081-X.

[124] M. A. S, ‘Optimisation of a PID controller for a two-floor structure under earthquake excitation based on the bees algorithm’, 2018, doi: 10.1177/1461348418757906.

[125] M. Arif Şen, M. Tinkir, and M. Kalyoncu, ‘Optimisation of a PID controller for a two-floor structure under earthquake excitation based on the bees algorithm’, *Journal of Low Frequency Noise, Vibration and Active Control*, vol. 37, no. 1, pp. 107–127, Mar. 2018, doi: 10.1177/1461348418757906.

[126] M. Sarailoo, Z. Rahmani, and B. Rezaie, ‘A novel model predictive control scheme based on bees algorithm in a class of nonlinear systems: Application to a three tank system’, *Neurocomputing*, vol. 152, pp. 294–304, Mar. 2015, doi: 10.1016/j.neucom.2014.10.066.

[127] N. Hartono, F. J. Ramírez, and D. T. Pham, ‘Optimisation of robotic disassembly plans using the Bees Algorithm’, *Robot Comput Integr Manuf*, vol. 78, p. 102411, Dec. 2022, doi: 10.1016/j.rcim.2022.102411.

[128] J. Liu, Z. Zhou, D. T. Pham, W. Xu, C. Ji, and Q. Liu, ‘Collaborative optimization of robotic disassembly sequence planning and robotic disassembly line balancing problem using improved discrete Bees algorithm in remanufacturing☆’, *Robot Comput Integr Manuf*, vol. 61, p. 101829, Feb. 2020, doi: 10.1016/j.rcim.2019.101829.

[129] P. Tapkan, L. Özbakır, S. Kulluk, and A. Baykasoğlu, ‘A cost-sensitive classification algorithm: BEE-Miner’, *Knowl Based Syst*, vol. 95, pp. 99–113, Mar. 2016, doi: 10.1016/j.knosys.2015.12.010.

[130] M. S. Packianather, A. K. Al-Musawi, and F. Anayi, ‘Bee for mining (B4M) – A novel rule discovery method using the Bees algorithm with quality-weight and coverage-weight’, *Proc Inst Mech Eng C J Mech Eng Sci*, vol. 233, no. 14, pp. 5101–5112, Jul. 2019, doi: 10.1177/0954406219833719.

[131] E. Oztemel and A. A. Selam, ‘Bees Algorithm for multi-mode, resource-constrained project scheduling in molding industry’, *Comput Ind Eng*, vol. 112, pp. 187–196, Oct. 2017, doi: 10.1016/j.cie.2017.08.012.

[132] S. Abdullah and M. Alzaqebah, ‘A hybrid self-adaptive bees algorithm for examination timetabling problems’, *Appl Soft Comput*, vol. 13, no. 8, pp. 3608–3620, Aug. 2013, doi: 10.1016/j.asoc.2013.04.010.

[133] T. Mazitov, P. Božek, A. Abramov, Y. Nikitin, and I. Abramov, ‘Using Bee Algorithm in the Problem of Mapping’, *Procedia Eng*, vol. 149, pp. 305–312, 2016, doi: 10.1016/j.proeng.2016.06.671.

[135] G.-H. Luo, S.-K. Huang, Y.-S. Chang, and S.-M. Yuan, ‘A parallel Bees Algorithm implementation on GPU’, *Journal of Systems Architecture*, vol. 60, no. 3, pp. 271–279, Mar. 2014, doi: 10.1016/j.sysarc.2013.09.007.

[135] J. Li, Q. Pan, and K. Mao, ‘Engineering Applications of Artificial Intelligence A discrete teaching-learning-based optimisation algorithm for realistic flowshop rescheduling problems’, *A discrete teaching-learning-based optimisation algorithm for realistic flowshop rescheduling problems*, vol. 37, pp. 279–292, 2015, doi: 10.1016/j.engappai.2014.09.015.

[136] R. V Rao, V. J. Savsani, and D. P. Vakharia, ‘Teaching-Learning-Based Optimization: An optimization method for continuous non-linear large scale problems’, *Inf Sci (N Y)*, vol. 183, no. 1, pp. 1–15, 2012, doi: 10.1016/j.ins.2011.08.006.

[137] Zare, S., Pourfayaz, F., Tavakolpour-Saleh, A.R., Mohammadian, A. and Mirshekari, R., 2023. Investigation of a two-diaphragm thermoacoustic Stirling engine using passivity method. Journal of the Brazilian Society of Mechanical Sciences and Engineering, 45(10), pp.1-17.

[138] Edwards, C. and Spurgeon, S., 1998. Sliding mode control: theory and applications. Crc Press.

[139] Slotine, J.J.E. and Li, W., 1991. Applied nonlinear control (Vol. 199, No. 1, p. 705). Englewood Cliffs, NJ: Prentice hall.

[140] Gao, W. and Hung, J.C., 1993. Variable structure control of nonlinear systems: A new approach. *IEEE transactions on Industrial Electronics*, *40*(1), pp.45-55

[141] M. Arif Şen, M. Tinkir, and M. Kalyoncu, “Optimisation of a PID controller for a two-floor structure under earthquake excitation based on the bees algorithm,” J. Low Freq. Noise, Vib. Act. Control, vol. 37, no. 1, pp. 107–127, Mar. 2018, doi: 10.1177/1461348418757906.

[142] V. Bakırcıoğlu, M. Arif Şen, and M. Kalyoncu, “Optimization of PID controller based on The Bees Algorithm for one leg of a quadruped robot,” MATEC Web Conf., vol. 42, p. 03004, Feb. 2016, doi: 10.1051/matecconf/20164203004.

[143] A. A. Fahmy, M. Kalyoncu, and M. Castellani, “Automatic design of control systems for robot manipulators using the bees algorithm,” Proc. Inst. Mech. Eng. Part I J. Syst. Control Eng., vol. 226, no. 4, pp. 497–508, Apr. 2012, doi: 10.1177/0959651811425312.

[144] M. A. Sen and M. Kalyoncu, “Optimisation of a PID Controller for an Inverted Pendulum Using the Bees Algorithm,” Appl. Mech. Mater., vol. 789–790, pp. 1039–1044, Sep. 2015, doi: 10.4028/www.scientific.net/AMM.789-790.1039.

Appendix A:

Design and modelling DC linear motor by using MagNet software.

This is the simulation for DC linear motor using MagNet. Figure 1 shows the configuration of the armature windings which were distributed along with the armature core. There are 28 independent coils distributed along of the armature core with enamelled copper wire of 0.5 mm in diameter. This allows for a maximum DC current of 29 A to flow. In addition, the armature windings are electrically independent of each other. The coils designed by 670 turns, with 42 mm length and 5.5 mm thickness. So, the air gap will be 6 mm. In this simulation, the air gap was 6 mm to avoid any increasing air gap and the current was around 5 A. The results were as shown below:

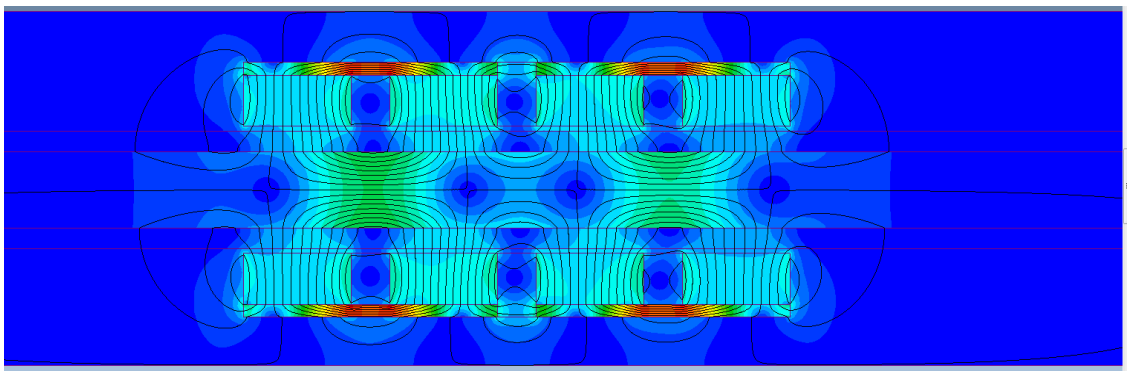

Figure A.0.1 Modelling linear Dc motor using MagNet

Figure A.2 shows the computed radial component of the flux density in the airgap between the armature winding and the magnet in X direction.

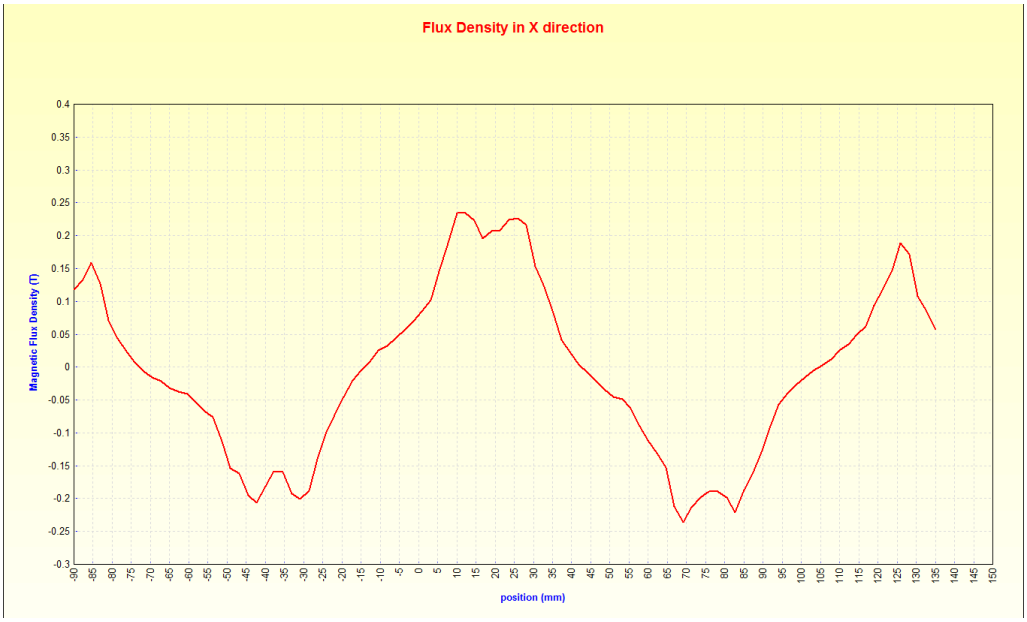

Figure A.0.2 Magnetic flux distribution (T) in air gap B-x

Figure A.3 shows the computed radial component of the flux density in the airgap between the armature winding and the magnet in Y direction.

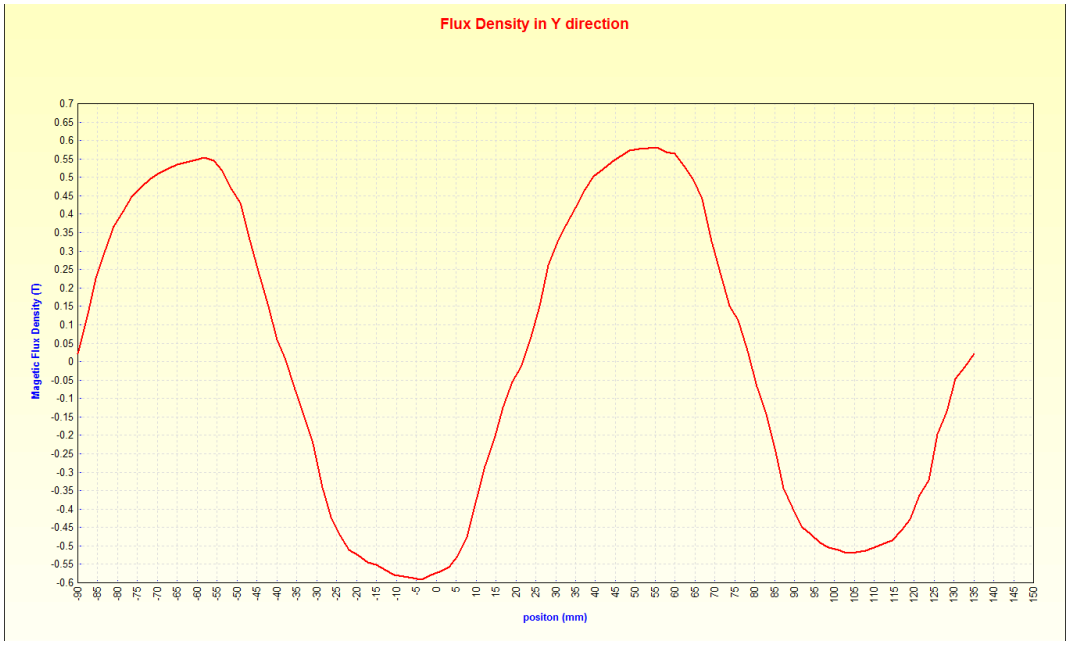

Figure A.0.3 Magnetic flux distribution (T) in air gap B-y

The figure below shows the line graph of the thrust force and position each time the mover moves.

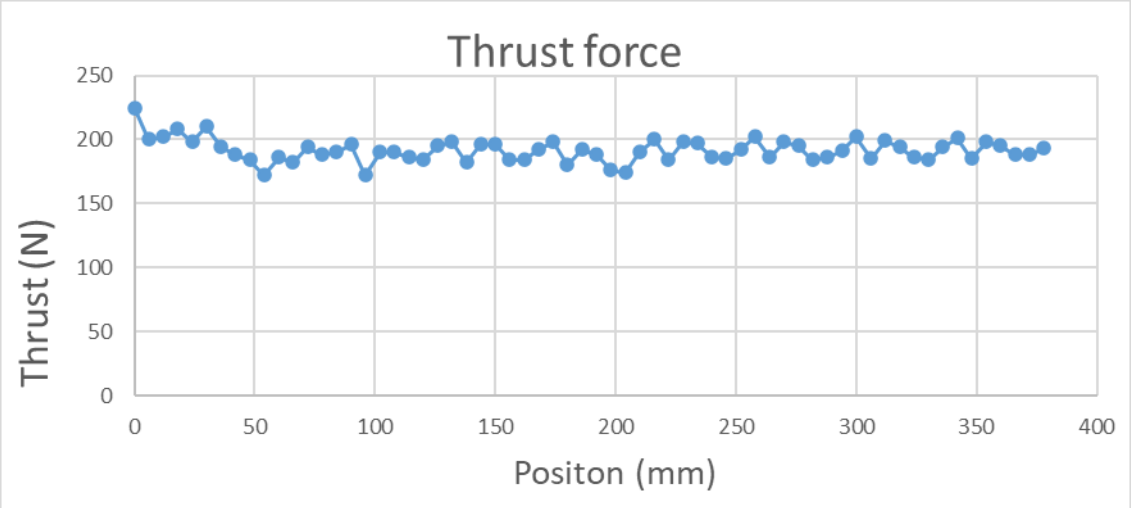

Figure A.0.4 thrust force to the motor displacement.

Steady state friction and velocity curve MATLAB code

```
% Draw the friction force.

 sigma = 23.7;
Fc = 25.011;
Fs = 32.07;
vs = 0.04;
v = -0.5:0.001:0.5;

Fss = lugref_ss(v, Fc, Fs, vs, sigma);
figure
plot(v, Fss)
grid
xlabel('velocity (m/s)')
ylabel('friction force (N)')
title('friction force at steady condition')


function Fss = lugref_ss(v, Fc, Fs, vs, sigma)
r = -(v/vs).^2;
Fss = Fc * sign(v) + (Fs - Fc) * exp(r) .*sign(v) + sigma * v;
end
```

The Table below shows the distance with which coils must energise each time the mover moves with 6 mm. in the simulation all distance has been tested.

Position	W1	W2	W3	W4	W5	W6	W7	W8	W9	W10	W11	W12
0	3	-3		3								
06	3	-3		3								
12	3		-3	3								
18	3		-3	3								
24	3		-3	3								
30		3	-3	3								
36		3	-3	3								
42		3	-3		3							
48		3	-3		3							
54		3		-3	3							
60		3		-3	3							
66		3		-3	3							
72			3	-3	3							
78			3	-3	3							
84			3	-3		3						
90			3	-3		3						
96			3			3						
102			3		-3	3						
108			3		-3	3						
114				3	-3	3						
120				3	-3	3						
126				3	-3		3					
132				3	-3		3					
138				3	-3		3					
144				3		-3	3					
150				3		-3	3					
156					3	-3	3					
162					3	-3	3					
168					3	-3		3				
174					3	-3		3				
180					3	-3		3				
186					3		-3	3				
192					3		-3	3				
198						3	-3	3				
204						3	-3	3				
210						3	-3		3			
216						3	-3		3			
222						3	-3		3			
228						3		-3	3			
234						3		-3	3			
240							3	-3	3			
246							3	-3	3			

252							3	-3		3		
258							3	-3		3		
264							3	-3		3		
270							3		-3	3		
276							3		-3	3		
282								3	-3	3		
294								3	-3	3		

Appendix B:

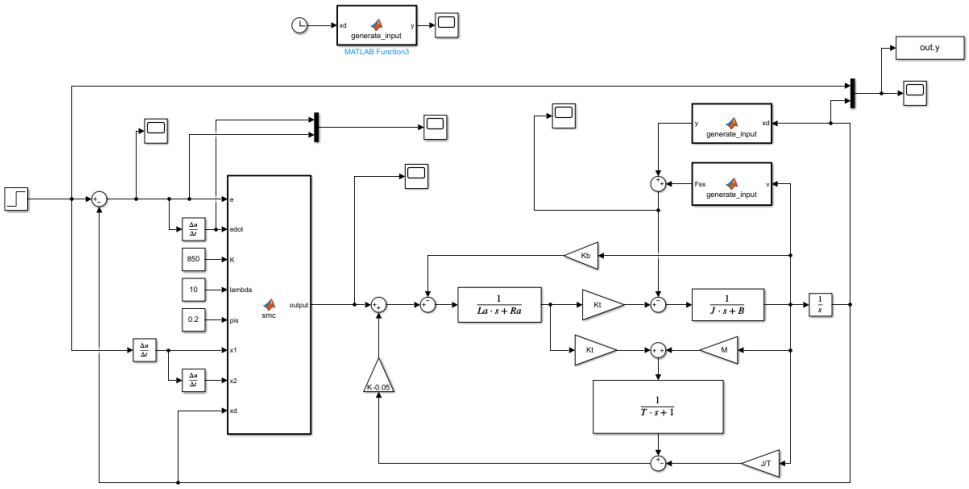

Figure B.1 MATLAB Simulink of control position using SMC-DOB

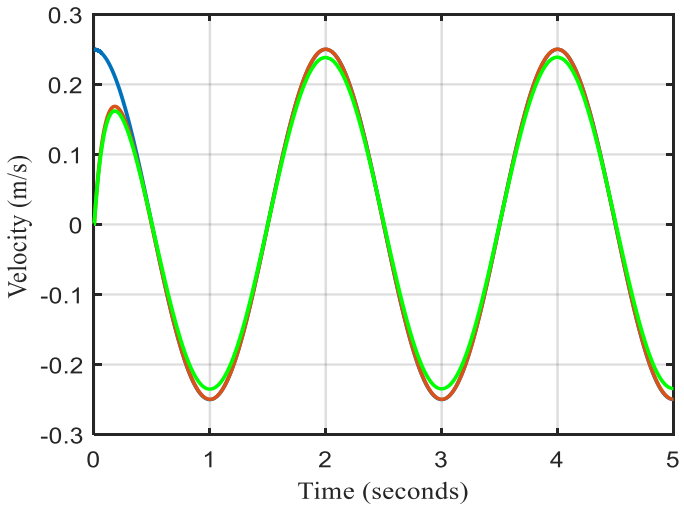

Figure B.2 The tracking speed of the SMC with and without DOB

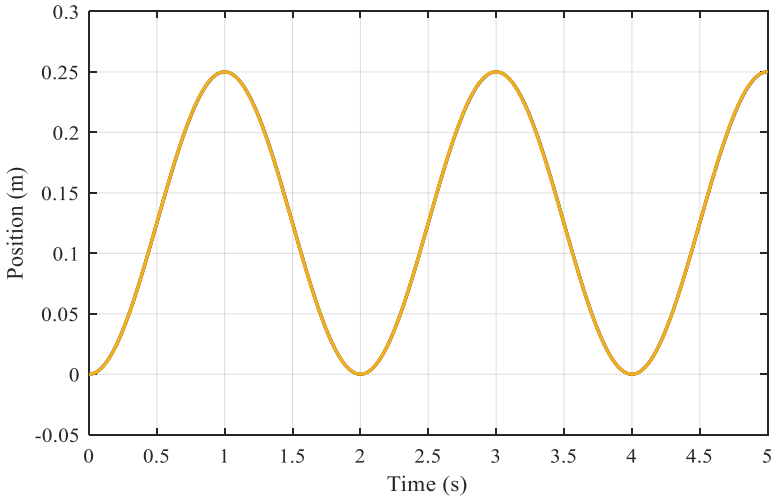

Figure B.3 The tracking performance of the SMC-DOB

1 - Design the proposed controller

After simulating the linear DC motor and test the controller using Mathlab, it can be designed as well in Labview, it can design the proposed control using LabVIEW by a method called Math-Script. figure 5 shows the sliding mode control in LabVIEW designed by Math-script for a Linear DC motor.

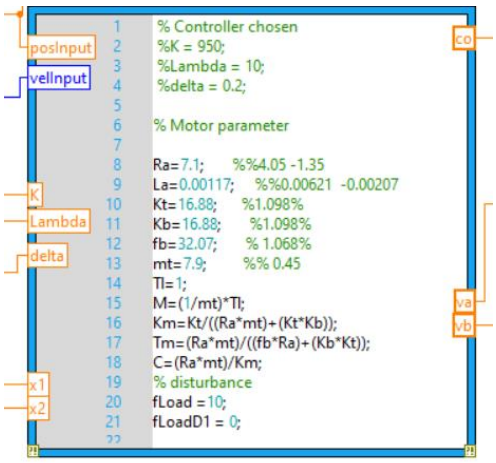

Figure B.4 Sliding mode control in LabVIEW designed by Math-script.

The linear DC motor has been designed in LabVIEW using mathematical model and state-space equations. Figure 6 shows sliding controller and plant

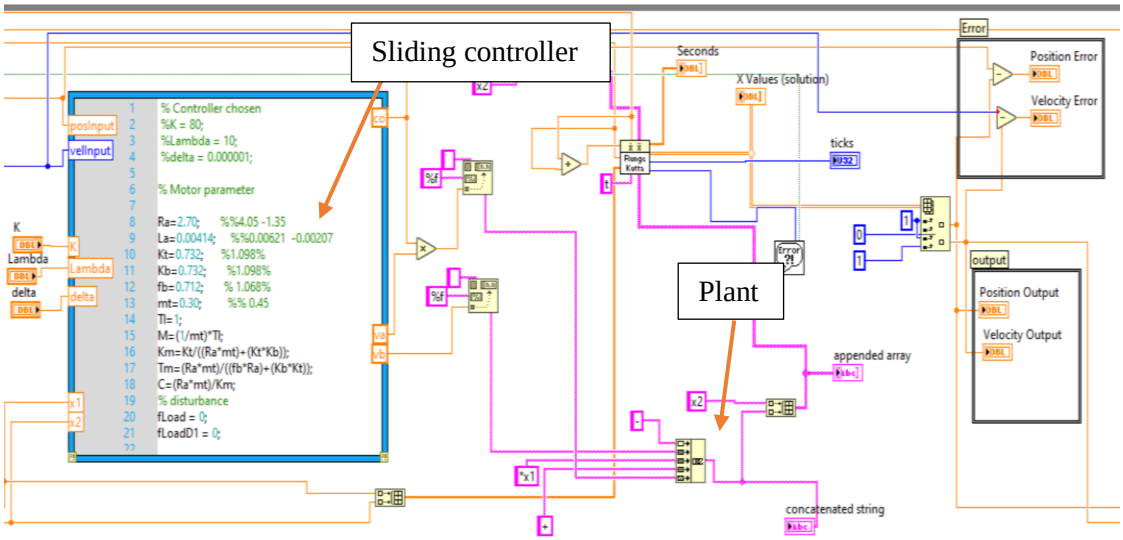

Figure B.5 Block diagram of sliding mode control of linear dc motor by LabVIEW

2 - Design laser sensor distance measurement

A laser sensor measurement can be designed via LabVIEW using visa function to write/read from the sensor.

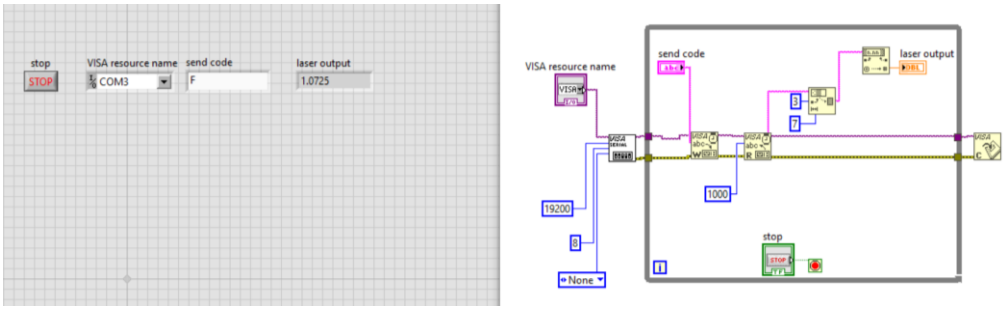

Figure B.6 Block diagram of laser sensor measurement

3 - The Results

Figure B.7 shows the results of the front panel and block diagram of the system.

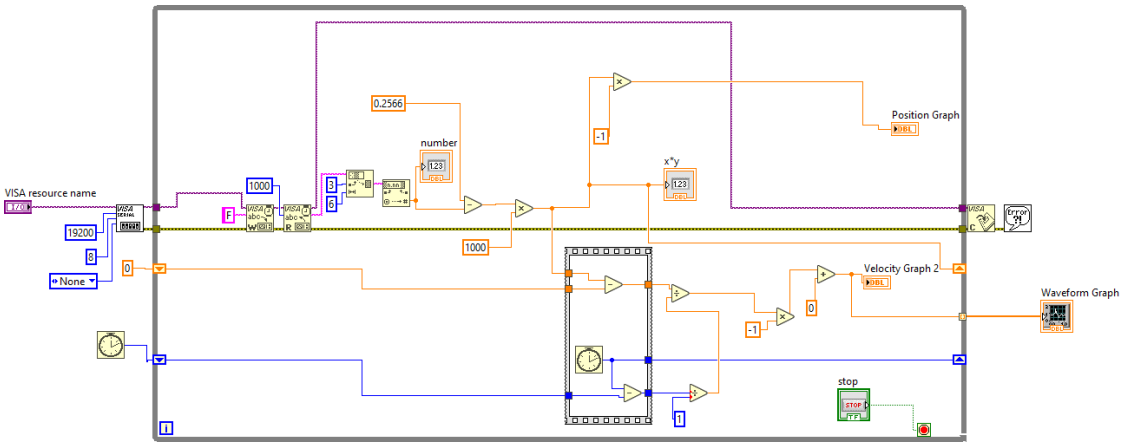

Figure B.7 Motor speed and position measurement via LabVIEW

Table B.0-1 Load cell calibration

Current	mV	Force	measurement
2	0	0	47.5
2.5	1.9	23.76	55.4
3	2.6	32.52	63
3.5	3.4	42.53	70.6
4	4.4	50.04	78.2
4.5	4.6	57.54	85.8
5	5.7	71.30	93.2
5.5	6.4	80.06	101
6	7	87.57	108.7
6.5	7.6	95.07	116.3
7	8.2	102.58	123.8

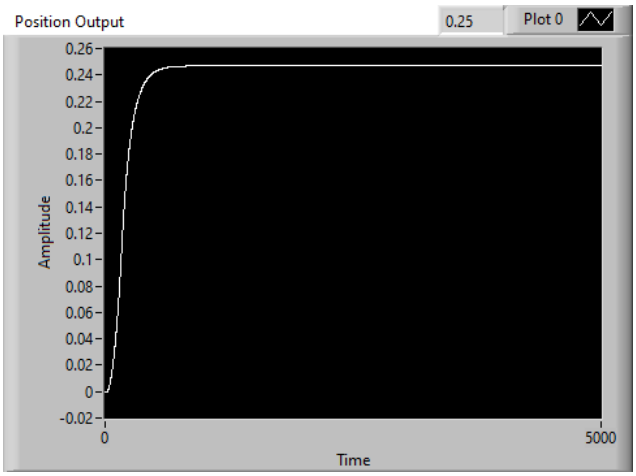

Figure B.8 Step response of position control measurement via LabVIEW

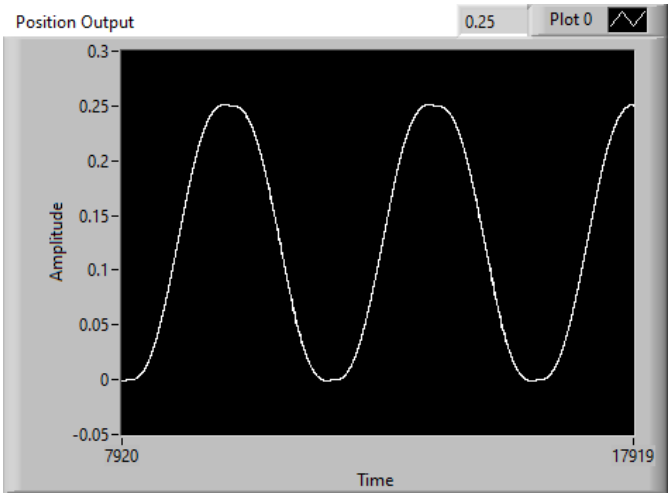

Figure B.9 Sinusoidal response of position control measurement via LabVIEW

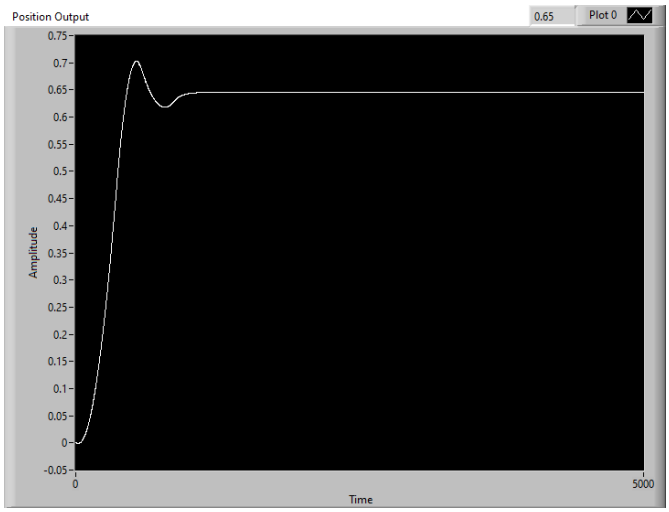

Figure B.10 Step response of control position measurement with 10 kg payload.

Bee's algorithm MATLAB code

```
%========== BEES ======================%
%========== PoP Member = particle ==============%

clear
close all
Ra=7.1;
La=0.00117;
Kt=16.88;       %the half length of the pendulum%
Kb=16.88;        % friction constant pendulum%
fb=11.25;        % friction constant cart%
mt=6.74;
Tl=1;
M=(1/mt)*Tl;
Km=Kt/((Ra*mt)+(Kt*Kb));
Tm=(Ra*mt)/((fb*Ra)+(Kb*Kt));
C=(Ra*mt)/Km;
B=(Km/Ra*mt);
kg=((B*Ra)+Km^2)/(Ra*mt);
Cm=Km/Tm;
Nm=1/Tm;
ts=0.001;

maxitr=20;
nbees = 10; %the number of scott bees
msite = 5; %number of best scotts
elite=2; % the number of elits
other=msite-elite;
nelite=5; %the number of bees sent to the elites sites
nother=3; %the number of bees sent to the other sites else elit
ngh=[0.01,0.01,0.01]; %the interval lenght for nigherbing for
variable 1
```

```
nvar=3; %number of variables
Lb=[1 1 0]; %lower boundary
Ub=[10 10 0.9]; %uper boundary   you can define a SS matrix as like
SS=[-10,20;10,50]
object = @slidingM;
bestmatrix=zeros(maxitr,1); %a matrix to draw the result of search
progress


pop = Lb+(Ub-Lb).*rand(nbees,nvar); %initial population is generated

pop(:,nvar+1)=object(pop);
functionevaluation=nbees;
itr=0;

while itr<=maxitr
   itr=itr+1

   bestmatrix(itr,1)=pop(1,nvar+1);

   popelite=zeros(elite*(1+nelite),nvar+1);


   popother=zeros(other*(1+other),nvar+1);



   for i=1:elite
       popelite(i,:)=pop(i,:);
       for j=(i*nelite-nelite)+1:i*nelite
           max=pop(i,1:nvar).*(1+ngh);
           min=pop(i,1:nvar).*(1-ngh);
          for z=1:nvar
              if max(1,z)>Ub(1,z)
                  max(1,z)=Ub(1,z);
              elseif min(1,z)<Lb(1,z)
                    min(1,z)=Lb(1,z);
              end
          end
          popelite(j+elite,1:nvar)=min+(max-min).*rand(1,nvar);
          popelite(j+elite,nvar+1)=object( popelite(j+elite,:));
          functionevaluation=functionevaluation+1;
       end
   end


   for i=1:other
       popother(i,:)=pop(i+elite,:);
       for j=(i*nother-nother)+1:i*nother
           max=pop(i+elite,1:nvar).*(1+ngh);
           min=pop(i+elite,1:nvar).*(1-ngh);
          for z=1:nvar
              if max(1,z)>Ub(1,z)
                  max(1,z)=Ub(1,z);
              elseif min(1,z)<Lb(1,z)
```

```
                    min(1,z)=Lb(1,z);
                end
            end
            popother(j+other,1:nvar)=min+(max-min).*rand(1,nvar);
            popother(j+other,nvar+1)=object( popother(j+other,:));
            functionevaluation=functionevaluation+1;
        end
    end

  temp=[popelite;popother];
  temp=sortrows(temp,nvar+1);

  popmsites=Lb+(Ub-Lb).*rand(nbees-msite,nvar);
  popmsites(:,nvar+1)=object(popmsites);

  functionevaluation=functionevaluation+nbees-msite;

  pop=[temp(1:msite,:);popmsites];

  pop=sortrows(pop,nvar+1);

end
Lam = pop(1,1)
K = pop(1,2)
seg = pop(1,3)

plot(bestmatrix)

disp("optimum Answer is =")
disp (pop(1,:))
```